Gravity waves resolved in Numerical Weather Prediction products

Dissertation
zur Erlangung des Grades
Doktor der Naturwissenschaften (Dr. rer. nat.)

von
Cornelia Strube

vorgelegt der
Bergischen Universität Wuppertal
Fakultät für Mathematik und Naturwissenschaften

BERGISCHE
UNIVERSITÄT
WUPPERTAL

JÜLICH
Forschungszentrum

Jülich, January 20, 2021

The PhD thesis can be quoted as follows:

urn:nbn:de:hbz:468-urn:nbn:de:hbz:468-20220127-093209-3
[http://nbn-resolving.de/urn/resolver.pl?urn=urn%3Anbn%3Ade%3Ahbz%3A468-20220127-093209-3]

DOI: 10.25926/9aj4-nw39
[https://doi.org/10.25926/9aj4-nw39]

Abstract

Gravity waves are important drivers of global circulations in the middle atmosphere. Amongst others they exert drag on the background wind while breaking. Predictive atmospheric simulations are usually based on general circulation models. Those struggle to realistically represent small-scale dynamics like gravity waves, because long time frames and necessary computational efficiency restrict climate model setups to coarse spatial resolutions. Therefore, parametrisations are usually part of forecast model setups of the atmosphere. Parametrisations refer to simplified physical models for subgrid-scale processes including gravity waves. Model studies have shown for instance that missing gravity wave drag influences the global circulation and leads to a systematically late breakdown of the southern-hemispheric polar vortex. In contrast to climate models, weather prediction systems have recently reached operational spatial resolutions that are able to resolve a large part of the gravity wave spectrum in the middle atmosphere. Their products, hence, can be used to investigate the generation and distribution of gravity waves in critical regions like the southern polar vortex region and improve future parametrisation schemes for climate models.

This thesis introduces an analysis concept for wave characteristics and the propagation of resolved gravity waves in operational fields from the European Centre for Medium-Range Weather Prediction “Integrated Forecast System” (IFS). The analysis of gravity waves in model data as well as observations is complicated by the abundance of different dynamic processes present in the atmosphere at the same time. Characteristic patterns of inertial instabilities and other wave-like phenomena have been misinterpreted as gravity waves before. Therefore, this thesis focusses first on the ability of different approaches to separate gravity wave signals from the rest of the atmosphere. These methods are referred to as “background removal” and are usually based on the distinction of small- and large-scale phenomena by spectral filtering along different spatial dimensions. The comparison of a vertical and a horizontal filtering approach showed that inertial instability structures are easier separated from gravity waves by applying the horizontal filtering. The results further suggest that zonal wavenumbers of order 6 for the stratosphere and

18 for the troposphere are best applied for the separation.

A wave field at the lower edge of the southern polar vortex southeast of New Zealand, which was previously observed from satellite and recovered in the IFS data, is analysed in detail. The investigation concentrates on generation processes and propagation pathways of waves in this wave field and connects properties of these waves (e.g. the horizontal phase speeds and wave propagation direction) and the environment (e.g. the wind directions). The results reveal that substantial oblique propagation of the waves from mid-latitude sources takes place in the troposphere and lowermost stratosphere. Accordingly, oblique propagation is already relevant below 15 km altitude. In addition, different kinds of non-orographic generation processes have to be taken into consideration. Thus, especially oblique propagation should be part of modern parametrisation schemes in future climate model setups, unlike the current standard for gravity wave parametrisations dictates.

Zusammenfassung

Schwerewellen tragen wesentlich zum Antrieb globaler Zirkulationen in der mittleren Atmosphäre bei. Sie üben unter anderem beim Brechen eine Beschleunigung auf den Hintergrundwind aus. Vorhersagesimulationen der Atmosphäre basieren üblicherweise auf allgemeinen Zirkulationsmodellen. Diese haben Schwierigkeiten, kleinskalige, dynamische Prozesse wie Schwerewellen realistisch darzustellen, weil Klimamodellrechnungen durch die großen zeitlichen Skalen und den damit verbundenen hohen Rechenbedarf weiterhin auf grobe, räumliche Auflösungen beschränkt bleiben. Parametrisierungen sind daher üblicherweise Bestandteil von Vorhersagemodellen der Atmosphäre. Parametrisierungen bezeichnen vereinfachte physikalische Modelle für Prozesse, die auf kleineren Skalen als der Gitterauflösung auftreten, einschließlich Schwerewellen. Modellstudien haben zum Beispiel gezeigt, dass ein abgeschwächter Schwerewellenantrieb die globale Zirkulation beeinflusst und zu einem systematisch verspäteten Zusammenbrechen des südhemisphärischen Polarwirbels führt. Im Gegensatz zu Klimamodellen haben Wettervorhersagesysteme kürzlich operative, räumliche Auflösungen erreicht, die große Teile des Schwerewellenspektrums in der mittleren Atmosphäre auflösen. Ihre Produkte können deshalb für die Untersuchung der Entstehung und Ausbreitung von Schwerewellen in wichtigen Regionen wie der Südpolarwirbelregion genutzt werden und verbessern damit zukünftige Parametrisierungen für Klimamodelle.

Diese Doktorarbeit stellt ein Analysekonzept für Welleneigenschaften und die Ausbreitung von Schwerewellen vor, die in operativen Ausgabefeldern des “Integrated Forecast System” (IFS, dt. “Integrieten Vorhersagesystem”) des Europäischen Zentrums für mittelfristige Wettervorhersage aufgelöst sind. Die Analyse von Schwerewellen aus Modell- und Beobachtungsdaten wird durch die Fülle von unterschiedlichen, dynamischen Prozessen erschwert, die zur gleichen Zeit in der Atmosphäre auftreten. Typische Muster von “inertial instabilities” (dt. Trägheitsinstabilitäten) und anderer wellenartiger Phänomene wurden in der Vergangenheit fälschlicherweise als Schwerewellen interpretiert. Zuerst wird daher der Fokus in dieser Doktorarbeit auf die Eignung verschiedener Ansätze zur Trennung von Schwerewellensignalen vom Rest der Atmosphäre gelegt. Diese Methoden

werden häufig als “background removals” (dt. Hintergrundentfernung) bezeichnet, und basieren üblicherweise auf der Unterscheidung von klein- und großskaligen Phänomenen durch Spektralfilterung entlang unterschiedlicher, räumlicher Dimensionen. Der Vergleich von vertikalen und horizontalen Filteransätzen zeigt, dass “inertial instability”-Strukturen mit Horizontalfiltern einfacher von Schwerewellen getrennt werden können. Weiterhin weisen die Ergebnisse darauf hin, dass für die Stratosphäre Wellenzahlen der Ordnung 6 und für die Troposphäre der Ordnung 18 entlang des Breitenkreises für die Trennung verwendet werden sollten.

Ein Wellenfeld nahe dem Südpolarwirbel südöstlich von Neuseeland, das zuvor in Satellitenbeobachtungen gezeigt und auch in IFS-Daten wiedergefunden wurde, wird im Detail untersucht. Die Untersuchung konzentriert sich auf Entstehungsprozesse und Ausbreitungswege von Wellen in diesem Wellenfeld und verbindet dabei Eigenschaften der Wellen (z.B. horizontale Phasengeschwindigkeiten und Wellenausbreitungsrichtung) mit Eigenschaften der Umgebung (z.B. Windrichtungen). Die Ergebnisse zeigen, dass umfangreiche schräge Wellenausbreitung von Quellen von mittleren Breiten in der Troposphäre und untersten Stratosphäre stattfindet. Schräge Ausbreitung ist entsprechend bereits unterhalb von 15 km Höhe relevant. Zusätzlich müssen verschiedene, nicht-orographische Entstehungsprozesse berücksichtigt werden. Besonders die schräge Ausbreitung sollte daher Bestandteil moderner Parametrisierungsschemata in zukünftigen Klimamodellkonfigurationen sein, anders als es der aktuelle Standard für Schwerewellenparametrisierungen vorgibt.

Contents

Chapter 1

Introduction

Internal gravity waves are oscillations in a stably stratified atmosphere triggered by vertically displaced air parcels. Gravity is acting as a restoring force to bring the air parcel back to its equilibrium level in the general flow. Neglecting exchange processes, an upward displaced air parcel expands, because the atmospheric pressure decreases with altitude and the air cools adiabatically by the lift. At the same time, the air parcel becomes denser than the ambient air because the atmospheric density gradient is generally lower than the adiabatic density gradient. Then, gravity forces the air parcel downwards, which gives this oscillation its name. The air parcel is accelerated downwards by gravity as long as the density of the parcel is higher than the ambient air. Momentum carries the parcel further downwards until it is outweighed by the buoyancy decelerating and forcing the parcel, which is now lighter than the ambient air, upwards again[1]. In the atmosphere, air parcels are not isolated but interact in their harmonic oscillation with air below and above which accumulates into the vertically propagating wave motion associated with internal gravity waves. The wave motion can be observed as disturbances in atmospheric properties including density, temperature, pressure, horizontal and vertical winds. The upward-displaced, cold part of the wave can lead to condensation and gravity waves can then directly be observed in wave cloud formation (cf. Fig. 1.1).

[1] In some traditional texts from the 1970s and later (e.g. Holton, 1992), gravity waves are therefore also referred to as “buoyancy waves”, since it is the interplay of gravity and buoyancy that balances the oscillation. This alternative naming would have avoided confusion with gravitational waves which are widely discussed in astrophysical contexts, but it did not prevail.

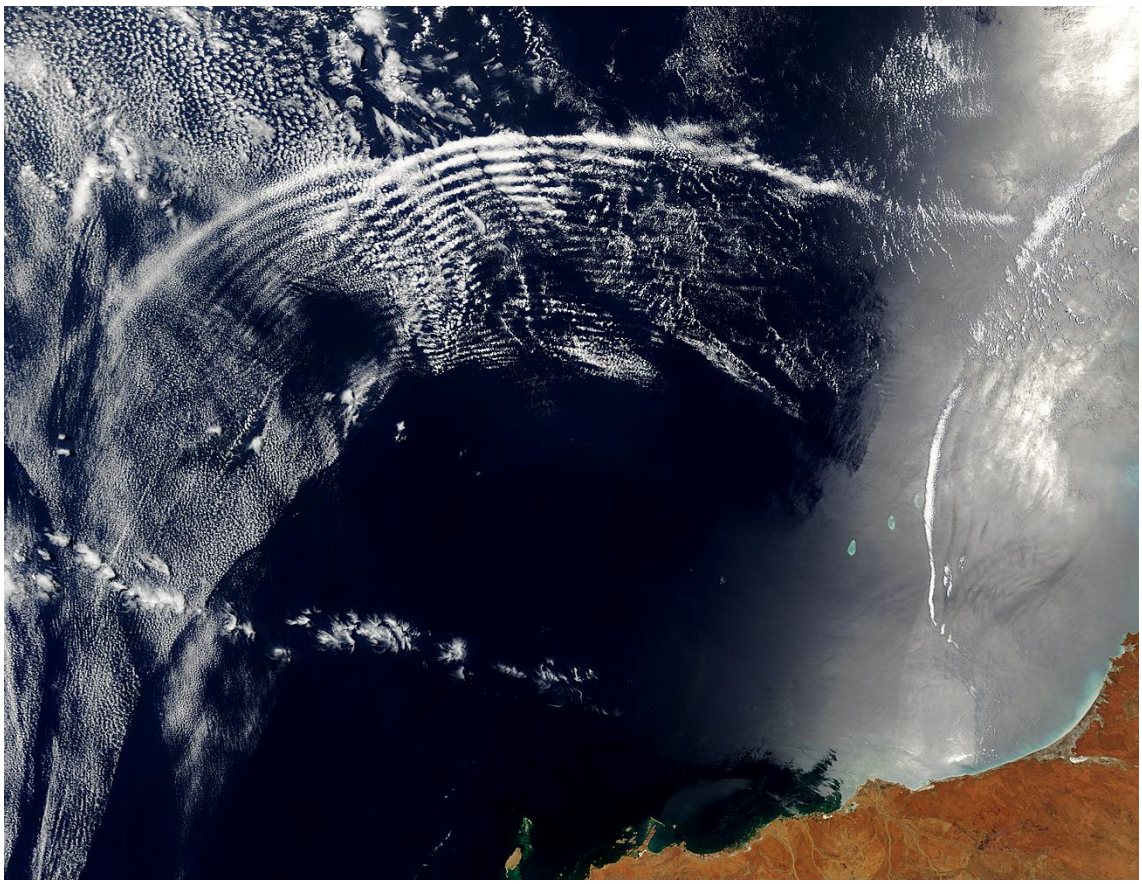

Figure 1.1: Wave clouds over the Indian Ocean close to Australia in true-color Moderate Resolution Imaging Spectroradiometer (MODIS) image, taken by the Terra satellite on November 11, 2003 (Picture taken by Jacques Descloitres, MODIS Rapid Response Team, NASA/GSFC (NASA Visible Earth)).

The initial vertical displacement for gravity wave motion is often illustrated by flow over an obstacle, like a mountain ridge. Besides topography, a number of processes acting mainly in the troposphere present the most important sources for gravity waves including convection, instabilities along frontal systems and jet streams as well as breaking waves and wave interaction (referred to as secondary generation) (Fritts and Alexander, 2003; Plougonven and Zhang, 2014; Alexander et al., 2010). Less frequently, gravity waves were also connected to volcanic eruptions (Ripepe et al., 2016; De Angelis et al., 2011) and tsunamis (Artru et al., 2005) as well as to non-tropospheric sources like auroral heating events (Richmond and Roble, 1979).

Atmospheric gravity waves propagate in all spatial directions. In this context, they

transport energy and momentum from (mostly) tropospheric sources upwards and deposit them in the middle atmosphere by breaking, dissipation and wave interactions (Holton, 1982; Fritts and Alexander, 2003; Nappo, 2012; Boeloeni et al., 2016). The deposition has significant driving impact on the large-scale circulation and the characteristics of the middle atmosphere in time and space. Gravity waves contribute to the stratospheric and mesospheric branches of the Brewer-Dobson circulation (Alexander and Rosenlof, 2003; McLandress and Shepherd, 2009; Butchart et al., 2010), the quasi-biennial oscillation (QBO) in the stratospheric winds (Dunkerton, 1997; Baldwin et al., 2001; Ern et al., 2009, 2014) and the semiannual oscillation at the stratopause (Garcia et al., 1997; Ern et al., 2015). Gravity waves accelerate or decelerate the circulation with the deposition of their momentum. This is referred to as gravity wave drag.

Internal gravity waves in the atmosphere exist on a wide spectrum of wavelengths and frequencies[2]. In the troposphere, scales of waves can be very short. For instance, mountains generate gravity waves of very small wavelength that are mostly relevant in the boundary layer (approximately 0 to 2 km altitude). Such short wavelength are predominately present between reflection layers. In the middle atmosphere, gravity wave scales of a few tens to a few thousands kilometer horizontal wavelength are most important (e.g. Preusse et al., 2009a).

According to Shepherd (2014), unresolved (i.e., subgrid-scale) processes including gravity wave drag impacts are the most uncertain aspect of climate modelling to date. Until today, general circulation models and global climate models are too coarse to resolve the whole spectrum of gravity waves. To incorporate these unresolved processes in the models, process parametrisations are employed. Parametrisations refer to drastically simplified approximations of the complex physical process are calculated frequently within the system to mimic the behaviour in a computationally cost-effective manner. The first studies of a gravity wave drag parametrisation in general circulation models goes

[2]The wavelength of an atmospheric wave refers to the distance between two crests respectively troughs of a plane wave. A three dimensional wave structure is fully represented in space by the wavelengths of vertical cuts through the atmosphere along the principle spatial directions. The wave frequency describes the number of wave cycles in time along the propagation direction. The matter will be discussed in more detail in Chap. 2.

back to Lindzen (1981) and Holton (1982). The former laid the theoretical ground work and the latter refined the process into the first implementation of such a parametrisation into a global climate model for topographically generated gravity waves. Gravity wave parametrisations are historically often separated into two independent entities that are implemented alongside each other: (1) an orographic gravity wave drag parametrisation implementing dedicated characteristics of topography-generated waves like the pure vertical propagation over the excitation area and (2) a non-orographic gravity wave drag parametrisation for everything but mountain waves. Different parametrisation approaches reviewed, for instance, by McLandress (1998), Kim et al. (2003) and Orr et al. (2010). Even though these reviews are more than 10 or even 20 years old, they still give a good representation of the implementations used in many general circulation model setups today.

In order to allow for a simple and cost-efficient implementation, unfortunately, parametrisations often lack realism in representing complex physics by design. Usually, parametrisations only allow for vertical as well as instantaneous propagation of the gravity waves up to a level where an amplitude threshold would be met by a conservatively propagating wave. Conservative propagation in this respect refers to an exponential growth in amplitude with height. These simplifications are made in order to facilitate parallelisation as many general circulation models deal with parametrised physical processes column-wise. The parametrisations are usually tuned to best reproduce climatologies of the mean temperature structure and mean winds from observations (Manzini and McFarlane, 1998). Only Orr et al. (2010) based their tuning on direct observations of global gravity wave distributions (Ern et al., 2006), which have large uncertainties of their own (Alexander et al., 2010).

General circulation models (GCMs) were widely shown to lack realism in describing the mean state of the atmosphere, if they do not take the effect of gravity waves into account (Lindzen and Holton, 1968; McLandress, 1998; Manzini and McFarlane, 1998; Kim et al., 2003; Orr et al., 2010). For example, a systematic delay in the springtime breakdown of the stratospheric polar vortex in the southern hemisphere due to insufficient

gravity wave drag was first found in the Canadian Middle Atmosphere Model (CMAM). It has since been often referred to as the "Missing Drag Problem" and is arguably the most recent example of this issue (e.g. McLandress et al., 2012). There have been attempts to solve this problem by enhancing orographic drag in the existing parametrisations (Garcia et al., 2017) or artificially adding gravity wave momentum flux as it would be induced by subgrid-sized mountains from small islands (Alexander and Grimsdell, 2013). However, global observations of mesoscale gravity waves indicate that these approaches do not explain the full discrepancy. It is not well understood which process fills the gap in gravity wave drag in reality. However, several recent studies have proposed a number of candidates:

- Downwind advection of mountain waves originating at midlatitude mountain ridges like the Andes and polar regions such as the Antarctic Peninsula combined with refraction of the waves into the polar stratospheric jet region (Sato et al., 2009)
- Sub-gridscale orography of small islands in the Southern Ocean (Alexander and Grimsdell, 2013)
- Non-orographic sources like storm tracks on the Southern Ocean (Wu and Eckermann, 2008; Hendricks et al., 2014)
- A collection of small amplitude waves generated by jet instabilities and spontaneous flow adjustments at the edge of the stratospheric polar night jet or tropospheric jet streams (Hindley et al., 2015)
- Secondary-generated gravity waves in the breaking region of a first generation of orographic waves (Hindley et al., 2015)

Already the first global observations of gravity waves in the southern hemisphere winter by Microwave Limb Sounder (MLS) (Wu and Waters, 1996b) on the Upper Atmosphere Research Satellite (UARS) and the Cryogenic Infrared Spectrometers and Telescopes for the Atmosphere (CRISTA) instrument (Preusse, 2001; Ern et al., 2004) show that the high wind velocities around the southern polar vortex are associated with an almost uniform

band of enhanced gravity wave activity. While the correlation to the wind speeds was evident early on (Preusse et al., 2003; Plougonven et al., 2017), the main sources for the enhanced activity especially far off land (i.e. not in the region of the Southern Andes or the Antarctic Peninsula) remain unclear. Based on MLS and ECMWF data, Wu and Eckermann (2008) proposed first that the gravity waves observed in the polar vortex may be generated by the storm track regions at lower latitudes and propagate obliquely into the vortex.

Oblique propagation is a fundamental property of gravity waves. Given that most gravity waves have much longer horizontal than vertical wavelengths, oblique propagation has to be expected to be the regular case[3]. Such oblique propagation can be directly observed. For instance, Sato et al. (2003) showed oblique propagation of a single wave packet in a case study based on radiosonde observations taken from a research vessel. Using propagation models with a global launch distribution, Sato et al. (2009); Preusse et al. (2009a) and Kalisch et al. (2014) investigated the importance of oblique propagation for the gravity wave distributions in the upper stratosphere and mesosphere. Such modelling results are strongly supported by the patterns revealed from sub-annual cycle variations in a long time series of gravity wave momentum flux which was inferred from temperature measurements of the Sounding of the Atmosphere using Broadband Emission Radiometry (SABER) instrument (Chen et al., 2019). All these investigations point to a continuous poleward propagation and focusing of gravity waves in the mid stratosphere and higher up.

The concept of sources in the storm track is supported by an investigation of a global model run with 7 km grid spacing of Holt et al. (2017). They show convection and frontogenesis around 50 °S and corresponding maxima of gravity wave momentum flux at 15 km altitude. However, already at approximately 18 km altitude super-pressure balloon observations show strong gravity wave momentum flux around 60 °S at the lower edge of the stratospheric polar jet (Hertzog et al., 2008; Geller et al., 2013). Also observations of

[3]This is true for gravity waves except for those mountain waves where the wind flows perpendicular to the mountain ridge and the intrinsic horizontal group velocity compensates the advection of the wave packet with the wind.

the High Resolution Dynamics Limb Sounder (HIRDLS) as low as 20 km altitude (Geller et al., 2013; Ern et al., 2018) find the maximum further south (around 60 °S) and much lower magnitudes of momentum flux at lower latitudes above the storm tracks.

Model resolution is constantly increasing. Especially analysis and reanalysis products of weather services, which integrate observation information from a wide variety of instruments with their data assimilation tools, are shown to represent a generally realistic dynamic atmosphere up to stratospheric altitudes (Jewtoukoff et al., 2015; Preusse et al., 2014; Wright and Hindley, 2018). For instance, the operational analysis products of the Integrated Forecast System (IFS) from the European Centre for Medium-Range Weather Forecasts (ECMWF) has a horizontal resolution of about 9 km globally in 2020[4]. In addition to the daily weather forecast, weather services also provide reanalysis products for research purposes, where historic data over several decades is processed with a consistent version of the fully integrated system including the assimilation of observations. The latest reanalysis from ECMWF, ERA5, provides data from 1979 ongoing with a constant resolution of 31 km horizontally. However, horizontal resolutions in the order of 10 km are not sufficient to fully abandon gravity wave drag parametrisations. Especially for middle atmosphere modelling, higher resolutions would be necessary up to more than 100 km altitude, which requires much higher computational power. This shows that even a one-time multi-decade run is limited by available computational resources in the representation of gravity waves. Climate forecasts are just as complex and span over even longer time frames and need to cover different scenarios and modelling options. Thus, a relatively coarse resolution will be necessary in climate modelling for years to come, requiring the parametrisation of small-scale dynamics.

Investigating these long-running reanalysis data sets with high and consistent resolution can help to understand propagation and characteristics of those parts of the gravity wave spectrum that are already resolved in the Numerical weather prediction products. This paves the way to improve parametrisations for climate forecasts, which cannot afford the required resolution. High resolution snapshots of the atmosphere from ECMWF-IFS

[4]The current standard is the resolution from cycle CY46R1 running on an octahedral reduced Gaussian grid with 1280 latitude lines between pole and equator (ECMWF, 2019).

analysis products allow for thorough extraction and detailed characterisation of resolved gravity wave structures. Several consecutive snapshots every few hours allow to build a realistic representation of the background atmosphere for a gravity wave propagation model and follow the characterised waves in time and space to find sources and to identify dominant pathways through the atmosphere to reach high altitudes.

The first essential step in gravity wave analysis from atmospheric data, both from observations and model products, is the extraction of gravity waves using scale separation. There have been studies to separate atmospheric data into a rotational (i.e. inertia-induced) and a divergent (i.e. gravity-wave-induced) part (Bühler et al., 2014; Lindborg, 2015), however, the separation according to spectral scales is far more common to date (e.g. Ehard et al., 2015; Tsuda et al., 2000; de la Torre et al., 2006; Fetzer and Gille, 1994; Preusse et al., 2002; Alexander et al., 2008a; Ern et al., 2018).

Two main topics are addressed in this thesis: (1) Gravity wave extraction from different temperature data sets and (2) what sources and pathways of gravity waves in the southern polar vortex region can be identified. The former solidifies the technical base for the investigation of the latter, while the latter contributes to answering one of the most pressing questions in climate modelling: How does gravity wave momentum flux get to the stratosphere at 60 °S to solve the Missing Drag Problem? In this thesis, the following research questions will be discussed to address these topics:

- **How well can gravity waves and background be separated in different data sets?**
  - How does horizontal filtering perform as a gravity wave background removal in the presence of inertial instabilities signals compared to vertical filtering?
  - What is the optimal cutoff wavenumber for Numerical weather prediction (NWP) product model temperatures in the upper troposphere and lower stratosphere (UTLS) and the stratosphere, respectively, to avoid interference with other wavelike structures?

- **From which sources and through which pathways do gravity waves enter the southern polar vortex?**
  - What source regions are important for a stratospheric wave field southeast of New Zealand?
  - Which role do different source processes play in bringing momentum and energy to the lower stratosphere at 60 °S?
  - How do waves reach the region around 60 °S already in the lower stratosphere? What are likely propagation pathways?

In this context, a comprehensive approach to analyse gravity waves resolved in the customary outputs of operational Numerical Weather Prediction systems is used to evaluate the spectrum of waves that is included within the model outputs. This incorporates: (1) extracting the wave information as perturbations from the atmospheric field variables, (2) characterising the wave structure on the spatial shape of the perturbations and (3) studying the evolution of particular characterised waves in time using process modelling with a gravity wave ray-tracer and statistical considerations to identify preferred motion.

In preparation to discuss these questions, Chapter 2 collects general knowledge about gravity wave physics and how it can be interpreted for atmospheric modelling. Special attention will be given to properties characterising gravity waves, like phase speeds, group velocity, their interaction with the general flow and energy and momentum transport induced by gravity waves in relation to the background wind. In addition, the propagation of mountain waves and the theoretical background of ray tracing are introduced briefly. Chapter 3 summarises the properties of the different atmospheric data sets used in this thesis. Chapter 4 introduces the methodology of how gravity waves that are resolved in snapshots of global model atmospheres can be extracted, characterised and followed in their wave evolution. This includes an overview of the few-wave, small-volume sinusoidal fitting method S3D and the established gravity wave ray-tracer GROGRAT. In Chap. 5, the challenges of gravity wave extraction from temperature data sets are addressed. First, the spectral filtering methods for scale separation used in this study, namely vertical and

horizontal filtering, are introduced and subsequently compared in order to evaluate their performance of these approaches as gravity wave background removals. Special attention is paid to their performance in presence of inertial instability signals in an artificial inertial instability perturbation data set, in ERA5 temperatures and temperature observations from the SABER instrument (Strube et al., 2020). Chapter 6 investigates the propagation pathways and likely source regions for a particular stratospheric wave field in the austral summer of 2014 close to New Zealand. Therefore, the structure is first fully characterised at 25 km altitude using the S3D method. Then, the identified wave packets are traced back to their origin using the GROGRAT ray-tracer and categorised according to the path the rays take through the atmosphere and locations where the corresponding wave originated. The chapter is concluded with a discussion of implications for the way gravity waves take to 60 °S that can be drawn from the distributions and properties of the modelled waves (Strube et al., 2021).

Chapter 2

Gravity wave theory

Atmospheric gravity waves are small-scale oscillations in the stably stratified atmosphere that transport energy and momentum from the troposphere to the middle atmosphere. At higher altitudes, energy and momentum are deposited through dissipation or breaking. These waves are characterised by dispersion and the ability to propagate both horizontally and vertically. Gravity waves have a direct impact for synoptic-scale weather and its forecasting (Koch and Siedlarz, 1999) and are important drivers of the global circulation in the middle atmosphere.

This chapter contains an overview of general properties and the physical interpretation of atmospheric gravity waves as groundwork for the following studies. A more detailed discussion of gravity wave theory can be found, for instance, in the text book of Holton (1992) or in the detailed review paper of Fritts and Alexander (2003).

2.1 Perturbation effects of gravity waves (Linear theory)

In general, atmospheric motion is described by the fundamental fluid equations of an incompressible flow based on momentum, mass and energy conservation. The derivation of these basic nonlinear equations is standard knowledge and can be found for instance in Andrews et al. (1987).

Perturbation theory comprises the theoretical backbone for a qualitative (i.e. physical) analysis of waves in the atmosphere. It describes a method to simplify atmospheric

wave motion in a way that the complex nonlinear system of fundamental equations can be solved applying linearisation and standard methods like the wave ansatz. It is assumed that all field variables of the atmosphere can be separated into a background atmosphere or basic state and local perturbations from this background, which are deviations of the field that are small and rapid compared to the variations in the background state. The background properties, in particular background winds and buoyancy frequency, change only slowly over a wave cycle and period and, hence, can be treated as constant coefficients in the system. This assumption is often referred to as Wentzel-Kramers-Brillouin (WKB) approximation.

$$(u, v, w, \theta, p, \rho) = (\bar{u}, \bar{v}, 0, \bar{\theta}, \bar{p}, \bar{\rho}) + (u', v', w', \theta', p', \rho'), \tag{2.1}$$

where, e.g., u represents the total zonal wind, $\bar{u}$ the large scale motion and u' the perturbation part. The remaining variables are meridional wind v, vertical wind w, potential temperature θ, pressure p and density ρ. By neglecting all terms involving products of the perturbations, a system of linear differential equations of the perturbations is generated that can be solved by employing a harmonic wave solution of the form

$$\left(u', v', w', \frac{\theta'}{\bar{\theta}}, \frac{p'}{\bar{\rho}}, \frac{\rho'}{\bar{\rho}}\right) = \mathfrak{Re}\left(\left(\tilde{u}, \tilde{v}, \tilde{w}, \tilde{\theta}, \tilde{p}, \tilde{\rho}\right) \cdot \exp\left(i\left(kx + ly + mz - \omega_g bt\right) + \frac{z}{2H}\right)\right). \tag{2.2}$$

In Eq. 2.2, $\boldsymbol{k} := (k, l, m)$ signifies the 3D wave vector and $\omega_g b$ the wave frequency, as seen by a static observer. The density scale height is described by H and $\mathfrak{Re}$ refers to the real part of the complex exponential function[1]. All variables with with a tilde ˜ describe the corresponding amplitude of the wave solution for the variables, e.g. $\tilde{u}$ is the zonal wind amplitude, etc.

The solution of the system of linear differential equation relates the wave vector $\boldsymbol{k}$ and

[1] Only the real part of the solution has physical significance and will be treated in the derivation.

the intrinsic wave frequency $\hat{\omega}$ to each other.

$$\hat{\omega}^2 = \frac{N^2\left(k^2+l^2\right)+f^2\left(m^2+\frac{1}{4H^2}\right)}{k^2+l^2+m^2+\frac{1}{4H^2}}. \tag{2.3}$$

This is the frequency relative to the background wind under consideration of the background state properties, which is usually referred to as dispersion relation. The intrinsic wave frequency $\hat{\omega}$ relates to the ground-based frequency ω_{gb} through a Doppler shift about the background wind, i.e., $\hat{\omega} = \omega_{gb} - k\bar{u} - l\bar{v}$.

A detailed derivation from the linearised system to this dispersion relation is given in Fritts and Alexander (2003).

Physically relevant solutions are only achieved if the wave vector $\boldsymbol{k}$ is real. A wave solution is only valid for vertical propagation, if the intrinsic frequency is confined to the range between Coriolis frequency and the buoyancy frequency, i.e. $f < \hat{\omega} < N$.

For $\hat{\omega} > N$, the exponent in the wave ansatz becomes real and one finds an exponential decrease of amplitude without phase variation. This is either an evanescent wave from start or causes wave reflection. In the other limit, when for a propagating wave $\hat{\omega} \to f$, $m \to \infty$, the vertical wavelength becomes infinitesimal and, before that point is reached, the wave becomes unstable and breaks.

In order to give insight in a situation, often the mid-frequency approximation is sufficient, that is assuming that the intrinsic frequency is far from the two limits of allowed frequencies ($N \gg \hat{\omega} \gg f$)

$$\hat{\omega} = N\left|\frac{k_h}{m}\right|. \tag{2.4}$$

2.1.1 Phase speed and group velocity

A characteristic property for propagating gravity waves is the phase speed defined as the speed of the phase front, i.e., the speed an observer would have to move to see the wave phase as constant. In general, the phase speed depends only on properties of the wave,

in particular the wavenumber vector $\boldsymbol{k}$ and intrinsic wave frequency $\hat{\omega}$ with

$$\hat{c}_h := \frac{\hat{\omega}}{\sqrt{k^2 + l^2}}, \quad \hat{c}_z := \frac{\hat{\omega}}{m}. \tag{2.5}$$

Analogously, phase speeds can be defined for zonal and meridional wavenumber. However, it is important to keep in mind that phase speed is not a vector, and c_h is not equal to $\sqrt{c_x^2 + c_y^2}$.

In practice, it can be helpful to define horizontal phase speeds along the wave vector as

$$(\hat{c}_x, \hat{c}_y) = \frac{\hat{\omega}}{k_h} \frac{(k, l)}{k_h}. \tag{2.6}$$

When $\hat{c} \to 0$, the vertical wavenumber goes to infinity and, thus, the vertical wavelength goes to 0. This presents a critical level where the wave breaks and cannot propagate further upward. A critical level might therefore not only be reached if the wind velocity changes, but also if the wind direction turns.

The form of the dispersion relation in Eq. 2.3 is valid for all gravity waves with phase speeds considerably slower than the speed of sound (Gossard and Hooke, 1975; Jones and Bedard, 2018). It shows that gravity waves have, other than Rossby waves or Kelvin waves, no limitation in the direction of propagation.

The intrinsic group velocity is the velocity of a wave packet moving through the atmosphere and, hence, the speed and direction the energy is transported by the wave. It is determined by the derivative of the intrinsic frequency over the wavenumber

$$(\hat{c}_{gx}, \hat{c}_{gy}, \hat{c}_{gz}) = \left(\frac{\partial \hat{\omega}}{\partial k}, \frac{\partial \hat{\omega}}{\partial l}, \frac{\partial \hat{\omega}}{\partial m} \right) \tag{2.7}$$

$$= \frac{1}{\hat{\omega}\kappa} \left(k \left(N^2 - \hat{\omega}^2 \right), l \left(N^2 - \hat{\omega}^2 \right), -m \left(\hat{\omega}^2 - f^2 \right) \right) \tag{2.8}$$

with $\kappa = \left(k^2 + l^2 + m^2 + \frac{1}{4H^2} \right)$. Analogously to the concept of intrinsic and ground-based frequencies, the group velocity as well can be interpreted in relation to the ground instead of the the background wind using the ground-based frequencies for the derivatives. This results in an additive shift by the background wind vector $(\bar{u}, \bar{v}, 0)$.

Therefore, the group velocity vector is always oriented parallel to constant-phase lines (also referred to as phase fronts). Wavenumbers of $k > 0$, $l = 0$ and $m < 0$, for instance, correspond to eastward and downward motion of the wave phases but eastward and upward propagation of the energy.

Under the mid-frequency approximation ($f \ll \hat{\omega} \ll N$), the phase speed and the group velocity are of the same magnitude but opposite in the vertical direction:

$$(\hat{c}_{gh}, \hat{c}_{gz}) \approx \left(\frac{\hat{\omega}}{k_h}, -\frac{\hat{\omega}}{m} \right). \tag{2.9}$$

In the general case, where the horizontal wavelengths are significantly longer than the vertical wavelengths (i.e., $k \ll m$), intrinsic propagation goes further in the horizontal than in the vertical. Mountain waves present a special case which will be discussed in 2.3 in more detail.

2.1.2 Polarisation relations

The polarisation relations describe the relations between the different variables in which a gravity wave can be observed.

$$\tilde{\zeta} = \frac{g}{TN^2}\tilde{T} \tag{2.10}$$

$$\tilde{w} = \hat{\omega}\frac{g}{TN^2}\tilde{T} \tag{2.11}$$

$$\tilde{u}_h = \frac{\lambda_h}{\lambda_z}\tilde{w} \tag{2.12}$$

where $\tilde{u}_h$ is the horizontal wind amplitude in direction of the wave vector. Equation 2.12 implies that the wind is parallel to the phase fronts of the wave.

To determine this simplified form of the equations, the scale height term $\frac{1}{4H^2}$ in the dispersion relation 2.3 is neglected. This choice is realistic for all $\hat{\omega}$, also those close to N or f given a fitting wavenumber range. Under mid-frequency condition (cf. Eq.2.4), this leaves a simple relation for $\tilde{u}$ and $\tilde{T}$:

$$\tilde{u}_h = \frac{\lambda_h}{\lambda_z}\tilde{w} \approx \frac{g}{TN}\tilde{T} \approx 2\,\tilde{T}. \tag{2.13}$$

High frequency gravity waves have large vertical wind amplitudes in relation to temperature amplitudes. Using typical stratospheric values for the buoyancy and background temperature, the factor $\frac{g}{TN}$ in Eq. 2.13 is close to 2 m s^{-1} K^{-1}.

Figure 2.1 illustrates the characteristics of a upward-propagating (e.g. $m < 0$ and $\hat{\omega} > 0$) gravity waves in the northern hemisphere ($f > 0$) in particular showing the phase relationship between wind speeds, geopotential and temperature.

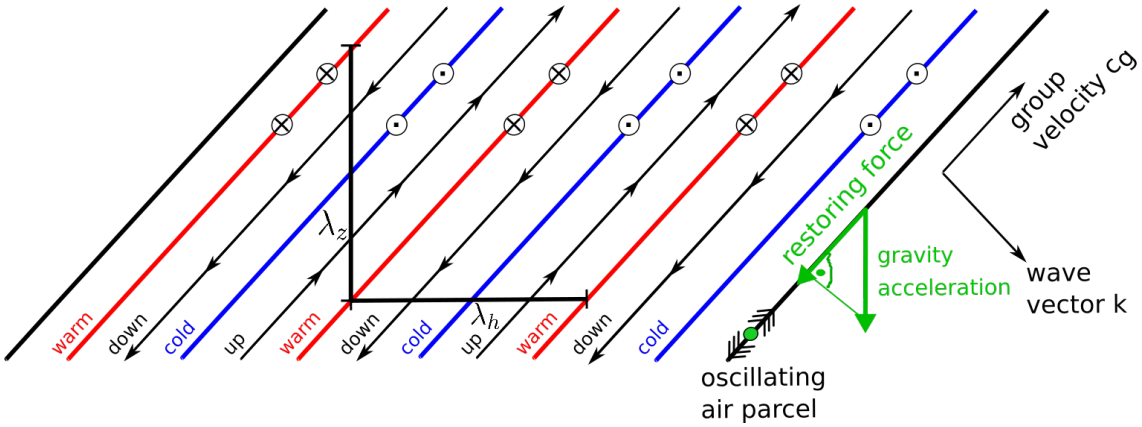

Figure 2.1: Schematic view of a gravity wave along its horizontal propagation direction. The wave is drawn to propagate intrinsically to the left, with downward phase and upward group velocity. This way, a warm front is followed by upward wind, by a cold front, by downward wind and by a warm front again, forming a full cycle. Winds are forced parallel to the phase fronts by pressure gradients. Assuming a moving oscillator, accelerations are consistent with the dispersion relation. Coriolis force superposes an additional rotation with (for the northern hemisphere) winds into the surface of the picture on the warm front and out off the surface on the cold front. After Andrews et al. (1987).

2.1.3 Interaction with the background flow and momentum flux

The conserved quantity in gravity wave motion without dissipation is the vertical flux of horizontal momentum, often referred to as pseudomomentum flux, which can be characterised by

$$(F_{px}, F_{py}) = \bar{\rho}\left(1 - \frac{f^2}{\hat{\omega}^2}\right)\left(\overline{u'w'}, \overline{v'w'}\right). \tag{2.14}$$

In the rest of this thesis, the term gravity wave momentum flux (GWMF) always refers

to this pseudomomentum flux for simplicity of notation.

In the fundamental fluid equations, the effects of perturbations on the general flow are implemented in the acceleration terms by X and Y with the relation (Fritts and Alexander, 2003):

$$\frac{du}{dt} - fv + \frac{1}{\rho}\frac{\partial p}{\partial x} = X \tag{2.15}$$

$$\frac{dv}{dt} + fu + \frac{1}{\rho}\frac{\partial p}{\partial y} = Y \tag{2.16}$$

and defined by

$$(X, Y) = -\frac{1}{\rho}\frac{\partial}{\partial z}\left(F_{px}, F_{py}\right). \tag{2.17}$$

Using the polarisation relations momentum flux can also be calculated from the wave vector and the temperature amplitude (Ern et al., 2004):

$$(F_{px}, F_{py}) = \frac{\bar{\rho}}{2}\frac{(k,l)}{m}\left(\frac{g}{N}\right)^2\left(\frac{\tilde{T}}{\bar{T}}\right)^2 \quad \text{if } \frac{\tilde{\theta}}{\bar{\theta}} = \frac{\tilde{T}}{\bar{T}}. \tag{2.18}$$

The relation between Eq. 2.18 and Eq. 2.14 can easily be derived using the mid-frequency polarisation relations with the exception of the correction factor $\left(1 - \frac{f^2}{\hat{\omega}^2}\right)$. However, Equation 2.18 is not limited to the mid frequency approximation. In fact, it is also valid for low intrinsic frequencies $\hat{\omega}$ close to f.

Gravity waves interact with the background atmosphere by dissipation and breaking. The vertical gradient of the absolute value of GWMF is negative in the case of dissipation by definition. The GWMF is proportional to and directed along the horizontal wave vector (cf. Eg. 2.18). The acceleration (X, Y) is again in the direction of the pseudomomentum (cf. Eq. 2.17), thus the effect that the pseudomomentum puts on the basic flow is directed along the intrinsic propagation direction. This together with a critical level criterion of the horizontal phase speed (cf. equation 2.6) makes up the interaction of gravity waves with the background flow as sketched in Figure 2.2. A critical level is reached where the

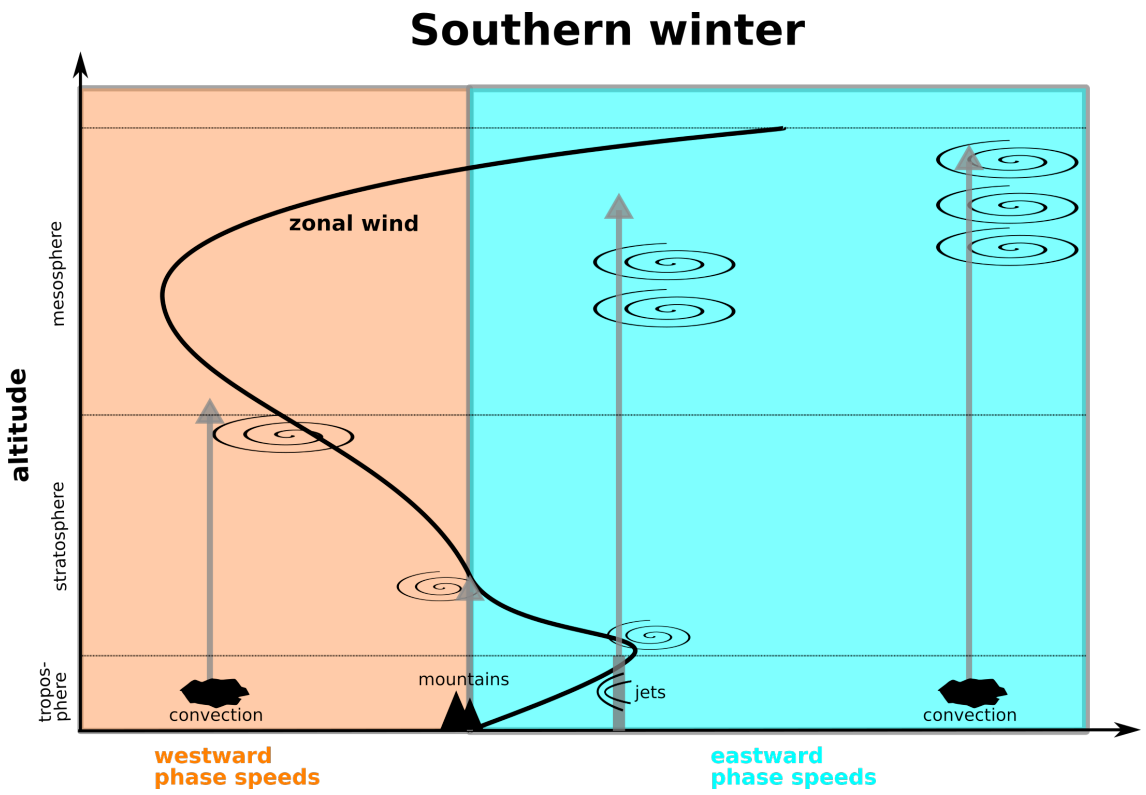

Figure 2.2: Schematic view of the interaction of gravity waves from different sources with the background flow for typical mid-latitude winter conditions in the southern hemisphere. The x-axis gives the wind velocity for the typical wind profile (black line) or the ground-based phase speed of the gravity waves (arrows). The spirals indicate wave breaking and dissipation. Waves break at critical levels or because amplitudes grow because of the decrease in density with altitude where the waves reach their stability limit. According to Fig. 1 in Kim et al. (2003). (Northern-hemisphere winter conditions usually exhibit slower wind speeds and slightly different distributions of breaking and dissipation. However the general idea of wind filtering is equivalent. See Kim et al. (e.g. 2003).)

wind matches the ground-based phase speed and waves break. Waves may also break below when amplitude growth due to decreasing density reaches the stability limit. In the southern hemisphere winter, the wind velocities are somewhat higher, which however does not impact the general principles depicted for northern hemisphere winter.

2.2 Sources

Gravity waves are generated by disturbances in a stably stratified flow where an air parcel is displaced in altitude and subsequently undergoes buoyancy oscillation to return to a

balanced state. The trigger generating the primary disturbance can be manifold but most commonly considered are flow over an obstacle (orographic generation), convection or instabilities in the vicinity of jets and frontal systems. Other less recognised processes comprise orography-related weather phenomena, wave-wave or wave-mean flow interactions. As an overview, the characteristics of gravity waves generated by the most common concepts are briefly reviewed in the following.

2.2.1 Orographic waves

The very first studies of gravity waves in the atmosphere considered flow over a mountain ridge (Wegener, 1906; Trey, 1919). Since that time, orographically generated gravity waves, often referred to as “mountain waves”, have been studied widely with theoretical approaches, model studies and observations (e.g. Queney, 1948; Nastrom and Fritts, 1992; Bacmeister, 1993; Preusse et al., 1999). Mountain waves exhibit small horizontal scales of approximately 2 to 200 km at excitation, phase speeds near zero and vertical wavelengths closely related to both the local static stability and the mean winds (Eckermann and Preusse, 1999; Fritts and Alexander, 2003). General circulation models usually include a dedicated orographic gravity wave parametrisation scheme applying instantaneous gravity wave drag in the middle atmosphere right above the generating mountain.

2.2.2 Jets and fronts

A comprehensive review of different mechanisms generating gravity waves at jets and fronts was presented by Plougonven and Zhang (2014). According to them, gravity waves close to jets and fronts can in general be explained by spontaneous adjustment emission (or short: spontaneous emission). Spontaneous emission refers to the general idea that imbalanced motions adjust back to a balanced regime and generate gravity waves in the process.

One theory covered by the spontaneous emission concept goes back to Lighthill (1952); it explains how acoustic waves are generated by turbulent motions and is the backbone of gravity waves generation at vortices such as cyclones. These gravity waves

have spatial scales larger than the vortex. Unbalanced instabilities (Plougonven and Snyder, 2005) and sheared disturbances (Vanneste and Yavneh, 2004) collect processes that connect gravity waves and balanced motions in sheared flows on inertial scales. Wind shear instabilities, like envelope generation at Kelvin-Helmholtz billows, typically generate gravity waves of small spatial scales (few kilometres) and ground-based phase speeds directly linked to the mean wind at the shear layer (Bühler, 1999).

A jet exit region, i.e., the area where the flow is slowing down upstream of a ridge or trough in a meandering jet stream, presents a common location for spontaneously generated gravity waves. Uccellini and Koch (1987) introduced a robust description of the properties of the jet and general wind conditions to facilitate gravity wave emission here. The gravity waves generated in jet exit regions usually exhibit large amplitudes and subsynoptic horizontal wavelengths of a few 100 km.

2.2.3 Convection

In contrast to an orographic source, convective sources can generate a wide range of phase speeds, vertical wavelengths and frequencies. They also generate horizontal wavelengths of very different scales. Especially low-frequency convective gravity waves are often observed at a long horizontal distance from theirs source, which makes co-location of waves and sources difficult (Preusse et al., 2001; Fritts and Alexander, 2003; Kalisch et al., 2016; Trinh et al., 2016). Existing observations of convective gravity waves show a close link between high-frequency waves and deep convection though the highly intermittent nature of convection as a source complicates observation (Sato et al., 1995; Dewan et al., 1998; McLandress et al., 2000; Alexander et al., 2000; Fritts and Alexander, 2003).

Three general mechanisms associated with convection are commonly proposed in the literature to generate gravity waves — (1) pure thermal forcing, (2) the “transient mountain” effect, and the (3) mechanical oscillator effect. Each mechanism generates waves of particular characteristics, however, they are not assumed to occur distinctly but coupled. Purely thermally generated gravity waves refer to a mechanism where the intermittent

latent heat release within a convective cell provides the main gravity wave forcing. These waves propagate vertically and exhibit vertical wavelengths of roughly twice the heating depth (Salby and Garcia, 1987; Garcia and Salby, 1987; Alexander et al., 1995; Piani et al., 2000) in mostly isotropic wave fields. "Transient mountain" waves represent an analogon to orographic waves where the convective heating in the bottom of the stably stratified layer above the convection acts as a barrier to the mean background flow similar to the mountain ridge for orographic generation (Clark et al., 1986; Pfister et al., 1993). Transient mountain waves have typically much larger amplitudes than waves generated by thermal forcing, generate anisotropic wave fields, and propagate opposite to the mean wind relative to the transient mountain obstacle (Fritts and Alexander, 2003). Alternating updrafts and downdrafts in a convective cell trigger oscillation and vertically displace the isentropes at the base of the stably stratified layer above the convection. This generates vertically propagating gravity waves similar to the response of a mechanical oscillator in a stratified fluid (Clark et al., 1986). The mechanical oscillator mechanism locally generates waves with intrinsic frequencies equal to the oscillator's frequency which is roughly half the tropospheric buoyancy frequency. Thus, this mechanism typically generates waves with very high frequency in the upper troposphere. Waves released by organised convection like a storm front (Fovell et al., 1992) are inheritely anisotropic. For a single convection cell, the generated waves are isotropic at the source, but become anisotropic when modulated by the background wind (Lane et al., 2001). In general, gravity wave generation from convective sources is still not very well understood compared to other sources like orography.

2.3 Propagation of gravity waves

For process studies on mountain waves, the situation of an infinitely long ridge encountered by a wind perpendicular to this ridge has been considered traditionally. In this case, waves generated by flow over the ridge have a ground-based phase speed c close to zero, such that they propagate vertically right above the mountain source. Accordingly, the phase speed in the direction of the wind compensates the background wind. If a

purely westerly wind u is assumed to flow over a ridge with north-south orientation, the meridional wave component is zero, and the phase speed is defined by

$$\hat{c} = \hat{c}_x = \frac{\hat{\omega}}{k} = -u. \tag{2.19}$$

From Eq. 2.9 follows directly that the intrinsic group velocity c_g is equal in magnitude to the wind and pointing in opposite direction to it. The outcome is a mountain wave that propagates purely in the vertical. This theoretical explanation was already the base for pioneering studies on mountain waves by Queney (1948).

If, however, the ridge is at an angle to the wind, i.e., the meridional wavenumber l is not zero, the situation becomes more complex. Then, the orientation of the ridge determines the direction of the wave vector.

Using the definition from Eq. 2.8 and assuming mid-frequency conditions[2], the scalar product of the ground-based group velocity and the horizontal wave vector calculates

$$\begin{aligned}
(c_{gx}, c_{gy}, c_{gz}) \cdot (k, l, m) &= \frac{k(N^2 - \hat{\omega}^2)}{\hat{\omega}\kappa}\, k + \frac{l(N^2 - \hat{\omega}^2)}{\hat{\omega}\kappa}\, l + \frac{-m(\hat{\omega}^2 - f^2)}{\hat{\omega}\kappa}\, m \\
&= \frac{(k^2 + l^2)(N^2 - \hat{\omega}^2) - m^2(\hat{\omega}^2 - f^2)}{\hat{\omega}\kappa} \\
&\overset{\text{mid-freq.}}{=} \frac{(k^2 + l^2)N^2 - m^2\hat{\omega}^2}{\hat{\omega}\kappa} = \frac{m^2\hat{\omega}^2 - m^2\hat{\omega}^2}{\hat{\omega}\kappa} \\
&= 0
\end{aligned} \tag{2.20}$$

with $\kappa = (k^2 + l^2 + m^2 + \frac{1}{4H^2})$.

A wave with $l \neq 0$ propagates horizontally along the phase fronts. The ratio $\frac{l}{k}$ describes the angle at which the wave propagates and indicates a larger meridional component as it increases. Likewise, the horizontal phase speed, saturation amplitudes and saturation GWMF decrease with a stronger meridional propagation. Therefore, the most efficient lateral propagation of GWMF is accomplished with similar magnitudes in both horizontal wave components, i.e., $|k| \simeq |l|$, in a westerly wind.

[2]Mid-frequency conditions refer to $N \gg \hat{\omega} \gg f$. The dispersion then simplifies to $\hat{\omega}^2 = \frac{N^2(k^2+l^2)}{m^2}$.

2.4 Propagation, refraction and amplitude calculation using ray tracing

Ray tracing is a common approach to follow the propagation of a fully characterised, monochromatic wave throw a complex atmospheric flow (Plougonven and Zhang, 2014). The method goes back to Lighthill (1978) and was discussed in great detail in numerous publications after 1995.(Marks and Eckermann, 1995; Eckermann and Marks, 1996; Guest et al., 2000; Hasha et al., 2008)

Gravity wave ray tracing builds on the use of the dispersion relation to define the ray tracing equations as

$$\frac{d\boldsymbol{x}}{dt} = \frac{\partial\hat{\omega}}{\partial\boldsymbol{k}} \tag{2.21}$$

$$\frac{d\boldsymbol{k}}{dt} = -\frac{\partial\hat{\omega}}{\partial\boldsymbol{x}}. \tag{2.22}$$

Wave action conservation is calculated as

$$\frac{\partial A}{\partial t} + \nabla \cdot (c_g A) = -\frac{2A}{\nu}. \tag{2.23}$$

Here $A = \frac{E}{\hat{\omega}}$, with $\hat{\omega}$ the intrinsic wave frequency, and E the wave energy density (Marks and Eckermann, 1995), ν the "damping timescale" determined from parametrised radiative and dissipative damping (Zhu, 1993), c_g the group velocity vector of the wave packet.

Chapter 3

Data

As described in the Introduction, NWP models recently reached grid resolutions that cover a large part of the atmospheric wave spectrum including gravity waves. The full spectrum of gravity waves, however, is still not resolved and neither are other processes relevant for gravity wave excitation and dissipation.[1]. These models are often referred to as “process-allowing” instead of “process-resolving” models. Two prominent examples of gravity-wave allowing global model products are the operational analysis and the reanalysis product ERA5, both based on the ECMWF-IFS, which are used in this study and explained in detail in this chapter.

Besides the model analysis products, this thesis evaluates satellite data from the infrared limb sounder SABER to investigate the performance of background removal techniques.

All data sets used for these investigations are briefly described in this chapter.

[1] One process that is not fully resolved in this context is convection. However, special runs of NWP models with convection-allowing grid resolutions are used in more research cases also with regard to gravity waves recently (Stephan et al., 2019a,b).

3.1 Global, gravity-wave allowing ECMWF products: ECMWF-IFS operational analyses

The European Centre for Medium-Range Weather Forecasts (ECMWF) Integrated Forecast System (IFS) provides global high-resolution atmospheric data. For the operational analysis product, the ECMWF-IFS couples a general circulation model (GCM) with a 4D-variational data assimilation system. The assimilation of a wide range of in situ, ground-based and satellite data ensures a good representation of the current state of the atmosphere. Gravity waves are considered as "atmospheric noise" and are not assimilated, but generated self-consistently by the model. The spatial resolution of the ECMWF GCM is being continuously increased. For instance, in 2014 data had a horizontal resolution of N640/T1279, corresponding to $\approx$16 km (on the reduced Gaussian grid)[2]. Due to hyper-diffusion, the shortest horizontal wavelengths properly resolved are about 8 to 10 times this horizontal resolution, i.e. $\approx$150 km (Skamarock, 2004; Preusse et al., 2014), but in case of strong mountain wave forcing also shorter wavelengths may be contained. In the vertical, altitudes up to approximately 80 km are represented by 137 vertical levels. The vertical resolution decreases stepwise with around 250 m at the tropopause, and about 2 km at the stratopause.

An overview of a number of studies comparing gravity waves resolved in ECMWF analyses products with ground-based and satellite observations is given by (Preusse et al., 2014). They showed that ECMWF gravity wave temperature amplitudes are usually underestimated by a factor of 1.5–2. Inside this limit, gravity waves compare favourable up to $\approx$40 km altitude both in global distribution as well as in wavelengths. Also the phases agree often between modelled fields and observations. Observed and modelled gravity waves agree particularly well for orographic waves and waves in the jets, which most likely are generated by spontaneous imbalance, but suboptimally for gravity waves from convection (Schroeder et al., 2009). Above 40 km altitude, amplitudes are rapidly decreasing in ECMWF data due to the sponge layer of the model (Ehard et al., 2018).

To apply the wave characterisation with the S3D method described in Sect. 4.1, the

[2]This is the resolution of ECMWF-IFS model cycle Cy38r2, which was operational in 2014.

data are interpolated to a constant longitude-latitude grid of $0.2^\circ \times 0.2^\circ$ and to geometric altitudes with a sampling of 500 m. This corresponds to the model vertical resolution in the middle atmosphere (approximately at 25 km altitude). The resolution is also adequate for the atmospheric background needed for performing ray tracing studies with the GROGRAT ray tracer.

3.2 Global, gravity-wave allowing ECMWF products: ERA5 temperatures

ERA5 is the newest reanalysis product based on the 4D-Var data assimilation of ECMWF's Integrated Forecast System (IFS). In the simulation, the grid consists of 137 hybrid model levels with a top at 0.01 hPa. In the stratosphere, the hybrid levels are less than 1 km apart. The IFS is a spectral system. The reanalysis has a horizontal resolution of $\approx 0.28^\circ$ or $\approx$31 km. Power spectral analysis showed that only gravity waves with wavelengths larger than a few grid points ($6\Delta x$; in this case $\approx 1.7^\circ$) may be expected to be well resolved in the reanalysis output (Jewtoukoff et al., 2015). Recently, ERA5 has been shown to represent the stratospheric temperature structure with more details than other reanalysis products (Wright and Hindley, 2018).

3.3 Infrared limb-sounder observations: SABER temperatures

The Sounding of the Atmosphere using Broadband Emission Radiometry (SABER) instrument is operated onboard the Thermosphere Ionosphere Mesosphere Energetics and Dynamics (TIMED) satellite, which was launched in December 2001 and is still operational in 2020. The limb-sounding instrument records profiles of atmospheric radiation by scanning its viewing direction vertically and covers a large altitude range from the tropopause to well above 100 km. Altitudes above approximately 60 km are not considered in this thesis since the focus of the investigations lies in the stratosphere and upper troposphere. The tangent point track, i.e., the track of observation points, is approxi-

mately 2 000 km away from the orbital track. Temperatures are predominantly retrieved from emissions of the 15 µm CO_2 infrared band. Retrieval results are provided in vertical profiles with approximately 2 km vertical resolution, 400 m vertical sampling and spaced on average 400 km along the tangent-point track. Detailed information on the retrieval are summarized in Remsberg et al. (2008).

The TIMED satellite covers most of the globe with about 15 orbits per day. Thus, waves up to a zonal wavenumber of 6 to 7 can be resolved along a latitude circle (Salby, 1982). The satellite performs yaw maneuvers close to every 60 days. This alternates the SABER viewing geometry between 50 °S to 82 °N, northward viewing, and 82 °S to 50 °N, southward viewing. While latitudes equatorward of 50 ° are covered continuously, the higher latitudes of each hemisphere are only covered 60 d in every 120 d.

According to Remsberg et al. (2008), the precision, i.e. the random instrument error, for the SABER temperature measurements in the V1.07 retrieval results to 0.3 K to 0.6 K (mean at 0.45 K) in the stratosphere (between 20 km and 50 km altitude). The precision error is predominantly related to pointing jitter. The temperature data used in the course of this thesis were obtained with the V2.0 retrieval algorithm. Ern et al. (2018) and the official SABER website (`http://saber.gats-inc.com/temp_errors.php`) report that there are no changes in the retrieval between V1.07 and V2.0 that would impact the precision of the temperature estimates, but the overall accuracy could be altered.

Chapter 4

An analysis setup for resolved gravity waves in ECMWF products

This chapter introduces the general approach of how gravity wave signals resolved in atmospheric model fields are extracted, characterised and subsequently used to feed a gravity wave propagation model. Eventually, this allows for statistical analysis of propagation pathways of gravity waves from a point in the middle atmosphere backward in time to find their origin.

From observations and modeling, some variables are directly available, such as temperature and trace species concentration. To analyse the influence of gravity waves on the general circulation, quantities such as gravity wave momentum flux have to be derived from those observed or modeled variables based on concepts of gravity wave theory. The general problem with inferred parameters is that the atmosphere has a rather complicated structure in both wind and temperatures even without gravity waves. Especially in the upper troposphere and lower stratosphere (UTLS), strong gradients in all these quantities occur due to dynamical and radiative processes. The atmospheric state measured by any instrument as well as implemented in any model can be interpreted as the superposition of the *background* state of the atmosphere, i.e. the state that the atmosphere would have without any gravity wave activity and the changes (*perturbations*) caused by gravity waves. This necessitates, as a first step in the processing, to separate the atmospheric

field in the background, i.e. the global-scale structures, and the gravity wave structures within. Spectral filtering is a traditional approach to isolating the higher frequency gravity wave information from variables like temperature and winds. A more detailed introduction of two methods for spectral filtering is part of Chap. 5.

In a second step, the resulting perturbation fields can be analysed to characterise the waves as described in the following. Section 4.1 introduces the requirements and algorithm implemented for the S3D method, a few-wave, small-volume sinusoidal fitting approach for gravity waves, in detail. This also comprises a number of inferred parameters to characterise the properties of the fitted waves in a more intuitive manner and a brief discussion of the implementation tool developed at Forschungszentrum Jülich. Section 4.2 presents the gravity wave propagation program GROGRAT that was introduced by Marks and Eckermann (1995) and Eckermann (1996) and its application on the fitted wave results from Sect. 4.1.

4.1 Gravity wave characterisation: S3D method

Gravity wave perturbation fields as obtained from background removals are used to infer gravity wave characterisations and can be based on any atmospheric data containing gravity wave information.

In order to infer gravity wave momentum flux from temperature fields, the wave amplitude and the three-dimensional wave vector, i.e. wavenumbers (respectively wavelengths) in three spatial dimensions, has to be determined. In order to study the propagation of waves, intrinsic and ground-based phase speeds are inferred from the wave vector and serve as input to a more sophisticated propagation model like GROGRAT, where the a wave packet and its associated wave action is tracked to implement wave saturation, dissipation and breaking.

Choosing the best suited method to analyse gravity waves in atmospheric data sets has posed challenges to scientists since the first attempts (e.g. Gossard and Hooke, 1975; Press et al., 1992). This is not solely depend on the type of data, but also on the available information due to the nature of these data sets.

As stated in the section introduction, the atmosphere is a complex system with many different processes composing the shape and structure observed in all atmospheric variables, like temperatures and winds. Most of those shapes are based on harmonics and can be represented by a superposition of spectral components.

Heisenberg's uncertainty principle puts a limit to the combination of spatial localisation and spectral resolution of spectral analysis methods. Depending on the scientific question, one or the other has to be the focus in choosing the suitable approach. Accordingly, a multitude of different analysis methods based on spectral analysis has been developed over the years, each employing a different compromises between spatial localisation and spectral resolution.

The most common method of Fourier transform does inherently not allow for any spatial dependency, but provides a complete orthonormal description in spectral space. As a side effect Fourier transform spreads a signal to a large number of spectral components, if a spatial pattern is, against the assumption, localised as for instance a mountain wave above a mountain ridge. Still, Fourier transform was used in historical analyses of airplane data (Nastrom et al., 1987) taking tremendous care that the favourable observation conditions do not change in between flight segments.

In the presence of such strongly localised gravity wave sources, global data are evidently non-homogeneous when considering mesoscale gravity waves. Two methods are still retaining good spectral resolution, but localise features in physical space as well: Windowed Fourier Transform and Wavelet analysis. In particular wavelet analysis is often used for gravity wave analysis in profile-wise observed measurement data such as radiosondes (Zink and Vincent, 2001a,b), lidar data (Rauthe et al., 2008), satellite IR radiances (Eidmann et al., 2001) or in situ airplane observations (Bacmeister et al., 1996; Bramberger et al., 2017; Portele et al., 2018). Windowed Fourier transform may still be a method of choice for very high resolution data (Schumann, 2019). Both methods require window-lengths several times the extent of the largest target wavelengths for good performance.

Further on the way to higher spatial localisation and less spectral information are the

S3D method described in this chapter and the 3-D Stockwell transform developed by (Wright et al., 2017). They focus on a few wave components determined in a small fitting volume with extent of a typical wavelength or less. On the other end of the method spectrum, the Hilbert transformation provides the envelope of the contained wave amplitudes for each point in a data set (Schoon and Zuelicke, 2018). Since also phase information is provided, wavelengths may be deduced from the spatial gradient of this phase, but strictly under the assumption of the presence of only one single wave. In fact, the UWADI tool of Schoon and Zuelicke (2018) based on the Hilbert transformation requires smoothing in order to produce reasonable amplitude and wavelength estimates.

For the purpose of this study, S3D is the optimal compromise between spatial localisation and spectral resolution, as will be explained in the following section.

4.1.1 Requirements to the method

The S3D method is a small-volume, few-wave decomposition method sequentially fitting monochromatic waves to atmospheric perturbation data. The method and two computational implementations have been developed by members of the remote sensing group at IEK-7[1] over recent years as new tool for the analysis of gravity waves in three dimensional data sets. It was first introduced by Lehmann et al. (2012) and applied in several studies for characterising gravity waves in simulated and true satellite observations (Preusse et al., 2014; Ern et al., 2017). The implementation is described in more detail in Sect. 4.1.4.

In the application, a monochromatic wave model $f(\boldsymbol{x}, \boldsymbol{k}; A, B)$ is fit to the temperature perturbation data $T'(\boldsymbol{x})$ in a small-volume fitting cube. The vector $\boldsymbol{x}$ consists of the spatial coordinates of the data which shall be fitted, $\boldsymbol{k}$ is the wave vector and A and B are amplitudes to be determined by the fit.

Gravity wave fields are genuinely spatially highly variable. The local background wind direction and wind speed constantly induces refraction of the vertical wavelengths during the propagation through the atmosphere. This requires a localised method. The

[1] Institute of Energy and Climate Research: Stratosphere at Forschungszentrum Jülich

S3D method represents complex wave structures by superposing several monochromatic waves and restricting wave parameters to a local characterisation. Quantitative analysis of energy budgets usually work well with locally characterised gravity wave activity to approximate the more complex real structure. The S3D method was originally developed for the analysis of gravity wave information in the proposed satellite limb imager PREMIER (ESA, 2008), where the swath width of the instrument was rather small and hence posed a limitation to the wave spectrum that would be possible to apply in fully spectral approaches.[2] Conventional spectral approaches suffer from the limitation that only wave components with wavelength spatially smaller than the analysed area can be used in the representation, whereas spectral components outside would be lost and even cause aliasing and thus undesired artifacts in the processed data.

The S3D characterisation then takes place in small analysis volumes inferring individual wave properties locally employing superpositions of one or more monochromatic wave components. While this allows to identify more than one wave influencing the general flow at one location.

The ECMWF model fields provide a fully global snapshot every 6 hours with a high spatial resolution of the order of 10 km horizontally. Therefore, the limitation of a small analysis area imposed by the observations is not actually given in analysing ECMWF model products. This would allow, in principle, for global or part-global spectral analysis with fine spectral resolution. However, gravity wave sources are highly localised and intermittent. For mountain waves, for instance, wave packets can often be described with two wavelengths or less. This calls for a localised method attributing most of the observed perturbations to a few monochromatic wave components. Localised wave fits also benefit from the fact that they provide wave vectors matching the true localised wave field (as opposed to windowed spectral analysis methods where the window size defines the available spectral components).

[2] Spectral approach here refers to the any approach that would representing the complex wave structure with a full spectrum (hence a large amount of wave components) like a Fourier analysis on the analysis area instead of specifying a small amount of wave components with specific characteristics to represent the wave structure.

4.1.2 Description of the algorithm

Cover the analysis area with small volumes

A target region is covered with relatively small, possibly overlapping analysis volumes for a systematic analysis. The analysis volumes are chosen as blocks of points in the input grid, i.e. in the case of ECMWF analysis products the volume is defined by a number of grid points in each spatial direction on a longitude-latitude-altitude grid, which makes the volume quasi-rectangular for small volumes[3] The analysis volume will sometimes be referred to as fitting cube or analysis cube in this thesis.

The size of the analysis volume is determined by the expected wavelengths in the data which typically requires some numerical test runs to make the right compromise. Usually the size of the analysis volume should be of the same order or down to two times smaller than the expected predominant wavelengths locally present in the perturbation data. Both using a cube size far smaller as well as far larger than the fitted wavelengths may result in unwanted deviations from true amplitudes and wavelengths. Larger cube sizes often result in underestimation of the wave amplitude, since the wave has to be expected constant for a larger spatial volume and possibly several wave periods. If the cube size is too small the phase variation inside the fitting volume may be too small in order to determine the correct wave vector, in particular in the presence of a secondary wave, noise or an incomplete background removal; typically all three effects impact the analysis of the data. The choice of the fitting volume size will be discussed in more detail in 6, section 6.1.2 on the example of a specific case study.

Sinusoidal wave model

The wave model used for the sinusoidal fit is a monochromatic wave and defined by

$$f(\boldsymbol{x}, \boldsymbol{k}; A, B) = A\sin(kx + ly + mz) + B\cos(kx + ly + mz), \tag{4.1}$$

where $\boldsymbol{x} = (x, y, z)$ is the location in the local Cartesian coordinate system.

[3]The curvature of the longitude-latitude grid is affecting the shape of the cube. In the mid-latitudes in a regular longitude-latitude grid, the edge length in kilometre of an analysis volume in zonal direction at 30 °S and at 50 ° would differ by a factor of $\frac{\cos(30\,^\circ)}{\cos(60\,^\circ)} \approx 1.73$. This is taken into account in the fitting program.

The wave vector $\boldsymbol{k} = (k, l, m)$ is defined by the wavenumbers k, l, and m along the three directions of x, y, and z. In the case of GCM data x, y, and z define the local geophysical coordinates. The wave model is completed with two amplitude variables A and B that are fitted to the data.

Equation 4.1 is equivalent to a single sinusoid defined by an amplitude and a phase instead of two amplitudes of orthogonal sinusoids:

$$f(\boldsymbol{x}, \boldsymbol{k}; \hat{T}, \phi) = \hat{T} \sin(kx + ly + mz + \phi). \tag{4.2}$$

It is easily shown that the models are equal for $\hat{T} = \sqrt{A^2 + B^2}$ and $\phi = \arctan\left(\frac{A}{B}\right)$. This latter model (Eq. 4.2) might be more intuitive for physical interpretation of the fitting results while the first (Eq. 4.1) is better suited for the implementation as the least-square minimisation trivially linearises in the two amplitudes. Amplitude, phase and wave vector fully characterise the monochromatic model wave except for a remaining ambiguity of 180° in the wave vector direction, discriminating between upwards and downwards propagating waves with also inverted horizontal propagation direction, i.e. the fit cannot discriminate between a wave (k, l, m) and a wave $(-k, -l, -m)$. For this thesis, upward propagation is assumed as the default by postulating a negative vertical wavenumber m (cf. chapter 2).

The sinusoidal fits are not limited to characterizing temperature perturbations. Lehmann et al. (2012) and Preusse et al. (2014) used the approach to analyze structures in horizontal winds and vertical winds as well.

Determination of the wave vector

The fit of the wave parameters is carried out by minimizing the cost function,

$$\chi^2 = \sum_i \left(y_i - \sum_j f(\boldsymbol{x_i}, \boldsymbol{k}_j) \right)^2, \tag{4.3}$$

where y represents the observations or atmospheric model data at each location $\boldsymbol{x}$. The index i runs through all locations $\boldsymbol{x}_i$ with a data point y, while the index j sums up the

few wave components. The fit is applied to snapshots of ECMWF analysis temperature perturbations for a case study in chapter 6 in this thesis. Determining the wave vector is a non-linear problem and requires a variational approach, which will be described below. The amplitudes A, B can be derived by analytically solving the minimization of χ^2 for a given wavevector $\boldsymbol{k}$.

The wave vector is determined by applying standard methods for a least-squares fit in wavenumber space. Currently, fitting with nested grid intervals and a steepest descent approach are implemented. Both of these approaches are iterative in finding a suitable solution. The first is computationally more complex but more robust against getting stuck in a local optimum, while the second is much faster, but sometimes delivers unreliable results. But both methods profit immensely from a good initial value by speeding up the interval search or even ensure that a reasonable solution is found at all, respectively. In the S3D method, a FFT is calculated over the analysis volume and the component with the largest spectral amplitude is used as an initial guess for the wave vector. The amplitude and phase are calculated analytically.

In general, the nested grid intervals method is very computationally expensive but usually more precise compared to the steepest descent fit. Therefore, in some applications, it is reasonable to apply the two methods in combination. Then, the steepest descent method is applied first to fit the data and, only if the fitting χ^2 result is not matching a chosen "goodness-of-fit" threshold[4], a second fit is subsequently carried out using nested grid intervals. The second fit is only chosen as the final result, if the χ^2 is indeed smaller than the first.

Fitting more than one wave component

A second wave component is fitted to the data after removing the wave represented by the fit results of the first component from the input perturbations for each analysis volume. This process can be repeated consecutively to analyse an arbitrary number of wave components for each analysis cube. The superposition of the single inferred

[4]The goodness-of-fit here is usually determined by evaluating whether the calculated χ^2 is smaller than the variance in the data scaled by a defined factor between 0 and 1.

wave models then represents the wave structure in more and more detail, the more wave components are considered. The value of χ^2 in comparison to the total variance in the input data $var(\boldsymbol{y}) = \sum_i y_i^2$ gives an estimate of confidence in the fit of a particular wave component. It was shown by Lehmann et al. (2012) that the superposition of two waves usually leads to a reasonable spectral representation with respect to the Fourier transform on a wider area. Also, for the analysis of data from the Atmospheric Infrared Sounder (AIRS), two wave components appear most suitable as Ern et al. (2017) have shown. A recent case study for Scandinavia indicates that three wave components would be likely required for the superposition of one large-scale with a potentially-reflected smaller scale wave which is the likely reason for an observed checkerboard pattern (Krisch et al., 2020). For ray-tracing studies the focus often lies on the first wave component only, which usually also carries most of the momentum flux.

4.1.3 Inferred wave parameters

The wave characterisation allows to infer characteristic parameters of the fitted wave, such as horizontal and vertical wavelengths, $\lambda_h = \frac{2\pi}{k_h}$ and $\lambda_z = \frac{2\pi}{m}$, wave direction, $\phi = \arctan(|\frac{l}{k}|)$. Gravity wave momentum flux is calculated from the 3D wave vector and the temperature amplitude as well as background quantities according to Eq. 2.18. The momentum flux is a key quantity to determine the potential the wave has to alter the general flow after breaking or dissipation. Illustrating the wave period, defined as $\tau = \frac{2\pi}{\omega}$ is a more accessible concept than the wave frequency to characterize wave motions, i.e. the movement of wave fronts.

4.1.4 Implementation of the method for various data sets

The S3D tool is a joint effort of several contributors and was partly refined as part of this thesis.

Originally implemented in IDL[5], most of the S3D source code was migrated to Python since 2016. A first Python version was then applied to observations of the Gimballed

[5]The Interactive Data Language (IDL) is a programming language for data analysis and visualisation owned by Harris Geospatial Solutions.

Limb Observer for Radiance Imaging of the Atmosphere (GLORIA) jointly developed by Forschungszentrum Jülich and IMK-ASF[6] at Karlsruhe Institute of Technology (KIT) (Riese et al., 2014; Friedl-Vallon et al., 2014). GLORIA can observe three-dimensional temperature fields, which were investigated with S3D in two case studied for various gravity wave source processes and gravity wave propagation (Krisch et al., 2017, 2020). The Python version for global model fields was further developed in the frame of this thesis and applied to a number of high-resolution global models to infer and compare the spectral and spatial characteristics of the gravity waves resolved (Stephan et al., 2019a,b). Furthermore, the Python tool is used for flight planning on campaigns by providing a gravity wave forecast product base on operational ECMWF-IFS data.

Python is an open-source, community-developed universal programming language developed to support a short, easily readable programming style. The open-source license of Python simplifies sharing of own code with collaborators and fits to the idea of common community licensed programs in science. The Python community is also offering a multitude of open code packages for numerical data analysis and data visualisation that are constantly advanced by the community. Furthermore, the language allows for easy integration of highly-efficient FORTRAN or C code for efficiency within a high-level programming setup.

Currently, the S3D tool is equipped to deal with three grid types:

1. A satellite grid spanning along-track, across-track and altitude coordinates specified by the measurement locations

2. A longitude-latitude-altitude grid for snapshots of global model data

3. A regular Cartesian kilometer grid for GLORIA measurements and local models

So far, the routines for the satellite grid (1.) are only implemented in IDL. The rest of the code was fully migrated to Python and thorough tests were made to check consistency to the original code for longitude-latitude grid codes (2.). Furthermore, all essential processing routines have unit tests in the python implementation.

[6] Institute of Meteorology and Climate Research - Atmospheric Trace Gases and Remote Sensing

Tasks in the consistency testing and general test case setup for the S3D code where part of the preparations to this thesis. The implementation of unit treatment within the code using the PINT package (Pint, 2020) made up a large part of this process. This allows to automatically process data supplied in arbitrary (sensible) units and prevents logic errors due to misinterpretation of data within the code.

Applications of the tools are manifold. The analysis can be coupled to a ray-tracer to provide the opportunity of interpreting global data sets and investigating the origin and propagation paths of resolved waves. Applied to global data sets from numerical weather prediction (NWP) services, these tools provide insight in the global distributions of gravity waves.

4.2 Gravity wave propagation model: GROGRAT raytracer

The software package GROGRAT (Gravity wave Regional Or Global RAy Tracer) introduced by Marks and Eckermann (1995) and further expanded to time-varying background flows by the works of Eckermann (1996) is an established tool for studies on gravity wave propagation (e.g. Eckermann, 1997; Eckermann and Preusse, 1999; Preusse et al., 2002; Gerrard et al., 2004; Preusse et al., 2009a,b; Kalisch et al., 2014; Pramitha et al., 2015; Trinh et al., 2016; Krisch et al., 2017).

In addition to the ray tracing equations, an equation for the energy balance, defining the conservation of the wave action density $A = \frac{E}{\hat{\omega}}$, with E representing the total wave energy and $\hat{\omega}$ the ground-based frequency, completes the model assuring the evolution of the amplitude within the wave packet to be represented. The software applies a saturation scheme according to (Fritts and Rastogi, 1985) and also parametrizations for turbulent and radiative wave damping (Zhu, 1993) as the waves propagate upwards.

The ray-tracing equations are derived from the gravity wave dispersion relation (Eq. 2.3) and in this way based on linear wave theory and the WKB assumption. In order to test

the validity of this assumption during ray-integration WKB calulates the WKB-criterion:

$$\delta = \frac{1}{m^2} \| \frac{\partial m}{\partial z} \| \ll 1 \tag{4.4}$$

This study uses a version of GROGRAT originating from the status reported by Eckermann and Marks (1996) with an additional correction for spherical geometry in the refraction terms of the horizontal wavenumbers as suggested by Hasha et al. (2008) and implemented by Kalisch et al. (2014). The propagation allows for a slowly changing background represented by interpolation through snapshots of the background atmosphere adding a ray tracing equation for the evolution of the wave frequency (cf. Eckermann and Marks, 1996). GROGRAT applies time variation in the background atmosphere by adding a raytracing equation for the ground-based wave frequency ω (Eckermann and Marks, 1996)

$$\frac{d\omega}{dt} = k\frac{\partial \bar{u}}{\partial t} + l\frac{\partial \bar{v}}{\partial t} + \frac{\left[N^2, k^2 + l^2 - \frac{1}{4H^2}, \hat{\omega}^2 - f^2\right]}{2\hat{\omega}\kappa}. \tag{4.5}$$

Many previous studies use generic background atmospheres like standard atmospheres or temperature and wind profiles from climatologies for raytracing studies. The ECMWF operational analyses data provides a full atmosphere for the exact situation of a study, providing a realistic, high-resolution background atmosphere. In this sense not only measurements, but also high resolution model products can be investigated in order to understand the mechanisms which lead to the excitation of the waves in the model (Preusse et al., 2014). In particular, for this thesis, rays are launched from wave parameters inferred from waves resolved in the ECMWF-IFS operational analysis temperatures. Thus, there is full consistency between the waves observed in the model and the background through which the waves are propagated.

Chapter 5

Removing complex backgrounds from gravity wave temperature perturbations using spectral filtering methods

Most analysis methods for gravity wave activity rely on an initial background removal using scale separation to extract only those signals introduced by gravity waves. The efficiency of different background removals depends highly on the method used and what perturbations next to gravity waves are present in the data.

Historically, different measurement methods with their specific characteristics have inspired the use of particular background removals (Alexander et al., 2010). For instance, radio occultation measurements using data from the Global Positioning System (GPS-RO) produce temperature profiles that are quasi-randomly scattered over the globe. Therefore, the application of a local horizontal filter would requires a tedious matching of coinciding profiles for a location from the data. The use of vertical high-pass filters is more straight-forward for the genuinely profile-based data and, hence, was applied predominantly in previous analyses (e.g. Tsuda et al., 2000; de la Torre et al., 2006).

For data with very high horizontal sampling, such as observations from microwave sub-limb and infrared nadir sounders, local horizontal filters were usually employed (Wu and Waters, 1996a; Wu and Eckermann, 2008; Hoffmann and Alexander, 2010). Infrared limb sounders collect data both in profiles with high vertical resolution and cover the whole earth in a regular fashion. Therefore, global horizontal low-pass filters are easy to apply to these data sets and have been commonly used (Fetzer and Gille, 1994; Preusse et al., 2002; Alexander et al., 2008a; Ern et al., 2018).

The different background removal techniques influence the spectrum of waves visible in the residual data and for some techniques they are even governing the spectral limits. Hence, the background removal is an important part of the observational filter.

This chapter discusses the different abilities of horizontal and vertical spectral filtering as background removals in presence of large-scale structures next to gravity waves. The investigation focusses onto temperature fields of the ECMWF reanalysis ERA5 and a satellite data set from SABER observations and aims to identify suitable characteristics cutoff lengths to savely separate gravity waves from the remaining background atmosphere (Strube et al., 2020).

5.1 Spectral filtering methods

Spectral filters, in general, are used to select wave-like information from atmospheric data, like measurements or model outputs. The filtering can be achieved by transforming the data into the wavenumber respectively frequency space applying a Fourier transform (for practical reasons usually a Fast Fourier Transform; FFT) or similar technique and subsequently retaining only the spectral power of the desired part of the spectrum.

A few limitations of the method have to be taken into consideration to apply the FFT to an atmospheric field or profile:

1. Spectral artifacts due to aliasing and leakage
2. The data extent limits the max. wavelength/period
3. The FFT expects periodic input data.

4. The FFT relies on equidistant, gapless sampling.

Gloabl model data pose the least problem in this respect, as they are regularly sampled up to the Nyquist frequency of all contained waves and periodic in longitude direction. Much more difficulties pose “sparsely sampled” data such as observations from satellite instruments. In particular, for altitude profiles of atmospheric data some preprocessing before spectral analysis is mandatory in order to remove the discontinuity at the endpoints of the profile arising from the general structure of the atmosphere.

The simplest case of an spectral filter then works as follows:

1. Detrend the data in order to minimise discontinuity at the endpoint of non-periodic data if necessary.

2. Calculate the Discrete Fourier Transform (DFT) for the spatial and/or temporal data.

3. Apply a window function to the spectral power to define what part of the spectrum is to be removed (window weight = 0), which is to be retained (window weight = 1) and which is to be damped (window weight between 0 and 1). In the simplest case, this window is a rectangular window function defined by a weight of 0 to the the spectral amplitudes of the wavenumbers or frequencies that are to be removed and 1 for everything inside the targeted part of wavenumber or frequency spectrum.

4. Reverse the transformation, i.e. apply an inverse DFT, to obtain the filtered data.

Depending on the spectral filter chosen, this procedure can be applied to retain either long wavelengths (low pass), short wavelengths (high pass) or a defined range (band pass). Fourier filters are non-local, i.e. they assume the same spectral composition for the whole analyzed data set. This limits, in principle their application to finite, non-periodic data. This can be partly overcome by applying a windowed FFT, i.e. by shifting the analysis range over the whole data set and convolving the analysis range first with a window function (Ehard et al., 2015). An alternative to a spatial window is to use in step 3 a non-trivial window function applied to weigh the spectrum.

This section describes the various methods for background removal and their application to different data sets.

5.1.1 Vertical wavelength filters

Vertical filtering has the advantage that it can be applied profile-wise without assuming any correlation between adjacent profiles. It is therefore particularly suited for GPS-RO and ground-based lidar measurements (Rapp et al., 2018a), but can also be employed easily on model products like ERA5 or the artificial inertial instability signals, which is built in Sect. 5.2.

The Butterworth filter was used as a high-pass, vertical wavelengths, FFT filter in previous studies e.g. by Ehard et al. (2015) to remove the background from lidar measurements and by Rapp et al. (2018a) for handling GPS-RO measurements. The filter is defined by a window function

$$H(\lambda_z) = \left(1 + \left(\frac{\lambda_z}{\lambda_c}\right)^{2n}\right)^{-\frac{1}{2}}, \tag{5.1}$$

with the cutoff wavelength λ_c and the vertical wavelength defined as $\lambda_z = \frac{2\pi}{m}$ for m representing the vertical wavenumber. The order of the Butterworth window is represented by n. Scales longer than the critical vertical wavelength λ_c were smoothly removed by convolving the Butterworth window.

In the studies of Ehard et al. (2015) and Rapp et al. (2018a), $n = 5$ and $\lambda_c = 15$ km were usually used as the characteristics for the filter. In the following, these typical values were adopted in most situations. Only in Sect. 5.3.3, the sensitivity of the background removal on different λ_c values is assessed, hence λ_c is altered then.

5.1.2 Horizontal wavelength filters

Horizontal or in particular zonal spectral filtering is an intuitive solution for a background removal in regularly sampled, global data sets such as general circulation model outputs of free-running models as well as assimilation products like reanalyses. The temperature and wind fields along the latitude circle are naturally periodic and with a regular (ideally high-resolution) sampling, an FFT analysis is directly applicable. In principle, zonal filtering can be adapted to satellite data as well, but then it needs to be taken into account

that a global coverage is reached only after a full day and that only 16 orbit traces are available.

Horizontal filtering for global, regularly sampled data sets

For horizontal filtering in regularly sampled, global snapshots, the FFT is applied in longitude direction to provide a zonal wavenumber spectrum for each altitude and latitude. The background is defined by low-pass filtering the spectrum with a rectangular window up to a cut-off wavenumber, k_c, i.e. the spectral amplitudes corresponding to wavenumbers larger than k_c are set to zero.

In the following, a cutoff zonal wavenumber k_c of 6 is used in the stratosphere. This cutoff has been used in a large number of previous studies on low earth orbiter (LEO); (e.g. Fetzer and Gille, 1994; Ern et al., 2018) and references therein.

Additionally, Savitzky-Golay polynomial smoothing on the spectral amplitudes with a third order polynomial on 25 points in the meridional and with a fourth order polynomial on 11 points in the vertical direction is applied. This step removes any contributions of signals with long zonal, but short meridional or vertical wavelengths from the background. Inverse FFT for every altitude and latitude location then yields a filtered 3-D background field containing only the large-scale signals. The temperature perturbations associated with gravity waves are then defined by subtracting this background point-wise from the original temperature field. Of course, perturbations of other atmospheric variables like winds or pressure can be calculated analogously.

Special case: Time-Horizontal filtering for limb-sounder data

SABER provides a global coverage over the course of one day. Applying a similar background removal as for a global model data set hence is a reasonable approach. However, data at a given latitude from the ascending or descending orbits are collected at the same local time (asynoptic sampling), respectively, rather than at one universal time (synoptic sampling). The orbit of the TIMED satellite is only slowly precessing and, hence, considering periods of planetary waves as short as a few days can lead to phase progression of

the wave. The period of one day, which SABER requires to collect the data for one global coverage, is close to the shortest period of planetary waves such as the quasi two-day waves in the mesosphere (e.g. Ern et al., 2013) or fast modes in the southern polar vortex. Accordingly, the phase shifts in this observation period and the observed structures are not longer cyclical in longitude direction. In addition, there are gaps between the measurement tracks. Satellite data hence require a more complex background removal including the temporal development.

The observation geometry of an LEO satellite limits the range of zonal wavenumbers and frequencies in which space-time spectra can be uniquely obtained (Salby, 1982). These limits allow to capture the periods of all Rossby wave modes (Salby, 1984) and equatorial wave modes (Kim et al., 2019). Furthermore, space-time spectra within the geometry limits have been proven to be mathematically correct for all permitted wavenumbers and frequencies (Salby, 1984). The use of time-longitude spectra also prevents influences of day-to-day variations in the atmospheric background due to short-period travelling planetary waves (Ern et al., 2016, 2018). Inertial instabilities were not in the focus of previous studies. Due to their characteristic scales (long horizontal, short vertical and long temporal with respect to the gravity wave spectrum), they should be easier separable from gravity waves considering the zonal and time dimension than the vertical dimension.

Ern et al. (2011, 2013) have developed such a dedicated background removal for limb-sounding satellite temperatures taking both the zonal and temporal dimension in consideration for the spectral analysis. With the relatively low resolution of the satellite temperatures in longitude and time, gravity wave signatures appear as a uniform white-noise background level in longitude-time spectra. This white-noise spectrum has to be retained after the background removal. Global-scale waves, on the other hand, exceed this white noise level and should be removed. Ern et al. (2011) used a factor of 5 above the average squared spectral amplitude of the white-noise spectral floor to define a threshold for separating between gravity wave signal and global-scale waves. The method uses overlapping 31-day time windows shifted by 15 days in each step. Spectra include zonal

wavenumbers 0 to 6 and frequencies up to 0.7 cycles per day. In order to compute the spectra, the SABER profiles are interpolated in the vertical and interpolated along the observation tracks yielding a fixed altitude-latitude grid.

The background estimation from Ern et al. (2011) is especially tailored to the sampling pattern of limb emission sounders on LEO satellites and was applied to SABER and HIRDLS (High Resolution Dynamics Limb Sounder) in the GRACILE climatology (Ern et al., 2018).

In order to determine the residual temperature fluctuations, the background is reconstructed for the precise location and time of each observation. First, spectra are interpolated in altitude and latitude. The background for the observation longitude and time is then evaluated as the superposition of the single, global-scale waves with significant spectral amplitudes using their spectral amplitudes and phases. In addition, the mean background temperature defined as the 31-day average plus a linear trend is taken into account. Eventually, the method defines the temperature perturbation at a particular location and altitude by subtracting the average local background temperature (averaged from the mostly two background temperature estimates) from the overlapping time windows. In addition, in a second step the most relevant tidal modes in stratosphere and mesosphere are explicitly removed (Ern et al., 2013). Lastly, an additional broad correction is applied that helps to calculate follow-up parameters such as gravity wave momentum flux: a dominant vertical oscillation with vertical wavelength $\lambda_z \geq 40$ km is removed to correct for remnants of quasi-stationary planetary waves and to limit the gravity wave spectrum to vertical wavelength short enough to be covered by the momentum flux estimation procedure.

In the following, this method is applied as a horizontal background removal to SABER profiles.

5.1.3 Diagnostic quantities

Linear gravity wave theory bases on the assumption that the total state of any atmospheric variables, e.g. temperature T, can be defined as a sum of a background state, $\overline{T}$,

and gravity wave perturbations, T' (cf. Eq. 2.1) like

$$T(\boldsymbol{x},t) = \overline{T}(\boldsymbol{x},t) + T'(\boldsymbol{x},t). \tag{5.2}$$

The background state is the superposition of a mean temperature profile and the large-scale influences like planetary wave and synoptic inertial instability conditions at each instance in space $\boldsymbol{x} = (x, y, z)$ and time t.

The variance $\mathrm{var}(T')$ of the zonal mean residual temperature perturbation T', also referred to as gravity wave variance, has been used as a diagnostic quantity for gravity wave activity in measured and modeled atmospheres early on (e.g. Fetzer and Gille, 1994)).

$$\mathrm{var}(T') := \frac{1}{N-1} \sum_i \left(T'_i - \langle T' \rangle\right)^2 \tag{5.3}$$

In Eq. 5.3, triangular brackets $\langle . \rangle$ represent a zonal mean at a specific snapshot or time range and N stands for the number of averaged values. This quantity shows "true" gravity wave structures in the data, if the background removal can be considered a good estimate for the large-scale fluctuations.

In addition, the zonal mean temperature perturbation $\langle T' \rangle$ is defined as a diagnostic quantity here. The index i runs through all locations along one latitude circle.

$$\langle T' \rangle := \frac{1}{N} \sum_i T'_i. \tag{5.4}$$

Two spectral methods to separate temperature perturbations from a background were introduced in detail in the Sects. 5.1.1 and 5.1.2 that will be applied hereinafter - vertical and horizontal spectral filtering. Temperature perturbations T' inferred by these background removals have been used in a number of previous studies to calculate more complex diagnostics like gravity wave potential energy densities and gravity wave momentum fluxes for climatologies of gravity wave activity.

In the case of horizontal filtering, in particular zonal wavenumber filtering, $\langle T' \rangle$ is expected to contribute only negligibly to the gravity wave variance, since the zonal average of the temperature state was already subtracted in the definition of the gravity wave tem-

perature perturbations. After vertical filtering, $\langle T' \rangle$ is not necessarily small, since the perturbations were estimated in a way that is independent of the zonal structure of the background state. In this situation, $\langle T' \rangle \gg 0$ gives a good measure for background state remnants in the derived perturbations, as shown by Rapp et al. (2018b).

In the ideal case, however, $\langle T' \rangle$ is zero or at least very small in comparison to the gravity wave perturbation that are analysed. Then, the zonal mean squared temperature perturbation $\langle T'^2 \rangle$ can be used as a good estimate for the gravity wave variance, since

$$\langle T'^2 \rangle := \frac{1}{N} \sum_i \left(T'_i\right)^2 \simeq var(T')|_{\langle T' \rangle = 0} \tag{5.5}$$

The advantage of analysing $\langle T'^2 \rangle$ rather than $var(T')$ is that it is consistent with local averages as used in global maps or spectra which cannot rely on a zonal mean average.

5.2 Data for comparison

For this study, three different kinds of data sets are used to test the background removal. Satellite measurements give unique information by providing global sampling on real observations, here represented by the SABER data introduced in section 3.3. The reanalysis data set ERA-5, described in section 3.2, has the advantage of covering a large range of spatial and spectral scales without being restricted to a specific, irregular sampling. Both data sets contain gravity waves as well as global-scale wave structures, like inertial instabilities.

In order to have a clear diagnosis whether inertial instability signals can be fully captured by a background estimate, a third data set of artificial inertial instability perturbations is introduced: An artificial perturbation model gives the opportunity to see how the background removal techniques are influencing an isolated inertial-instability-like signal. Any residual fluctuations after applying the background removal then indicate remnant inertial instability signals that should not be attributed to other processes. In realistic model data sets or measurement results possibly remnants signals might belong to the gravity wave activity we eventually want to infer.

5.2.1 Artificial inertial instability perturbations

A simple model of artificial inertial instability temperature perturbations (T'_{II}) was constructed here to first evaluate the ability of the background removals on isolated signals. In building the model, both theoretical knowledge about the spatial structure of stratospheric inertial instability effects (Dunkerton, 1981; Knox and Harvey, 2005) and the situation observed in the particular inertial instability case on 3 December 2015 were considered. For each location $\boldsymbol{x} = (x, y, z)$, the perturbation value is derived from a constant temperature perturbation T'_{II} and three independent spatial shape functions w_* to form the structure.

$$T_{II}(x, y, z) = T'_{II} \cdot w_{zonal}(x) \cdot w_{meridional}(y) \cdot w_{vertical}(z). \tag{5.6}$$

Following the findings from Dunkerton (1981), the first derivative of a Gaussian forms the meridional component:

$$w_{meridional}(y) = -\frac{y - y_0}{\beta} \exp\left(-\frac{1}{2}\left(\frac{y - y_0}{\beta}\right)^2\right) \tag{5.7}$$

The symmetric structure is centered around the latitude y_0 and defined by a characteristic width β.

In the vertical, a sinusoid with a given vertical wavenumber m fits the wave-shaped "pancake" structure. The lowest level with zero perturbation is defined by z_0.

$$w_{vertical}(z) = \sin(m(z - z0)) \tag{5.8}$$

For the zonal dimension, a step function with smoothed transition to zero is used here in order to restrict the structure to about a third of a latitude circle, because mid latitude inertial instability signals are often constrained in a so-called "channel" (Knox and Harvey, 2005). The step function is defined by the edge longitudes x_1 and x_2, that enclose the longitude range containing the nonzero perturbations, and a width α for the smooth transition from weights 0 to 1. The auxiliary parameters $\alpha_1 := x_1 + \alpha$ and $\alpha_2 := x_2 - \alpha$

abbreviate the notation:

$$w_{zonal}(x) = \begin{cases} 1 & x \in [\alpha_1, \alpha_2] \\ -\frac{1}{2}\cos\left(\pi\frac{x}{\alpha}\right) + \frac{1}{2} & x < \alpha_1, x \in [x_1, x_2] \\ -\frac{1}{2}\cos\left(\pi\frac{\alpha_2 - x}{\alpha}\right) + \frac{1}{2} & x > \alpha_2, x \in [x_1, x_2] \\ 0 & x \notin [x_1, x_2] \end{cases} \tag{5.9}$$

Table 5.1: Parameters adapted for this study in the artificial inertial instability perturbation model defined in Eqs. 5.6 to 5.9.

T'_{II} [K]	y_0 [°]	β [°]	x_1 [°]	x_2 [°]	α [°]	z_0 [km]	m [km^{-1}]
12	20	15	240	40	40	2	$\frac{2\pi}{12}$

In order to constrain the free parameters of the three shape functions, the idealized inertial instability is compared to the case of 3 December 2015. Based on a one-year survey of GPS-RO temperature anomalies and a climatological analysis of ERA-Interim data by Rapp et al. (2018b), this case of 3 December 2015 is a particular strong one. The vertical and horizontal scales of the inertial instability are representative for typical winter conditions. The same inertial instability signals can also be found in ERA5 and SABER temperatures, as will be discussed in more detail in Sect. 5.3. Figure 5.1 shows vertical, longitudinal and latitudinal cross sections as well as the zonal mean structure in a restricted longitude band (similar to Fig. 1b) by Rapp et al. (2018b)). The upper two rows depict the structures of the artificial data set based on Eqs. 5.6 to 5.9 and the parameters from Table 5.1 to generate the structure illustrated. The lower two rows give the corresponding plots from ERA5 temperature perturbations, calculated using vertical filtering with a fifth order Butterworth filter with a cutoff vertical wavelength of 15 km. (The Butterworth filter will be explained in more detail in Sect. 5.1.1.) The lower row also shows the modeled inertial instability signal as white contours for comparison with the ERA5 structures.

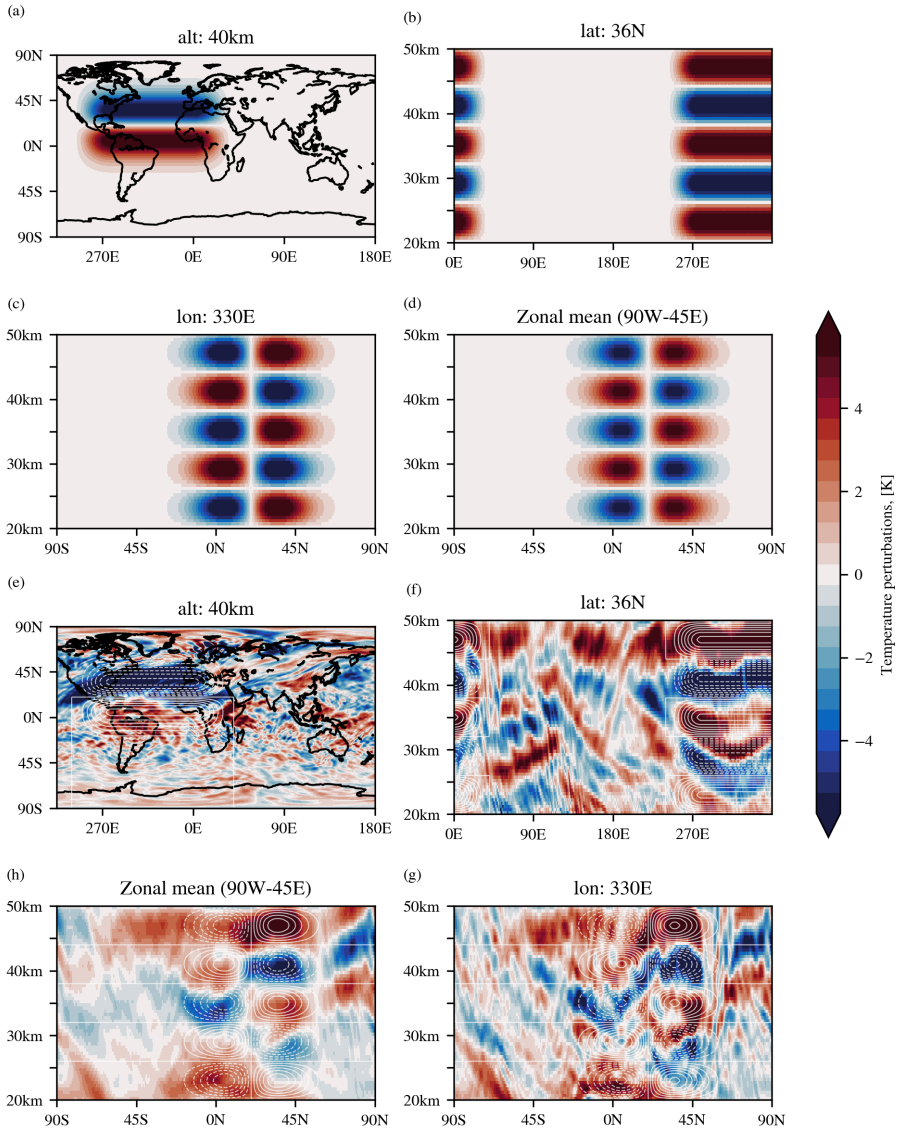

Figure 5.1: Cross sections of temperature perturbations of the artificial inertial instability, as defined in Sect. 5.2.1, are shown in the upper two rows: (a) A longitude-latitude cross section at 40 km altitude (black contours mark the coastlines), (b) a longitude-altitude cross section along the 36 °N latitude circle, (c) a latitude-altitude cross section along the 330 °E meridian and (d) the zonal mean in the longitude band from 90 °W to 45 °E (in the style of Fig. 1b) in Rapp et al. (2018b)). The lower two rows (panels (e) to (g)) shows the respective plots from the ERA5 temperature perturbation applying the fifth order Butterworth vertical filter with cutoff wavelength of 15 km as the plots two rows above. For easy comparison, the white contours in the lower row plots show the perturbation levels of the artificial data set in 2 K steps (solid lines indicate positive values, dotted lines negative values).

5.3 A case study on horizontal vs. vertical filtering in dealing with synoptic phenomena (inertial instabilities)

5.3.1 When is the background removed?

The purpose of this study is to evaluate the efficiency of the background removal when quantifying gravity wave signals scale-separated from a background atmosphere, which contains global scale variations caused e.g. by planetary waves and signals from inertial instabilities. To assess this, it is necessary to measure, whether spurious signals such as from inertial instabilities are still left in the inferred gravity wave perturbations. A simple option would be to evaluate whether the spurious remnants from inertial instabilities are significantly smaller than the targeted gravity wave signal. In this case the impact these remnants have would be insignificant, as of definition, and the removal could be deemed successful. However, the gravity wave signal is the targeted variable of the analysis and hence not known a priori. The gravity wave signal therefore cannot be used as a reference for a successful background removal.

For observations, a practical limit can be used instead. If the background remnants are smaller than the errors introduced by the measurement method and the retrieval, the signal would not be contaminated more by the background than by the instrument limitations anyways. Thus, the error of the instrument can be used as a realistic limit for filter efficiency.

The error budget of an atmospheric measurement instrument is usually described by precision and accuracy. In this context, accuracy describes “systematic” errors which are present in a similar magnitude on the entire data set and precision refers to the noise-like errors that affect a measured parameter randomly. In the observation of fluctuations, like gravity waves, the uncertainty is closer linked to the precision than to the accuracy of the instrument, since errors characterized by accuracy are removed together with the background. The magnitude of both accuracy and precision usually vary with altitude.

The SABER instrument, for instance, reaches best precision in the stratosphere with a minimal value of 0.3 K (Ern et al., 2018, and references therein). This threshold will

be used in the following as a measure for a successful background removal. For most of the stratosphere and for the mesosphere, this threshold is more conservative than the targeted detection limit for gravity waves.

5.3.2 Minimum appropriate filter cutoff for vertical and horizontal background removals

A spectral background removal will usually remove global-scale variations gradually, i.e. each global-scale process is described by several spectral components, and the more wavenumbers are removed the more of the background signal is removed as well. The success criterion defined above then allows us to identify threshold parameters for the cutoff vertical wavelengths or zonal wavenumbers for the respective background removals. On single process model data, like the artificial inertial instabilities defined in Sect. 5.2, the comparison against the threshold can be applied directly, since no gravity wave signal is present in the data. Here, the different filtering approaches are tested. In this context, the background removal is deemed to be successful when the mean squared temperature perturbations (cf. Eq. 5.5) fall below $0.09\,\mathrm{K}^2$.

Figures 5.2 and 5.3 show altitude-latitude cross sections of the zonal temperature variance (cf. Eq. 5.3) for the artificial inertial instability data (see Sect. 5.2). In Fig. 5.2, vertical filtering is applied with decreasing cutoff vertical wavelengths. The same is shown for horizontal filtering with increasing cutoff zonal wavenumbers, respectively, in Fig. 5.3. The layered “pancake” structures are a persistent feature, but eventually both methods, vertical filtering at cutoff wavelength 6 km (see Fig. 5.2(f)) and horizontal filtering at cutoff wavenumber 7 (see Fig. 5.3(f)) remove the signal with remaining remnants of less than $0.05\,\mathrm{K}^2$ magnitude. This value is smaller than the threshold of the success criterion we defined in Sect. 5.3.1.

The cutoff wavelengths and wavenumbers examined in this comparison were chosen to match values used in previous satellite studies. Fig. 5.2 (a) shows the structure after removing vertical wavelengths down to 15 km, as used by Rapp et al. (2018b). A similar level of reduction in the variance is reached by applying cutoff zonal wavenumber 0 in

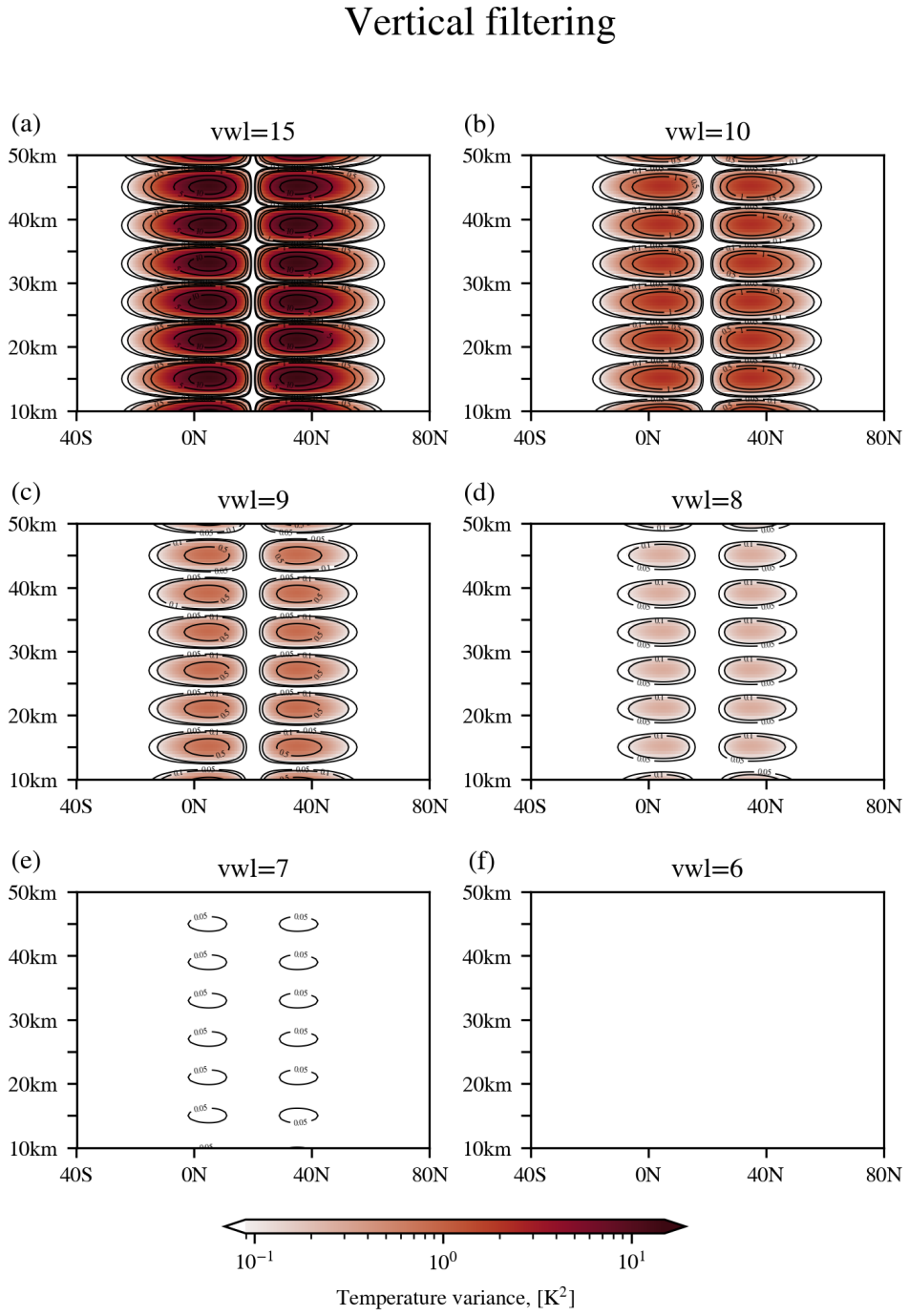

Figure 5.2: Zonal temperature variance of artificial inertial instability temperature perturbations after vertical filtering (fifth order Butterworth) with a cutoff wavelength of (a) 15 km, (b) 10 km, (c) 9 km, (d) 8 km, (e) 7 km and (f) 6 km.

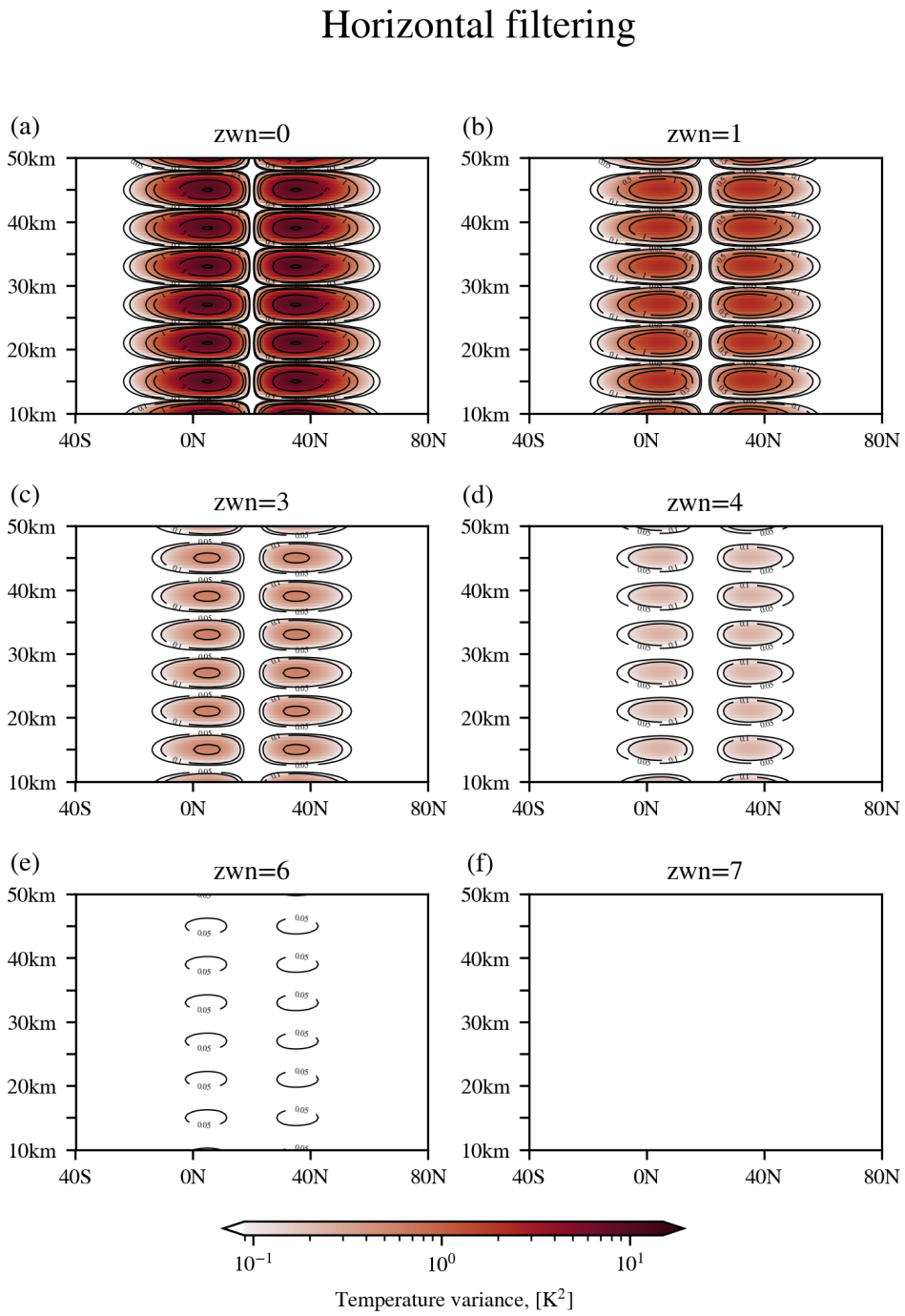

Figure 5.3: Zonal temperature variance of artificial inertial instability temperature perturbations after horizontal filtering (zonal mean with additional smoothing in meridional and vertical components) with cutoff zonal wavenumber (a) 0, (b) 1, (c) 3, (d) 4, (e) 6 and (f) 7.

the horizontal filtering case (see Fig.5.3 (a)). A cutoff wavelength of 10 km as used in Fig. 5.2(b) was used before by Tsuda et al. (2000) and Alexander and Barnet (2007) for vertical filtering. However, it has been shown that this cutoff removes a significant part of the gravity wave spectrum important for the middle atmosphere (Preusse, 2001; Preusse et al., 2008; Alexander et al., 2010). Here, horizontal filtering with cutoff zonal wavenumber 1 (see Fig. 5.3 (b)) gives a similar temperature variance result. On the other hand, Alexander et al. (2008a) applied horizontal filtering with a cutoff zonal wavenumber 3 using an S-transform approach. Fig. 5.3 (c) shows the temperature variance structure after removing zonal wavenumber 3. On the vertical filtering side, a similar result is achieved with a cutoff wavelength of 9 km (see Fig. 5.2(c)). The values of cutoff vertical wavelength 8 km or cutoff zonal wavenumber 4 were not used in previous studies, but the results show an intermediate value for the remnants (see Fig. 5.2(d) and 5.2(d)). The horizontal filtering with cutoff wavenumber 6 (see Fig.5.3 (e)) is the first to fall below the precision threshold of 0.09 K^2. A number of studies used this cutoff previously (e.g. Fetzer and Gille, 1994; Preusse et al., 2002; Ern et al., 2018), since zonal wavenumber 6 is close to the sampling limit for infrared limb sounders on low earth orbits. The counterpart magnitude of the vertical filtering variance here is found at a cutoff wavelength of 7 km (see Fig.5.2 (e)). Finally, with vertical cutoff at 6 km and horizontal cutoff at 7, the zonal variance decreases even to $<0.05\,K^2$ (see Fig.5.2 (f) and 5.3 (f)).

5.3.3 A compromise between removing inertial instability remnants and preserving gravity wave signals in ERA5 temperatures

The upper row of Fig. 5.4 shows zonal mean structures of temperature perturbations (cf. Eq. 5.4) from ERA5 data on 3 December 2015, 00:00 UTC, after applying different filterings. As an indication for significance, the standard deviation of the zonal means is shown as well, calculated as $\sqrt{\mathrm{var}(T')}$ (cf. Eq. 5.3), in the lower row. On the left, the zonal mean temperature perturbation for vertical filtering with cutoff wavelength 15 km (cf. Fig. 5.4(a)) displays strong layered bands of vertically alternating positive and negative peaks at the equator, i.e. spanning from 20 °S to 20 °N, as well as in the midlatitudes

approximately between 30 and 45 °N. This shows the presence of the inertial instability also in the ERA5 data. Equatorial values are 180 °-phase-shifted with respect values at the midlatitudes, as expected from theory (Dunkerton, 1981) and found in previous inertial instability observations (Hayashi et al., 1998; Smith and Riese, 1999; Rapp et al., 2018b). The midlatitude stack widens in meridional extent with altitude between 20 and 45 km, while the tropical feature narrows. The main pancake structures are significant, i.e. larger than the corresponding standard deviations (cf. Fig. 5.4(d)).

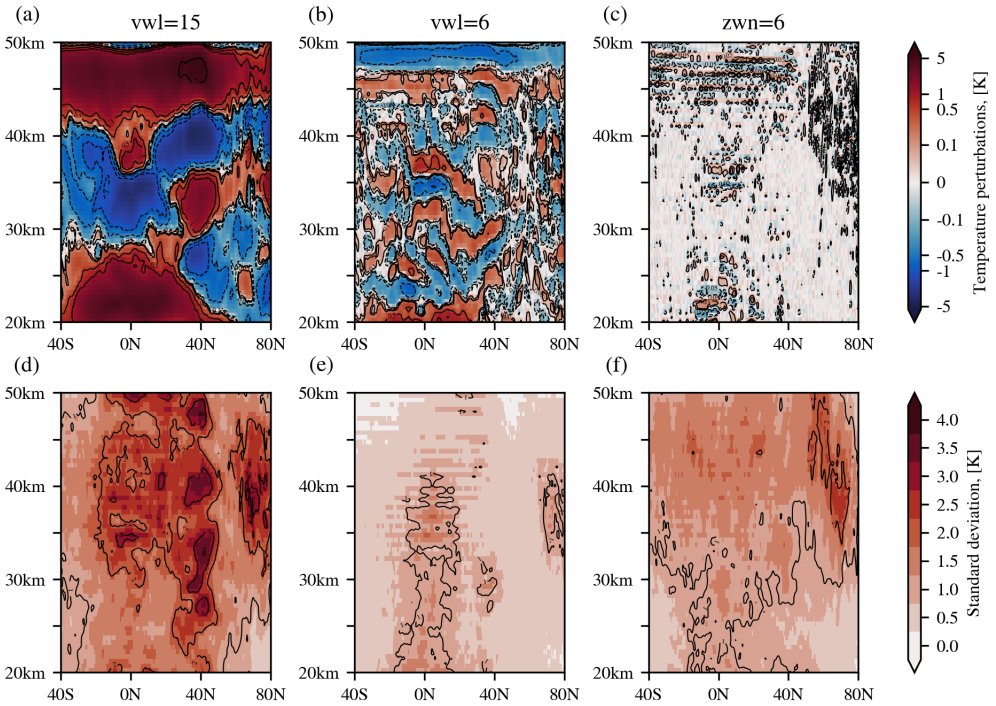

Figure 5.4: Zonal mean temperature perturbations for ERA5 temperatures for 3 December 2015, 00:00 UTC after (a) vertical Butterworth filtering with 15 km cutoff wavelength, (b) vertical Butterworth filtering with 6 km cutoff wavelength and (c) horizontal FFT filtering with cutoff zonal wavenumber 6 and additional vertical and meridional smoothing in the upper row. The lower row – (d), (e) and (f) – shows the respective standard deviations of (a), (b) and (c). Contours show indicated temperature perturbation levels to highlight the structure.

The middle and right columns in Fig. 5.4, show the zonal mean temperature perturbations for the cutoffs, which provide the best removal of our artificial inertial instability signals (see Sect. 5.3.2). In the middle (Fig. 5.4(b) and (e)), vertical filtering with a cutoff

wavelength of 6 km was used to remove the background. The mean perturbations still show layered structures, in particular in the latitude bands where the pancake structures were found for a cutoff at 15 km. The magnitudes, however, are less than 1 K and overall insignificant. In the tropics (approximately from 20 °S to 20 °N), higher values in the standard deviation point to signals that have smaller vertical scales than the removed inertial instability. The symmetric structure around the equator with a smooth, Gaussian-like peak and a half-width of approx. 10 ° indicates that this maximum may be attributed to Kelvin waves (Smith et al., 2002). On the right (Fig. 5.4(c) and (f)), the data was treated with a horizontal filtering using a cutoff wavenumber 6. Except for a few spots above the tropical tropopause (around 5 °S and below 25 km) and at high latitudes (north of 60 °N) and high altitudes (above 35 km), the zonal mean does not show structures exceeding 0.01 K. The standard deviation, however, shows enhancement at higher altitudes and in particular in a wide range of latitudes associated with the polar jet. Though there may be some structures caused by horizontal gradients at the vortex edge, this enhancement spans approx. 30 ° of latitude and hence indicates real gravity wave activity. This feature is also present in the two other standard deviation plots and will be discussed in more detail later on.

As already shown in the Sect. 5.3.2, the quality of a spectral filter is highly dependent on the cutoff length scale used. Ideally, a transition between mesoscale and synoptic-scale fluctuations (previously referred to as “spectral gap”) can be identified, where the temperature variance will be insensitive to the cutoff length separating gravity wave activity at small- and mesoscales from global-scale inertial instability signals. However, such a transition is not necessarily present in the stratospheric temperature variance, and very unlikely to be found in the troposphere.

With its dense regular sampling, the realistic global ERA5 temperature data allow a sensitivity study with respect to temperature variances on the cutoff length scales for a wide range of cutoffs of both vertical and horizontal filtering. Figure 5.5 shows the dependence of temperature variances on the background removal. The variances are calculated using Eq. 5.5, but here the average is defined over a domain from 90 °W

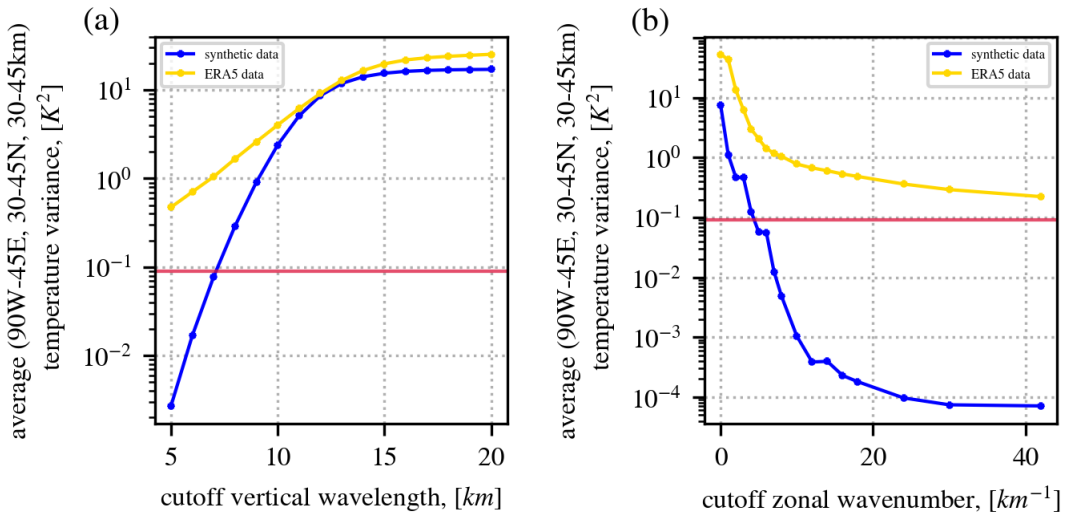

Figure 5.5: Dependence of mean temperature variance in a box of 90 °W to 45 °E longitude, 30 °N to 45 °N latitude and 20 to 50 km altitude on the characteristic cutoff length scale for different filtering methods: (a) vertical fifth order Butterworth filter with cutoff in the vertical wavelength and (b) horizontal FFT filter with additional smoothing in vertical and meridional direction and cutoff in zonal wavenumber. In each plot, the blue line represents artificial inertial instability perturbations and the yellow line shows the corresponding results for ERA5 temperatures. The red horizontal line marks 0.09 K^2 as precision threshold of the SABER instrument.

to 45 °E longitude, 30 to 45 °N latitude and 20 to 50 km altitude instead of one latitude circle. This region is chosen, as Fig. 5.1 shows this domain to contain the largest inertial instability signal. The Figure shows the scaling behaviour for vertical filtering with cutoff vertical wavelength in the range 5 to 20 km in panel (a) and horizontal filtering from cutoff zonal wavenumber 0 to 42 in panel (b). The yellow curve shows results for ERA5 data at 3 December 2015 at 00:00 UTC and the blue curve for the artificial inertial instability constructed as described in Sect. 5.2.1. The blue curve can be interpreted as a reference of how a pure inertial instability signal is affected by the background removals. Different sensitivities of the mean temperature variance for more rigorous filtering are evident.

For vertical cutoff wavelengths larger than 15 km, the averaged variance of ERA5 temperatures increases slowly with a linear gradient. In the same cutoff wavelength range, the variance stays mostly constant in the artificial inertial instability perturbations. The gradient becomes gradually steeper in both data sets between cutoffs at 15 and 10 km.

In this range, where both data sets show similar behaviour, the averaged temperature variance is likely dominated by the inertial instability signal. The gradient for the ERA5 data remains similar also for cutoff vertical wavelengths shorter than 10 km while for the artificial inertial instability data the decrease continues to steepen. This different behaviour indicates that the variance evolution for smaller cutoff wavelengths is dominated by a different dynamic process, like gravity wave activity, missing in the artificial inertial instability perturbation data.

The sensitivity of the temperature variance to increasing cutoff zonal wavenumbers in horizontal filtering shows a range of cutoff values where both the realistic ERA5 data as well as the artificial inertial instability perturbations behave in a similar manner. From cutoff zonal wavenumber 1 to 6, both curves of averaged temperature variances are decreasing fast, indicating the dominance of the inertial instability signal in the variance evolution. At wavenumber 6 there is an abrupt change in the variance decrease in ERA5 data, and the slope gets continuously flatter between wavenumber 6 and 12. At wavenumbers above cutoff zonal wavenumber 12 the gradient is about constant. In comparison, the variances decrease of the artificial perturbations continues up to wavenumber 12 and then almost directly stagnates at extremely small averaged temperature variances. That the averaged temperature variance for the synthetic inertial instability stays constant at wavenumbers 2 and 3, wavenumbers 5 and 6 and wavenumbers 10 and 12 in the artificial data is likely connected to the regular structure of the modeled inertial instability, which spans over approximately a third of the latitude circle.

Analogously to the vertical filtering case, we interpret similarities and differences in the variances of the two data sets. The variance is likely dominated by the inertial instability influence up to wavenumber 6. For wavenumbers larger than 7 gravity waves are taking over as the dominant process, though up to wavenumber 12 there may be remnants of the inertial instability. The slow decrease at high wavenumbers shows that eventually energy is taken out of the gravity wave scales as well.

5.3.4 Effects of spurious remnants from background removals in quantities relevant for gravity wave climatologies

The diagnostics shown for gravity wave climatologies from measurement or model data are usually energy quantities like gravity wave potential energy densities (Tsuda et al., 2000; de la Torre et al., 2006; Rapp et al., 2018b) or gravity wave momentum fluxes (Ern et al., 2004; Wang and Alexander, 2010; Alexander, 2015; Ern et al., 2018). These quantities are not calculated from gravity wave variances (Eq. 5.3), but using a spatial average of the the squared temperature perturbation (Eq. 5.5). Figures 5.6 and 5.7 show the zonal mean structure of ERA5 squared temperature perturbations for vertical and horizontal filtering employed with different scales of the background removal. Similar to Figs. 5.2 and 5.3, the different cutoff length scales are mostly chosen according to levels that have been used in previous studies. For the vertical filtering, only results for cutoff vertical wavelengths of 15 km (Fig. 5.6(a)), 10 km (Fig. 5.6(b)) and 6 km (Fig. 5.6(c)) are included. The first two values were used in studies by other groups before, while the 6 km cutoff marks the transition point in the sensitivity curve (Fig. 5.5) discussed above where the gravity wave signal dominated the temperature variance in the stratosphere. Cutoff zonal wavenumbers at 0, 1, 3, 4, 6, and 7 as used before for the artificial data were selected. Furthermore, the higher order cutoff values at wavenumber 12, 18 and 42 complete the figure to include an evaluation of how the structures are changing if more wave components are removed then necessary to eliminate the inertial instability structures.

In the following, four structural features and their evolution under different cutoffs are highlighted in the discussion of the two background removal. First, Fig. 5.6(a) shows a typical pancake structure in the midlatitude stratosphere (approximately between 30 and 45 °N and above 25 km altitude) associated with the inertial instability (Rapp et al., 2018b). A corresponding but isolated stack is present above the equator between 30 and 40 km altitude.

The isolated structures merge into one broad sheet of perturbation at altitudes a few kilometers below the stratopause and upwards. Decreasing the cutoff wavelength in the

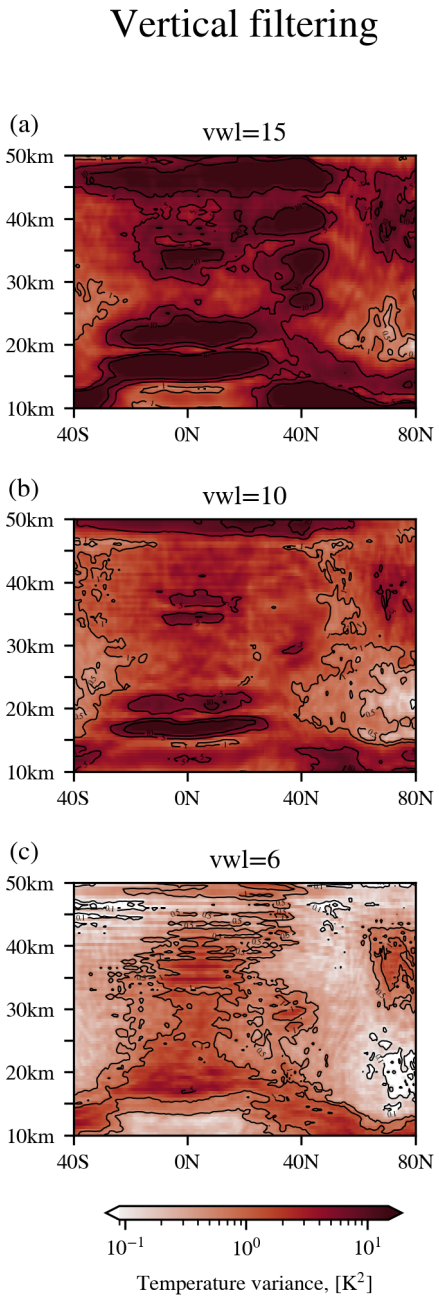

Figure 5.6: Vertically filtered (fifth order Butterworth) zonal mean squared temperature perturbations (cf. Eq. 5.5) with a cutoff wavelength of (a) 15 km, (b) 10 km and (c) 6 km of ERA5 temperatures on 3 December 2015, 00:00 UTC.

vertical filtering reduces the pancake structure at midlatitudes in a way that it is not further recognizable in the results from 6 km vertical filtering. The tropical band of the structure is more persistent while being reduced in magnitude, but remaining especially strong at

35 to 40 km altitude. In addition, a more rigorous vertical filtering seems to narrow the vertical distance between the variance peaks. As discussed in Sect. 5.3.3, the remaining structures may be caused by tropical wave modes and, in particular, by Kelvin waves.

In comparison, the horizontal filtering results show less evidence for the typical pancake structure, both at midlatitudes and in the tropics. In the tropics, above 30 km altitude some layered structures emerge for low cutoff wavenumbers (cf. Fig. 5.7(a) and (b)). The midlatitudes, however, are dominated by a strong ($>$10 K^2), large-scale perturbation structure that does not show the stacked pancake features and is likely connected to remaining Rossby wave signals. At cutoff zonal wavenumbers 3 and 4 (cf. Fig. 5.7(c) and (d) respectively), the Rossby wave feature is mostly removed and some pancake-like structures are found in the midlatitudes which are already reduced compared to the vertical filtering with cutoff wavelength 15 km. In the tropics, no clear pancake structure remains while increasing the cutoff zonal wavenumber further, but a small local maximum in Fig. 5.7 (e) at 40 °N and 30 km altitude could still be associated with the pancake structures.

At altitudes above 20 km, the general structure continues to decrease in magnitude, but remains very similar in structure for wavenumbers 6 and larger. This is consistent with gravity waves at a wide range of different scales causing these features. Particularly pronounced is a second structure between 60 °N and 80 °N and 30 to 50 km altitude, which shows still enhanced perturbations at wavenumber 42 (cf. Fig. 5.7 (i)). This is likely associated with gravity waves in the winter polar vortex, and Rapp et al. (2018b) attribute a major part of the feature to gravity wave sources at Greenland. The structure is also found in the vertical filtering results, but it extends less far into higher altitudes as well as less wide equatorwards. In general, the perturbation structures after vertical filtering (Fig. 5.6) show a few degree latitude wide gap of comparably small perturbations around 60 °N. This anomaly is located approximately in the center of the polar night jet where we expect a predominance of long vertical wavelength of gravity waves. The feature is not present in the horizontal filtering results of Fig 5.7. In fact, at this location, horizontal filtering indicates a maximum of squared temperature perturbation.

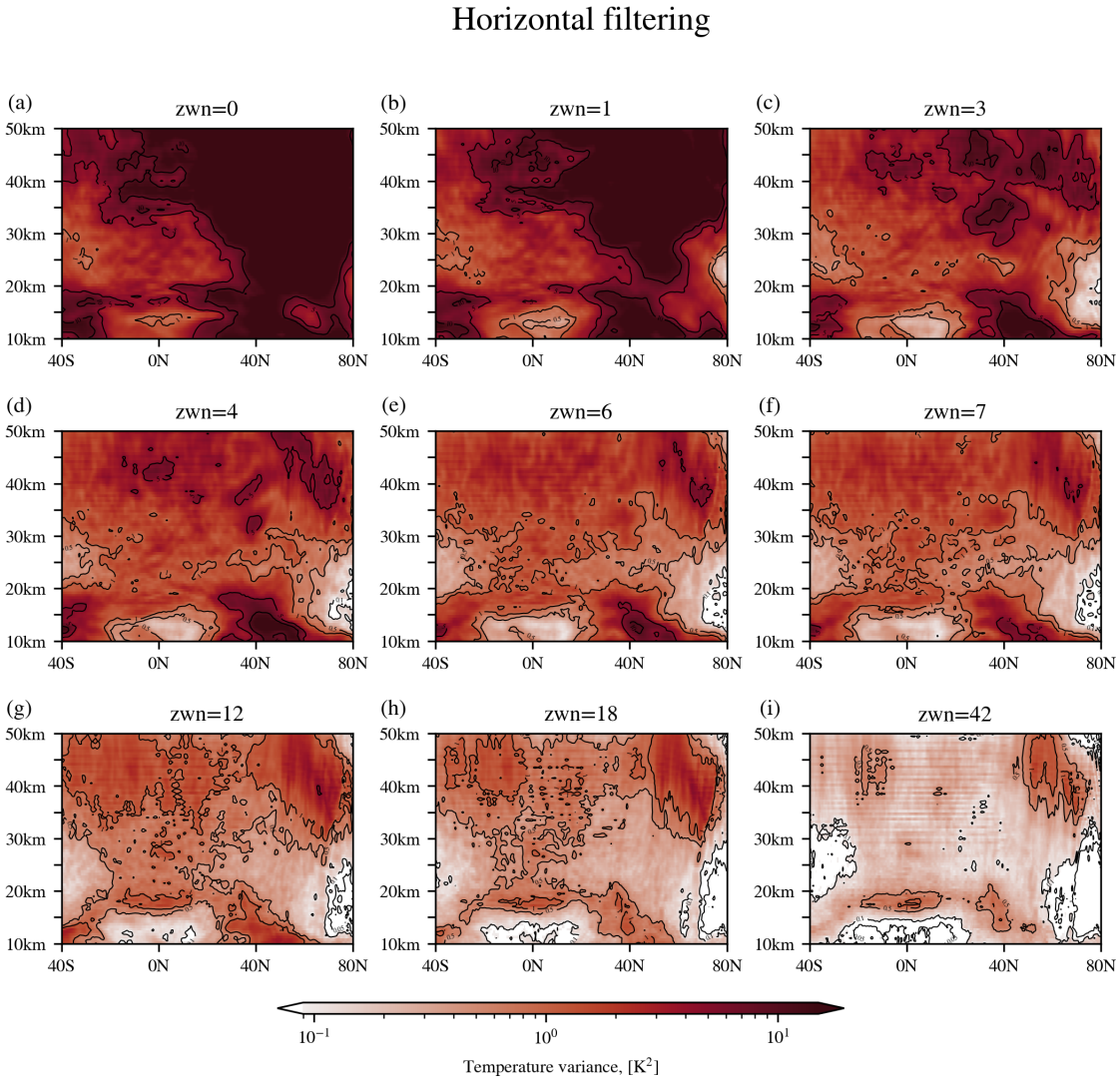

Figure 5.7: Horizontally filtered (with additional smoothing in meridional and vertical components) zonal temperature variance of ERA5 temperatures on 3 December 2015, 00:00 UTC, with cutoff zonal wavenumber (a) 0, (b) 1, (c) 3, (d) 4, (e) 6, (f) 7, (g) 12, (h) 18 and (i) 42.

For very low cutoff zonal wavenumbers, the high-latitude maximum is concealed by a larger perturbation due to Rossby waves in middle and high latitudes. From cutoff wavenumber 6, it is not distorted by pancake-like, overlaid structures anymore. Then, the overall shape of the enhanced temperature perturbation distribution is not changed up to a cutoff wavenumber 18 and also keeps roughly the same magnitude. This indicates that

the horizontal wavelengths of the waves amount to at most $\sim$1 000 km as Coriolis force arguments for gravity waves at these latitudes would suggest (Alexander et al., 2002; Preusse et al., 2006). The very strong horizontal filtering with cutoff zonal wavenumber 42 still shows the feature but with decreased magnitude, which indicates that part of the gravity wave spectrum is also removed by the background removal.

Below 20 km altitude, the tropical tropopause and the tropopause inversion layer show up distinctively in the vertically filtered data, depicted by a enlongated, strong perturbation signal spanning all the way from 30 °S to 30 °N between 15 and 25 km (cf. e.g. Fig. 5.6(a)). Rapp et al. (2018a) explained this third structure with shortcomings of the vertical filtering to identify background temperature structures like the tropical tropopause with the short vertical length scale. Even a rigorous vertical filtering with a cutoff wavelength of 6 km retains the signal. This problem is similar to the misinterpretation of inertial instability perturbations due to their small vertical wavelength. In comparison, the horizontal filter is removing a large part of the tropopause signal from the perturbations already with cutoff wavenumber 0, i.e. only removing the zonal mean. This could be explained by the tropical tropopause and the tropoause inversion layer being rather stable in altitude over all longitudes. However, even at zonal wavenumber 42, the remnant structure is still larger than the gravity wave fluctuations above and below, indicating that the remnants of the tropopause still masks the gravity wave signal.

Finally, all of the results show enhanced temperature perturbations in the troposphere below 15 km around 40 °N. With cutting more rigorously, both filtering methods reduce the zonal mean magnitude of this feature, but it is never fully removed, even with high horizontal wavenumber cutoffs of 18 or 42. The dynamically active region of the troposphere is very difficult for all gravity wave background removals due to the large and possibly abrupt variation of the temperature over small distances. In the troposphere a wide spectrum of Rossby waves up to high zonal wavenumbers exists, which is filtered around the tropopause according to the Charney-Drazin criterion (Charney and Drazin, 1961). Accordingly, the stratospheric background atmosphere is dominated by planetary waves with zonal wavenumbers smaller than 4 (e.g. Domeisen et al., 2018; Barnett and

Labitzke, 1990; Pawson and Kubitz, 1996), consistent with the findings in this paper. In order to investigate altitudes below 20 km from LEO infrared sounders, higher wavenumbers than wavenumber 6 have to be taken into account. Even at high zonal wavenumbers, the results will need further validation, which, however, is beyond the scope of this study.

5.3.5 Horizontal and vertical filtering on a one-year time series of SABER measurements

In the previous sections, a case study for a particular, strong inertial instability event was considered. In order to evaluate whether the results are representative, a corresponding filtering analysis of one year of SABER data is presented in the following.

As already addressed in Sect. 3.3, SABER data is much sparser than ERA5 and the analysis has to rely on a more complex horizontal filtering approach. The method is taylored to the regular global sampling pattern of orbiting limb-sounders with measurement tracks quasi-parallel to the satellite orbit track. Satellite observations with different sampling methods may need slightly different approaches. For instance, longitude-time spectra can be calculated from GPS-RO profiles; this has been done by Alexander et al. (2008b), for the analysis of Kelvin waves using data from the Constellation Observing System for Meteorology Ionosphere and Climate (COSMIC). Such spectra could be used for background removal, but more care would have to be taken because the number of data points available for a given latitude will vary strongly.

Like Fig. 5.4 for ERA5, Fig. 5.8 shows the zonal mean temperature perturbations and corresponding standard deviations now from SABER data. On the left (Fig. 5.8(a) and (c)), the results from the vertical filtering with cutoff wavelength of 15 km are presented. Again, there are the pancake structure in the tropics and midlatitudes characteristic of the inertial instability. Since SABER pointed southward on 3 December 2015, data does not cover high latitudes (poleward of 50 °N) for this case. The standard deviation show layered structures as well, which are especially strong in the midlatitudes. On the right (Fig. 5.8 (b) and (d)), the results from the time-horizontal filtering for the SABER data using cutoff zonal wavenumber 6 that the inertial instabilities remnants have been removed

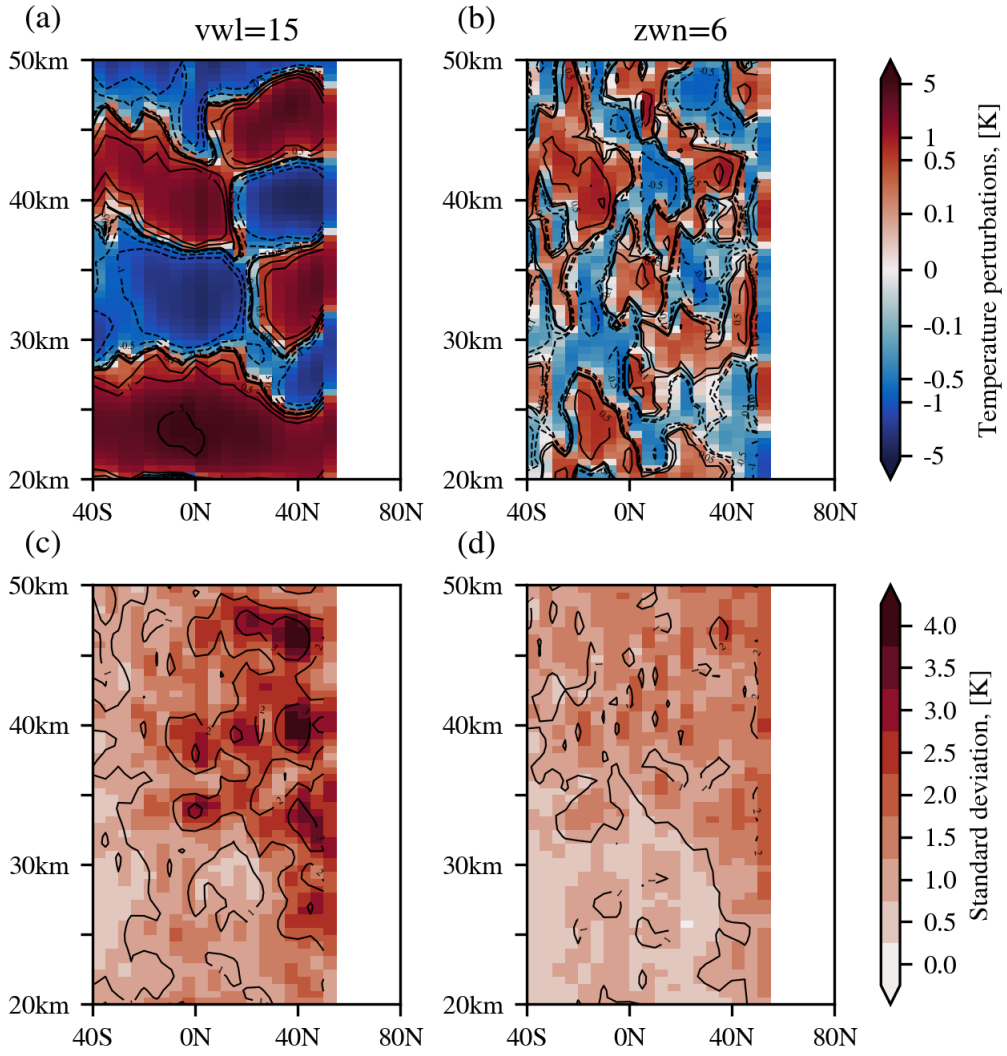

Figure 5.8: Zonal mean temperature perturbations and corresponding standard deviations of SABER data. The upper row shows the mean perturbation from (a) vertical filtering (fifth order Butterworth) with cutoff vertical wavelength of 15 km and (b) horizontal filtering with the method from Ern et al. (2011) with cutoff zonal wavenumber 6 and period $\approx$1.4 d. The lower row shows in (c) and (d) the corresponding standard distributions of (a) and (b).

successfully. Over the course of one day, SABER data only contains 32 measurement points along one latitude circle and thus provides much weaker statistics than the ERA5 data set. This presumably explains remnant values of mean temperature perturbations in the SABER results, which, however, do not show the characteristic “pancake” struc-

ture typical for inertial instabilities and are mostly below 0.5 K. In the standard deviation, more activity in the winter hemisphere than in the summer hemisphere is evident. This is consistent with the general understanding of source activation and global distributions of gravity waves (Fritts and Alexander, 2003; Geller et al., 2013). It is also supported by the study in Chapter 6 which discusses gravity wave propagation into the winter polar vortex. Overall, magnitudes are lower than in Fig.5.8 (a) and (c). In vertical filtering, most of this distribution was distorted by the large, layered features of the inertial instability.

Figure 5.9 shows daily averages of mean zonal squared temperature perturbations (cf. Eq. 5.5) in a midlatitude box from 90 °W to 45 °E and from 30 °N to 45 °N for one year of SABER temperature data (July 2015 to June 2016). The upper panel shows results from a vertical Butterworth filter with 15 km cutoff wavelength, and the lower panel presents results form horizontal background removal with a cutoff zonal wavenumber 6.

Throughout the entire year, the vertically filtered data shows a pronounced signal above the tropopause, i.e. between 20 and 25 km, and around the stratopause, i.e. between 40 and 50 km altitude. Furthermore, this data set exhibits remnant pancake structures persisting for several days through the northern hemisphere winter (December to mid February). This is consistent with favourable conditions for inertial instability particularly around the winter solstice (Rapp et al., 2018b).

After horizontal filtering some wave-like structures are remaining, however smaller in magnitude and of shorter duration. These structures indicate very active gravity wave events dominating the average in the domain. Also, the horizontal background removal does not show the very strong signals associated with the tropopause and stratopause.

5.4 Conclusion

The analysis data ranging from satellite temperature measurements to global reanalysis snapshots for resolved gravity waves relies on an initial scale separation to separate the targeted gravity waves from larger scale structures, like planetary waves and inertial instabilities. In recent studies, concern was raised that inertial instabilities might not be properly removed in generating gravity wave climatologies and thus cause spurious sig-

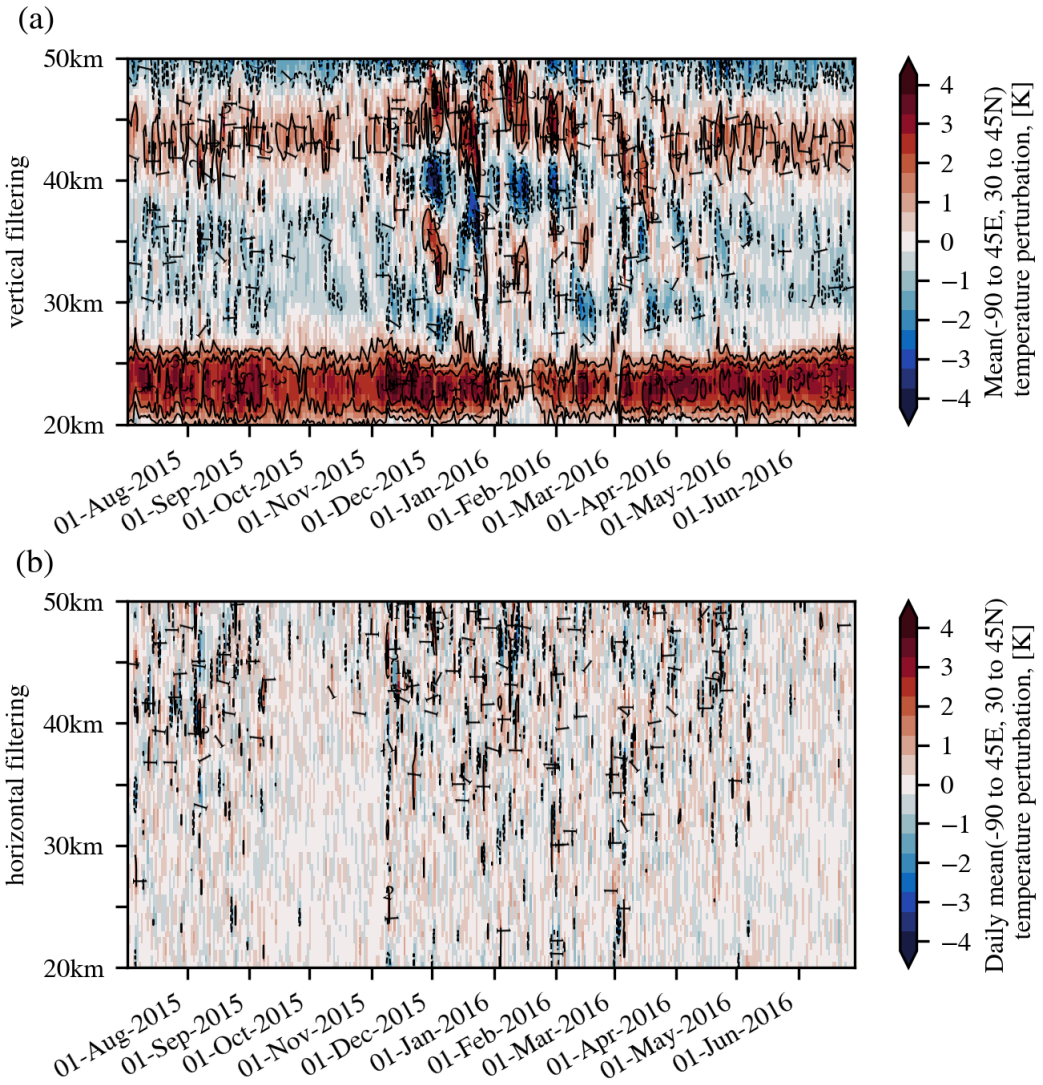

Figure 5.9: Time series of daily mean temperature perturbation profiles from SABER in the midlatitude box, 90 °W to 45 °E longitude, 30 to 45 °N latitude, for one year (1 July 2015 to 30 June 2016) after (a) vertical Butterworth filtering with 15 km cutoff wavelength and (b) horizontal filtering (zonal mean with additional smoothing in meridional and vertical components) with cutoff wavenumber 6. Contours show the indicated value of daily mean box mean temperature perturbation.

nals in the derived distributions (Rapp et al., 2018b; Harvey and Knox, 2019). Therefore, the subject of this study is to assess the capability of horizontal and vertical spectral background removals to isolate gravity waves from inertial instability effects. An additional aim in this context was to determine optimal cutoff length scales for the background removal.

In this attempt, the focus here lies in a particularly strong inertial instability event on 3 December 2015, which was previously discussed in the study of Rapp et al. (2018b). As test data, ERA5 reanalysis temperatures, SABER temperature observations and a synthetic data set containing only an artificial inertial instability signal were used. In general, a background removal is considered successful if the gravity wave variances dominate over the remnants of the removed inertial instability. For practical purposes we also introduced as a second criterion that the background removal is considered successful if the remnants of the removed inertial instability are smaller than the precision of the instrument from which we determine the climatology. The advantage of this criterion is that the gravity wave distribution does not need to be known a priori.

In the first step, the vertical and horizontal filtering results for the artificial inertial instability signal were compared. Zonal mean gravity wave temperature perturbations and zonal mean variances show that both methods are in principle capable to remove an inertial-instability-like perturbation to a limit that it falls to a level below the SABER precision threshold. However, in vertical filtering all fluctuation larger than 7 km had to be eliminated in the vertical to achieve a sufficient signal reduction. This would lead also to the removal of a major part of the gravity wave spectrum. A comparable level of removal after horizontal filtering was achieved with a cutoff zonal wavenumber of 6, which is no restriction to the gravity wave analysis, in particular if momentum flux is considered.

The investigation of ERA5 data shows that for the midlatitude stratosphere gravity waves dominate over inertial instability signals for vertical cutoff wavelengths shorter than about 10 km and for horizontal cutoff wavenumbers larger than 6. After vertical background removal remnants of the stratopause remain. In addition, the tropical stratosphere showed perturbations over all altitudes from 20 to 45 km that indicate Kelvin wave activity. Horizontal filtering, in contrast, removes both effects. Horizontal filtering is also more capable in dealing with the tropical tropopause, but remnants larger than the average gravity wave variance remain. In the subtropical troposphere and lowermost stratosphere zonal wavenumbers larger than 18 are required to reduce the signal of Rossby waves. Further consideration will be needed in future, if data sets should be evaluated for such lower alti-

tudes, as well. A zonal wavenumber filter applying wavenumbers higher than 18 removes already part of the gravity wave spectrum.

A one year analysis of SABER data reveals inertial instability signals for the vertical filtering, but no evidence for inertial instabilities after horizontal filtering. Hence, the case study of one inertial instability event is representative. Considering existing satellite climatologies, such data sets, which are based on time-longitude spectra including zonal wavenumber 6, are likely free of the influence of large scale inertial instabilities. This includes for instance the GRACILE climatology (Ern et al., 2018) and studies based on this or similar data sets. Some influence is expected on data sets generated by vertical filtering with a 10 km cutoff wavelength, such as GPS investigations by Tsuda et al. (2000); de la Torre et al. (2006). In addition, an influence of Kelvin waves is expected for low latitudes. The relatively short cutoff wavelength applied in these studies, however, is also cutting deep into the gravity wave spectrum, in particular for high latitude winter conditions. Gravity wave temperature perturbations calculated using vertical filtering with a 15 km cutoff wavelength on the other hand are dominated by inertial instability depending on season and geographical region, as was already shown by Rapp et al. (2018b).

In conclusion, for the removal of a background containing inertial instabilities and gravity waves, horizontal spectral filtering with a zonal wavenumber of 6 or higher provides the best results. It is therefore recommended to use such an approach where the data allow for it. For altitudes around the tropopause, larger zonal wavenumbers are required, but zonal wavenumbers larger than 18 reduce the fraction of retrievable gravity waves in the stratosphere greatly.

Chapter 6

A case study of wave source identification and propagation paths at the southern hemisphere winter polar vortex

In this chapter, the methods introduced in Chap.4 are applied to investigate which propagation pathways and source distributions are important for gravity waves in southern hemisphere winter. For this reason, a case study presented by Ehard et al. (2017) from the austral winter of 2014 is investigated again. The authors noted on an apparent contraction: In the study, waves observed by the COmpact Rayleigh Autonomous Lidar (CORAL) over Lauder, New Zealand, have been shown to propagate mainly vertically up to about 40 km altitude where they are refracted by horizontal wind gradients and propagate southward into the polar vortex above 40 km altitude. However, AIRS observations also shown in this context feature a large-amplitude event of more than 2 million km^2 extent spanning from the South Island of New Zealand southeastward onto the ocean. This wave field is observed far out over the ocean already in the lower stratosphere (25 km and below) and, thus, cannot follow the same oblique propagation paths as the gravity waves observed by the CORAL lidar over Lauder at 40 km altitude.

Beyond that case study, model investigations and satellite observations point to a continuous poleward propagation and focusing of gravity waves into the stratospheric polar vortex in the mid stratosphere and higher up. Using ray-tracers with a global launch distribution, Sato et al. (2009); Preusse et al. (2009a) and Kalisch et al. (2014) investigated the importance of oblique propagation for the gravity wave distributions in the upper stratosphere and mesosphere. Such modeling results are strongly supported by the patterns revealed from semiannual and terannual variations in a long time series of GWMF inferred from SABER temperature measurements (Chen et al., 2019). In contrast, superpressure balloon observations show strong GWMF around 60° S already at approximately 18 to 20 km altitude around the lower edge of the stratopspheric polar vortex (Hertzog et al., 2008; Geller et al., 2013). Also HIRDLS observations as low as 20 km altitude (Geller et al., 2013; Ern et al., 2018) show that the momentum flux maximum is located further south, around 60°S, than the storm tracks which occur mostly around 40°S. The realistic implementation of oblique propagation from mid-latitude sources, like the tropospheric jets, orography and the storm tracks (Holt et al., 2017), into the polar vortex (Wu and Eckermann, 2008) is the most promising approach to fixing the Missing gravity wave drag problem in climate models. The timing of the southern polar vortex break-down and the related ozone loss period is one of the major shortcomings in most current climate models.

Section 6.1 introduces the wave event, that was observed on 1 August 2014 by briefly reviewing the synoptic situation and the perturbation fields over the ocean. Subsequently, the wave field is characterised using the S3D method as introduced in 4.1. Section 6.2 collects the results from propagating these characterised waves from the stratosphere backwards to their likely sources using the GROGRAT ray tracer (cf. Sect.4.2). The implications of these results for gravity wave propagation into the southern hemispheric polar vortex are discussed in Sect. 6.3.

6.1 Gravity wave characterization in the stratosphere

6.1.1 Synoptic situation and the wave field

The prevalent meteorological situations occurring during this campaign period are described in detail by Gisinger et al. (2017): in the troposphere, a meandering of the jet is caused by synoptic-scale Rossby waves displacing the jet core at times to latitudes north of New Zealand. On the 31st of July and 1st of August 2014 this resulted in incident flow to the southeast, perpendicular to the New Zealand mountain ridge in the troposphere. In the lower stratosphere, the wind turned to eastward and in the mid stratosphere the flow was also eastward and the jet core farther south between 50°S and 75°S (Ehard et al., 2017).

Figure 6.1 shows horizontal and vertical cross sections through the gravity wave field found on 1 August 2014, 12:00 UTC, in the ECMWF-IFS temperatures. Temperature perturbations are inferred with the zonal spectral filtering described in Sect. 5.1 and all waves up to a zonal wavenumber of 18 are attributed to the background. At all altitudes, a gravity wave field is stretching from the southern tip of New Zealand's southern island far out southeast from New Zealand over the ocean.

At 25 km altitude (Fig. 6.1a), there is a large field of enhanced gravity wave amplitudes spanning from 170°E to 150°W and from 40°S to 65°S. This is the target altitude for spectral analysis in Section 6.1.2 in this study. The gravity wave field is rather isolated and there are only few structures to the north and south as well as upstream of 160°E for latitudes south of 50°S. Above New Zealand's South Island, mountain wave structures are visible. Most pronounced is a small patch with high amplitudes in the south of the South Island with, at 25 km altitude, north-south orientation of the phase fronts. Also weaker structures above the northern part of the South Island have north-south alignment of the phase fronts and are not parallel to the coast and thus the main mountain ridge. This orientation has been attributed to turning of the phase-fronts by horizontal refraction (Ehard et al., 2017). A resulting balance of the likewise turning background winds keeps the waves above the island of New Zealand as is discussed in detail by

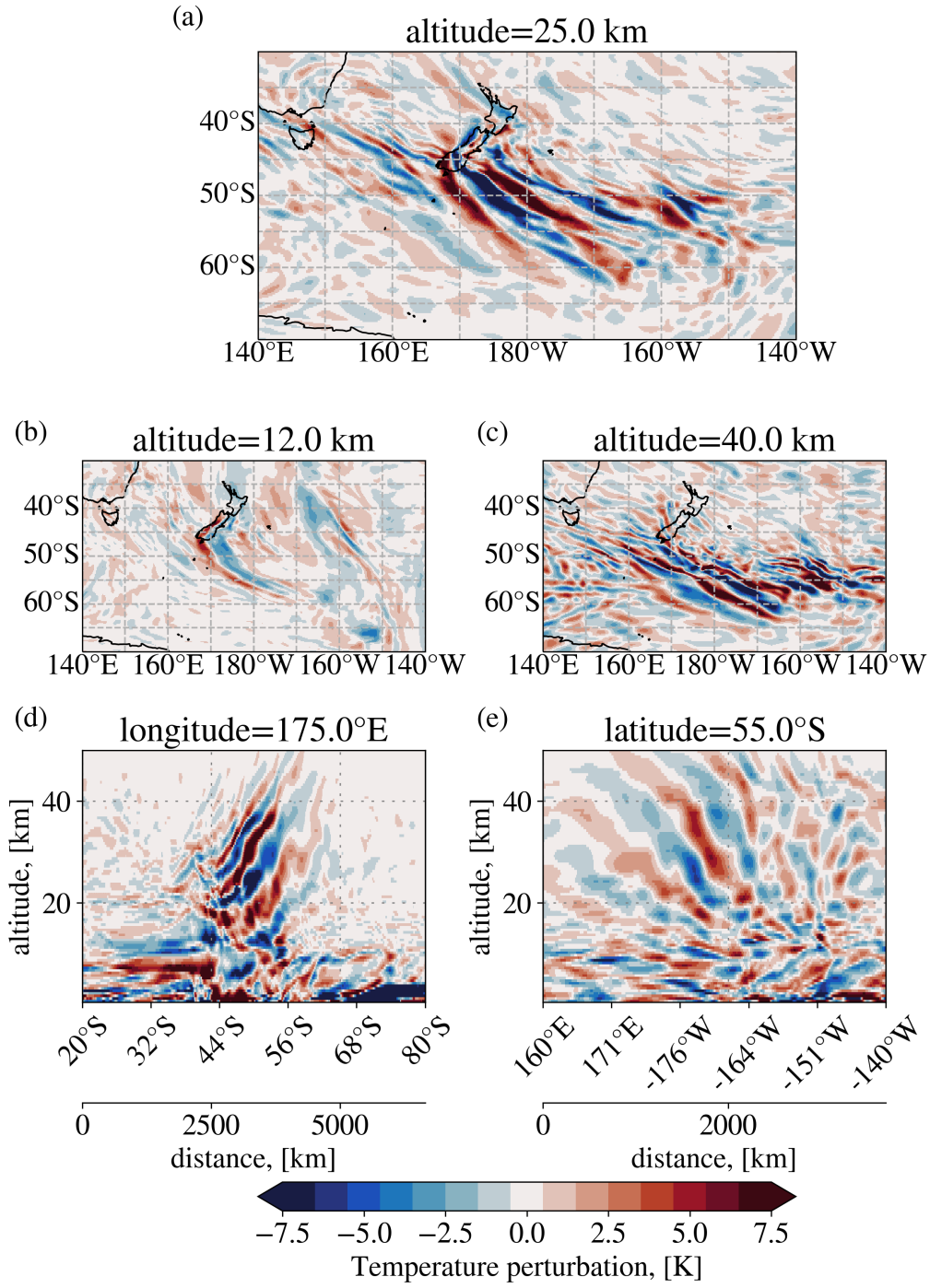

Figure 6.1: Horizontal (a-c) and vertical (d,e) cross sections of temperature perturbations found in the ECMWF-IFS temperature field on 1 August 2014, 12:00 UTC. The temperature perturbations in the vertical cross sections are scaled with a factor of $\exp\left(\frac{-(z-z_0)}{2H}\right)$,$z_0$ =25 km, assuming a scale height of H =7 km, to highlight the vertical phase line structure.

Ehard et al. (2017) for Lauder. The pattern of north-south orientation of the phase fronts is also visible downstream of New Zealand.

To the south, a wave field extends with, generally, north-west to south-east directed phase-fronts to about 63°S and 160°W. The phase front close to the island shows a rather homogeneous wave structure. Close to New Zealand (down to about 53°S) the phase fronts point to the southern part of the island. This is an indication of mountain waves, as mountain waves propagate horizontally along the direction of the horizontal phase fronts and the prolongation of the phase fronts hence points to the source: here to the southern part of the South Island. This detail will be addressed in more detail in Sect. 6.2.5. South of 50°S, the wave field is still connected, but not homogeneous. Instead, there are different horizontal scales and also some variation of phase front direction visible. Also there are some weaker patterns in a diagonal stripe from New Zealand upstream to the east coast of Australia.

At 12 km altitude, the gravity wave field close to New Zealand is dominated by a V-shaped pattern (or rather $<$-shaped pattern) of waves parallel to the mountain ridge along the whole South Island and presumably trailing waves, similar as in the events analyzed by Jiang et al. (2019), starting from the south tip and extending to $\approx$50° S. The latter point to the South Island indicating orographic origin, as discussed in Chap. 2, Sec. 2.3. These wave structures seem to be continued for latitudes 51°S to 58°S, but with a different direction and the prolongation of the phase fronts does not point to the island any longer. In longitudinal direction, the wave pattern is restricted close to the island (170°E to 170°W). At 12 km altitude, it is not trivial to distinguish between gravity wave signals and potential incomplete removal of synoptic-scale structures from weather systems as discussed in Chap. 5. Therefore it is difficult to interpret structures such as the one seen at 60°S and 160°W and 45°S and 160°W.

At 40 km altitude (Fig. 6.1c), the wave field has separated from the island. Some waves are also found upstream of New Zealand and the gravity wave field reaches downstream to 150°W, thus spanning more than 70°of longitude in total. The phase fronts are now oriented more strongly west-east, indicating a further refraction of the wave vector to

increasingly southward direction.

At 25 km, the most prominent horizontal wavelengths in the temperature residual fields appear to range between ≈300 km (e.g. seen around 55 °S between 170°E and 180°E at 12 km, or south of 50°S between 160°W and 150°W at 40 km) and more than 1 000 km (cf. 45°S to 50°S between 170°W and 180°W at 12 km, 55°S to 60°S between 170°E and 170°W at 25 km).

The amplitudes of the temperature perturbations are increasing with altitude. Maximum values range between approximately 7 K at 12 km and approximately 15 K at 40 km. Increasing amplitudes are expected from gravity wave theory, if wave action is conserved (see Chap. 2, Eq. 2.23) because the atmosphere has lower density at higher altitudes.

The temperature perturbations of the vertical cross sections in Figures 6.1d and 6.1e are scaled with a non-dimensional factor of $\exp\left(-\frac{z-z_0}{2H}\right)$, where z is the altitude, z_0 the reference altitude of 25 km and H a scale height estimate of 7 km. The scaling compensates for the density differences in altitude and hence emphasizes the wave front structure. The two vertical sections cut through the center of the wave field: panel 6.1d gives a north-south section at 175°E, and panel 6.1e shows a west-east section at 55°S. The phase lines here are slanted to the west with altitude. This indicates waves propagating against the dominating eastward wind in this area. In the lower to mid stratosphere (between 20 and 40 km), the phase lines get steeper at higher altitudes, consistent with increasing wind velocity; above 40 km the phases are flattening again. Overall the vertical wavelengths range from about 5 km (cf. 45°S, between 160°E and 164°E at 35 km or around 165°W between 20 and 25 km) to about 20 km (cf. 55°S, around 170°W above 25 km).

6.1.2 S3D results

The small-volume, few-wave decomposition method S3D, as introduced in Chap. 4, is applied here on a snapshot of ECMWF-IFS operational analysis temperatures. Besides the fitting method for temperature amplitudes and wave vector, Sect. 4.1 also introduces a number of inferred wave parameters that help in the interpretation of properties of the

wave structure including horizontal and vertical wavelengths, λ_h and λ_z, ground-based wave period, $\hat{\tau}$, the wave propagation direction, ϕ and gravity wave momentum flux.

Sensitivity testing in previous studies (Lehmann et al., 2012; Preusse et al., 2012) indicates best performance of the S3D method, if the cube size is in the middle of the range of expected wavelengths. Furthermore, the longest expected horizontal wavelengths should not exceed three times the horizontal cube size. In this study, the extent of the fitting cube therefore was chosen to be 35 grid points (7°) in the zonal and 21 grid points (4.2°) in the meridional direction. This correspond to about 450 km$\times$450 km horizontal extent at 55°S fitting to the 300 to 1000 km horizontal wavelengths identified in the temperature residuals above (cf. Fig. 6.1). From the temperature residuals, gravity wave vertical wavelengths are expected to range between 5 and 20 km. Therefore, a vertical cube size of 10.5 km (21 grid points) was chosen for the fit.

Figure 6.2 shows horizontal maps of wave parameters obtained for the strongest sinusoidal wave component resulting from the S3D method in the investigated fitting volumes. Inspecting the temperature amplitudes (Figure 6.2a), there are three local maxima of wave amplitudes in the fits: one in the lee closely southeast of New Zealand's South Island ((165°E,45°S) to (180°,55°S)), one further south-east of this first maximum ((175°W, 57°S) to (165°W, 62°S)) and one far to the east from the first one ((160°W, 50°S) to (150°W, 55°S)). These are marked by ellipses in Fig. 6.2 and, for simplicity, the maxima will be referred to in the following as **I** (short for "Island"), **S** (short for "South") and **E**(short for "East") amplitude maximum, respectively. These maxima in temperature amplitude also show areas of maximum GWMF (see Figure 6.2b). GWMF depends both on the squared temperature amplitude and the ratio of horizontal to vertical wavelengths. The momentum flux is a key quantity to determine the potential of the wave for accelerating the general flow by interaction through breaking or dissipation.

Horizontal wavelength values (Figure 6.2c) increase from the northeast to the southwest between approximately 200 km and 1 000 km. The shortest horizontal wavelengths are found in the area of the **I** maximum and the longest around 60°S located at the **E** amplitude maximum. Vertical wavelengths (Figure 6.2d) increase from north to south

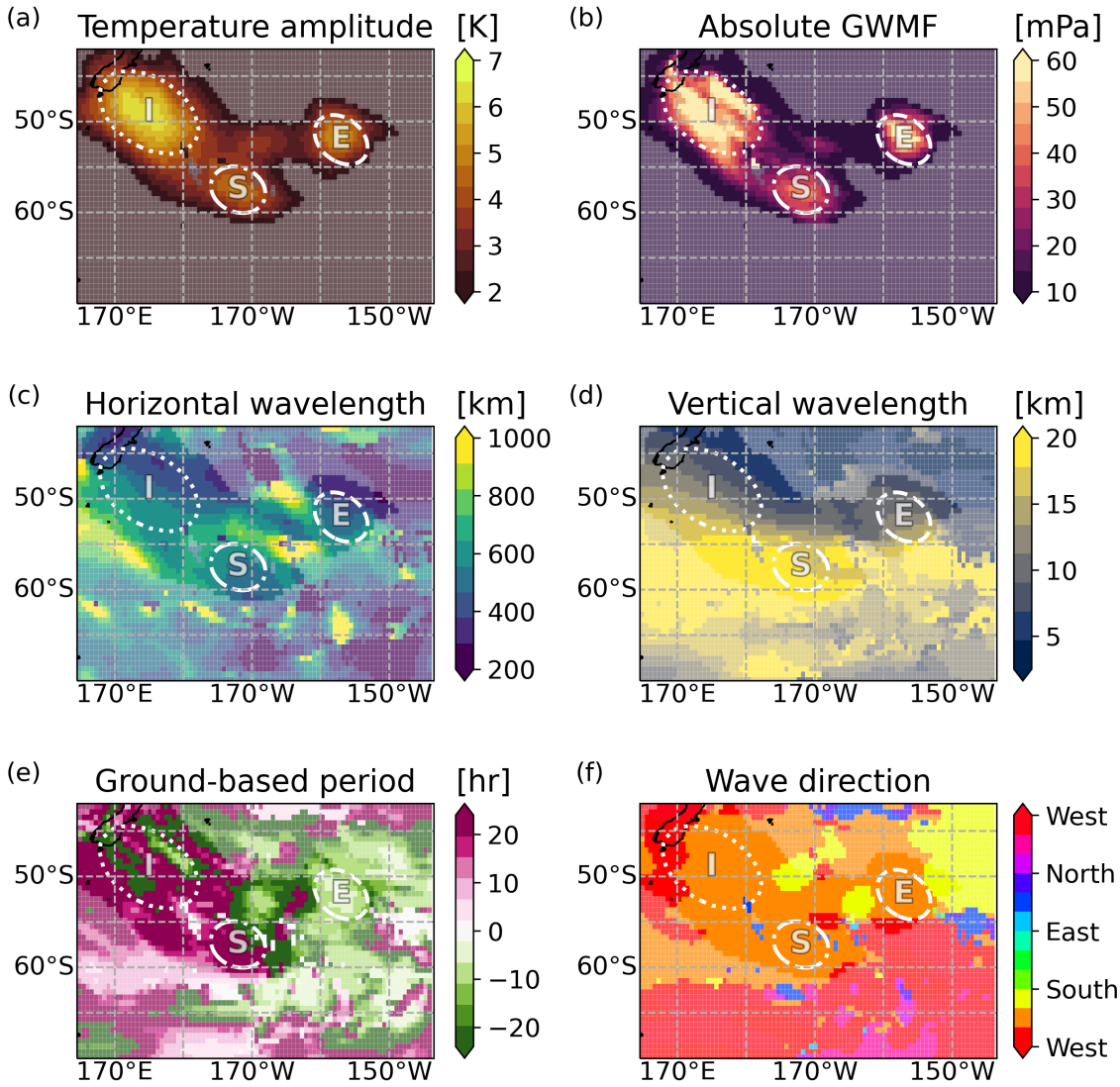

Figure 6.2: Horizontal maps of gravity wave parameters calculated by sinusoidal fits from 35×21×21 grid point cubes on ECMWF-IFS temperature perturbations of 1 August 2014, 12:00 UTC, centered around 25 km altitude. The panels show different gravity wave parameters: (a) Temperature amplitudes, (b) GWMF, (c) horizontal and (d) vertical wavelengths, (e) ground-based period and (f) wave propagation direction. The letters in panel (a) refer to the locations of the different amplitude maxima — **I**="Island", **S**="South" and **E**="East" - as described in Sect. 6.1.2. Areas with a temperature amplitude below 2 K are overlayed with a milky shading to indicate less significant wave events.

ranging between about 5 km for region of the **I** amplitude maximum and 20 km at the **S** amplitude maximum. This is consistent with the fact that the wind maximum of the stratospheric polar vortex is around 60°S and refracts the waves there to longer vertical

wavelengths. In general, the vertical wavelengths are 1 to 2 orders of magnitude smaller than the corresponding horizontal wavelengths.

The ground-based period, τ_{gb}, shown in Figure 6.2e is the period of one full oscillation as observed from the ground. The quantity relates to the ground-based wave frequency ω_{gb} by $\tau_{gb} = \frac{2\pi}{\omega_{gb}}$. The intrinsic frequency $\hat{\omega}$ is calculated as a positive number per definition, but due to the Doppler shift, the ground-based frequency ω_{gb} and hence also the period τ_{gb} may take positive or negative sign. Positive values show advection of the gravity wave phase lines to the east and, analogously, negative values show advection to the West. Most of the wave structure has positive wave periods (in particular in the **I** and **S** amplitude maxima) corresponding to periods of approximately 20 h. These relatively long, ground-based periods indicate almost stationary gravity waves consistent with mountain waves or other low ground-based phase speed sources. Negative ground-based periods are only found east of 160°W. The **E** amplitude maximum has negative τ_{gb} values that are smaller in magnitude than the positive values of the other two maxima and indicates waves with phase fronts moving eastward with respect to the ground.

The direction of the wave vector shown in Figure 6.2f represents also the intrinsic propagation direction and is perpendicular to the phase fronts as seen in the temperature residuals (Figure 6.1). Wave directions in the regions of the maxima (**I**, **S** and **E**) exhibit wave directions pointing west-southwest (≈210° counter-clockwise with 0° pointing to the east) to south-southwest (≈240°).

In summary, the three wave amplitude maxima (**I**, **S** and **E**) have each specific characteristics. The **I** amplitude maximum is characterized by gravity waves with relatively short horizontal and vertical wavelengths, a wave direction pointing to west-southwest, and an intermediate, positive ground-based period. The **S** amplitude maximum is characterized by waves with longer horizontal and especially long vertical wavelengths, wave direction pointing further to the south than for the other cases and very long wave periods. The **E** amplitude maximum is characterized by waves with also relatively short horizontal and vertical wavelengths, wave direction pointing to the southwest and a negative wave period.

For the backward ray-tracing described in the next section, a focus is set to the larger amplitude waves ($\hat{T} > 2$ K) for several reasons: As GWMF is proportional to the square of the gravity wave amplitude, these waves carry most of the momentum flux; the influence of imperfections in the background removal is less important for higher amplitude waves. In addition, gravity wave with amplitudes above a general background level can be expected to have a clear source attribution and, hence, can be well described by a single monochromatic wave, which allows for backward ray-tracing (Preusse et al., 2014; Krisch et al., 2017; Perret et al., 2020). All waves selected in this manner exhibit vertical wavelengths smaller than 2.5 times the vertical fitting-cube extent and horizontal wavelengths smaller than 3 times the horizontal fitting-cube extent.

6.2 Backward ray-tracing

In this section, gravity waves characterised before are traced backwards in time and space using the GROGRAT ray-tracer (see Section 4.2). The altitude of 25 km was chosen as launch altitude because this is where AIRS observations in the study of Ehard et al. (2017) showed structures inconsistent with their theory. In general, GROGRAT rays may be terminated while tracing backwards because of three different reasons: (1) the rays may reach the ground, (2) the rays may approach a critical level from above and, hence, stall vertically (i.e. the vertical group velocity falls below a specified threshold), or, (3) the wave amplitude may vanish because of saturation. For the latter two criteria, the wave could exist at the ray-termination altitude only with insignificant amplitude which would not be compatible with large observed amplitudes at launch. The real source therefore must be located along the ray-path, but for (2) and (3) above the ray-termination altitude (Preusse et al., 2014).

6.2.1 Categorisation of the backtraced rays

The analysis grid for this study is built from overlapping analysis cubes every 0.6° in zonal and meridional direction. This yields more than 2 000 wave characterizations in

the considered region. The analysis is limited to rays with a launch amplitude of more than 2 K. This leaves 1 280 rays covering the strongest parts of the structure, including the regions of the three temperature amplitude maxima discussed in Sect. 6.1.2 (cf. the regions marked by **I**, **S** and **E** in Fig. 6.2). The ray launch and termination points are shown in Figure 6.3 also featuring the areas of temperature amplitude maxima **I**, **S** and **E** in the launch point plots.

For a better overview, the rays are categorised according to indications of different likely source processes and are shown accordingly in the three rows of Figure 6.3.

Two criteria were applied to select rays for categorisation: First, the rays are screened along the ray path for a pass-by close to mountain ridges. If there was an elevation that is higher than 500 m detected in a box of 2° distance in longitude-latitude extent centered around the ray and less than 1 km below the closest ray location, the ray was stopped there and assigned to the first category. In the following, this category will be referred to as "mountain" rays. "Mountain" rays do not necessarily represent waves that are classically generated by flow over a mountain ridge. Also stagnation flow in front of a mountain range and increased convection from corresponding cloud formation, for instance, can trigger gravity waves (Galewsky, 2008; Houze, 2012). However, such processes are still closely related to the presence of mountain ridges, which is the reason why also more distant ray terminations are assigned to the "mountain" ray category. The characteristics of these waves and how they relate to classical mountain waves will be a subject in Sect. 6.2.4. Second, all rays that terminate above 5 km altitude are collected in the "high-terminated" ray category. When rays approach a critical level from above the vertical group velocity approaches zero. This vertical stalling is implemented in GROGRAT, such that the ray is terminated when the vertical group velocity falls below a defined threshold. For this study, the threshold is defined as 0.01 times the launch group velocity. In this case, efficient energy transport from a lower level is not possible, hence, the source must be located above. An altitude of 5 km was chosen as a threshold here to restrict the options for possible sources of the represented wave: In the analysis area, an orographic wave cannot originate from above 5 km altitude, since the orography in New Zealand and

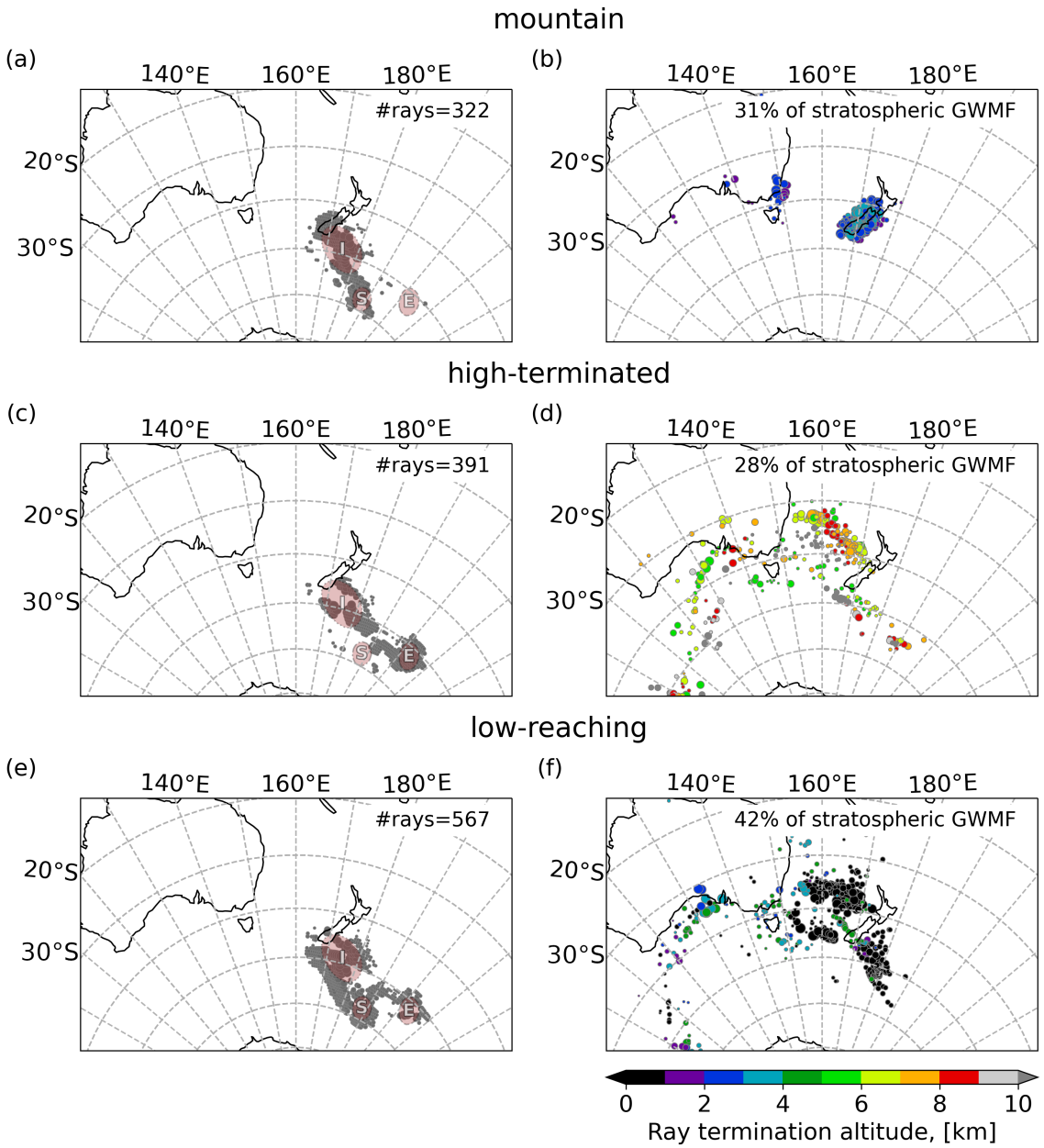

Figure 6.3: Ray-tracing results for (upper row) "mountain", (middle row) "low-reaching" and (lower row) "high-terminated" ray categories. Right column: Location of the ray-termination for different source categories. The color of the markers shows the lowest ray altitude. Upper left corner: Percentage of stratospheric GWMF. Left column: Location of the ray launch points at 25 km altitude. Upper right corner: Total number of rays in that category

Australia does not exceed 4 km[1]. Furthermore, frontogenesis is usually diagnosed at

[1]The highest peak of New Zealand and Australia is the Aoraki/Mount Cook with 3 724 m

the 850 hPa level, which is located also well below 5 km altitude. This leaves jet-related generation and deep convection as the most likely candidates for sources to the "high-terminated" rays. Another possible option might be secondary wave generation, which is however not very likely in the lower stratosphere. In the literature, there are no studies of secondary gravity wave generation for altitudes below 40 km and to be relevant in our case the generation would have to take place well below 25 km.

As a third category, the remaining rays are collected, which will be referred to as "low-reaching" rays. The number of likely source processes for this category is broader, since the generation can, in principle, take place anywhere along the ray.

The three ray categories do not necessarily coincide with the three regions of temperature amplitude maxima (**I**, **S** and **E**) discussed in Sect. 6.1.2. However, the local characteristics of the wave parameters, such as wave frequencies, are associated with different source processes in Sect. 6.2.3.

Figure 6.3 shows in the left column the ray launch points in the stratosphere and in the right column the ray termination points respectively for the "mountain" (upper row of 6.3), "high-terminated" ray category (middle row of 6.3) and "low-reaching" (lower row of 6.3). The ray launch point marks the location of the relevant cube centres from the S3D analysis discussed in Sect. 6.1.2. In the upper right corner of each ray-launch-point panel (left column) the total number of rays in this category are shown. The grey dots marking the launch locations are scaled with the launch GWMF inferred for the individual ray to highlight the locations that are most relevant for the momentum budget. The ray-termination point refers to the location of the lowermost altitude an individual ray reached in the propagation. In the panels showing the ray-termination points (right column), the percentage of the total GWMF at 25 km attributed to this category is given instead. The coloured dots mark the location of the ray-termination points and the colour code shows the altitude of ray termination. Furthermore, the size of the dots is scaled with the inferred GWMF at the launch location of the ray analogous to the dots of the corresponding launch points on the left. This gives a visual aid which ray excitation areas are most important for the energy and momentum budget in the stratosphere.

Most of the rays cluster locally both at launch and termination altitudes. At termination altitudes, the “mountain” rays originate mainly from around the Southern Alps on the South Island of New Zealand. Some are accumulating in the strait between the North Island and South Island. A few of the rays also trace back to Tasmania and mainland Australia, however, the associated momentum flux is small. In total, “mountain” rays in this case correspond to about one third (31%) of the sum of stratospheric GWMF calculated at the launch level of 25 km altitude. “Mountain” rays, however, make for only about a quarter, 322 of the total of 1280 rays, in number, which shows that they carry above-average GWMF. At launch altitude the locations for “mountain” rays (Figure 6.3 a) cluster in three areas:

1. around the South Island of New Zealand,

   → This is over the Southern Alps extending into the upwind-side of the mountain range.

2. in a streak extending from the tip of the island eastward for about 10° over the ocean, and

   → This coincides with large parts of the **I** amplitude maximum discussed in Sect. 6.1.2.

3. around 175°W between 55°S and 60°S.

   → This region coincides partly with the **S** amplitude maximum and indicates that “mountain” rays contribute to this structure.

The termination points of “high-terminated” rays cluster along an almost straight line above the Tasman Sea aligned from the northwest to southeast, approximately between (160°E, 30°S) to (170°E, 38°S). Most rays terminate there between 6 km and 9 km altitude. A second cluster is aligned south of New Zealand along a line from (160°E, 48°S) to (175°E, 50°S). Furthermore, there are a few small clusters at (145°E, 46°S), at (175°E, 48°S) and at (172°W, 52°S). The group at 100°E, south of 50°S corresponds to rays that leave the considered horizontal domain. “High-terminated” rays are associated with less

than a third of the stratospheric momentum flux (28%). The launch areas cluster mainly on the **I** amplitude maximum and the **E** amplitude maximum.

Many of the "low-reaching" rays are launched in the western part of the gravity wave field directly south of New Zealand, i.e. as part of the **I** amplitude maximum, and from **S** amplitude maximum. The majority of those waves terminates below the core of the tropospheric jet upwind of New Zealand. In particular for the **S** amplitude maximum, the waves originate at a source very close-by and propagate close-to vertically. "Low-reaching" rays are the largest class, both in GWMF (42%) and total number of rays (567).

In general, it is evident for almost all rays that the termination areas are far further north than the main GWMF patterns observed in the stratosphere. This detail will be discussed in more detail in Sect. 6.2.2.

6.2.2 Dependency of lateral propagation on wind and wave direction

In order to quantify the lateral propagation of the gravity waves, Figure 6.4 shows the total distance and the zonal and meridional shift separately for the three ray-termination categories. The left column shows the total distance the waves propagate between the ray termination point in the troposphere and the ray launch point at 25 km altitude. As already indicated by Ehard et al. (2017), some of the mountain waves propagate almost vertically in the troposphere and most of the stratosphere. Consequently, the "mountain" ray category (Figure 6.4a) is the only one which shows a major contribution also in the bin of shortest propagating distance which collects distances from zero to 500 km. In general, "mountain" rays travel short distances and hardly any are propagating further than 2 000 km away from the launch region. This is consistent with the modeling study of Jiang et al. (2019), who find for another gravity wave event of the DEEPWAVE campaign trailing waves from New Zealand to propagate onto the open ocean in the stratosphere. These trailing waves travel only about 10° southeastward of the island and the main part of the wave field still remains over the island (Jiang et al., 2019).

"Low-reaching" (Figure 6.4 c) and "high-terminated" (Figure 6.4 e) rays seem to fall into two groups: one with propagation distances less than 2 000 km and the second with

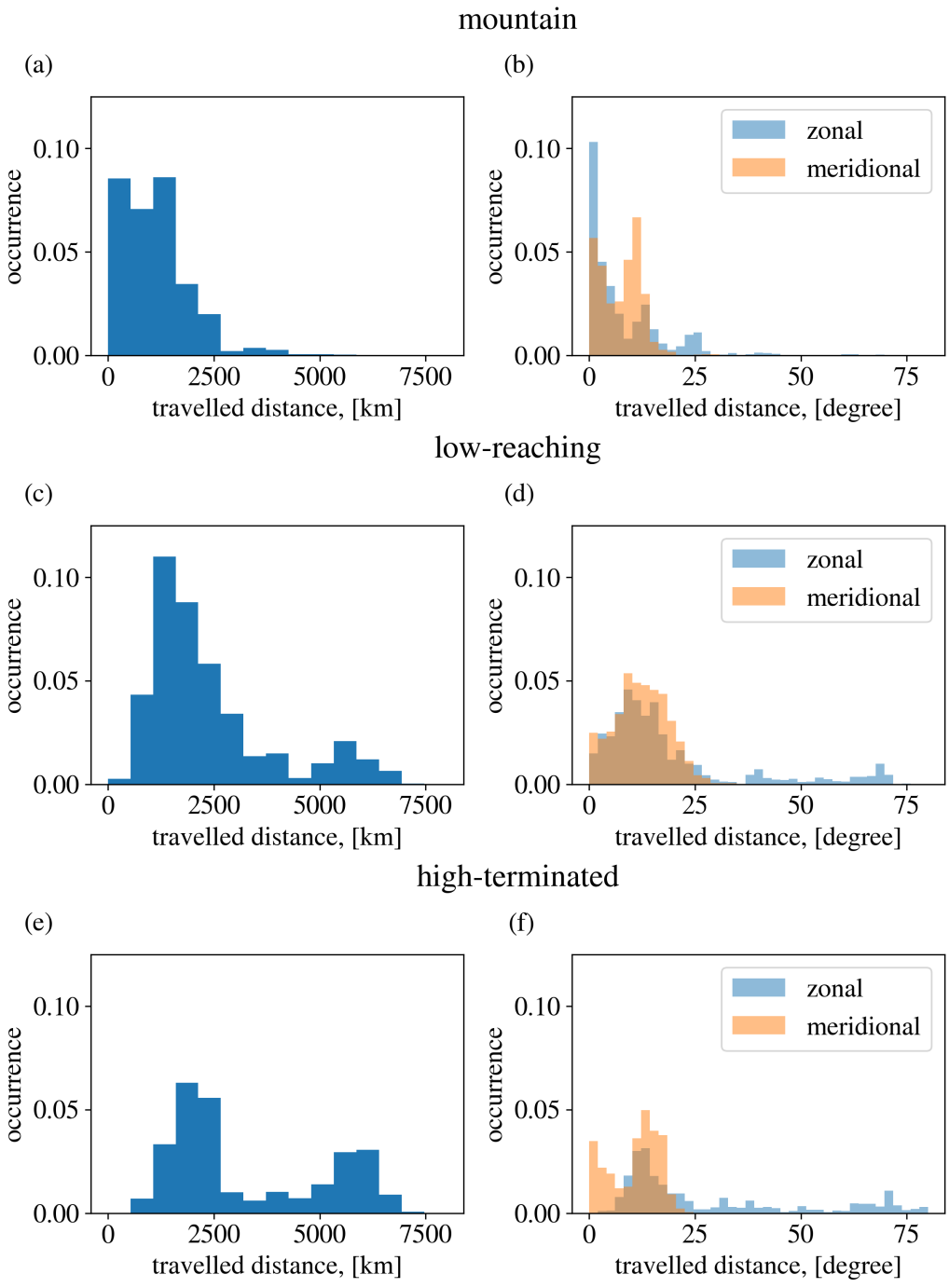

Figure 6.4: Occurrence frequency of distance between launch point (25 km altitude) and termination point. The upper row shows geometric distances along a great circle; the lower row shows distances in zonal and meridional direction. Distances were weighted by relative GWMF at ray launch, hence rays associated with more momentum flux in the stratosphere are emphasized.

distances around 6 000 km. The relative importance between these two groups is shifted. For the “high-terminated” rays, longer distances occur more often while, for the “low-reaching” rays, the shorter distances seems to be more frequent. The result is consistent in a way, that “high-terminated” rays are closely connected and shaped by the critical level they approach, which usually means that they have lower intrinsic phase speeds and are more prone to lateral propagation. Furthermore, a large amount of the “low-reaching” rays travels about 500 km to 1 000 km distances, which is consistent with the overlap of launch and termination areas for the **S** amplitude maximum.

The right column of Figure 6.4 shows the zonal and meridional propagation distance. These propagation distances are measured in degree and, hence, the identical values in meridional distance compared to zonal distance indicate almost double the total distance in kilometer. For all three ray categories substantial southward propagation is evident. Notably, the largest meridional propagation is observed for the “low-reaching” rays despite the fact that “high-terminated” rays are propagating the larger total distance. Obviously, the “high-terminated” rays are drifting downstream with the wind while the “low-reaching” rays have a tendency for southward propagation.

It is one aim of this study to identify the altitude at which lateral propagation takes place. This question is further investigated here by analysing latitude-altitude propagation paths shown in Figure 6.5. For all three termination categories, the gravity wave origin is mainly associated with the tropospheric wind maxima between 30 °S and 50 °S.

Gravity waves in the “mountain” ray category fall into two branches, a compact one propagating almost vertically and a second, spreading branch which shows southward propagation below 20 km altitude. The main paths are flatter below 15 km altitude and steepen above. A similar behaviour was also shown in Krisch et al. (2017) for a mountain wave packet from Iceland in the northern mid to high latitudes.

“Low-reaching” rays show the furthest meridional propagation (cf. also Figure 6.4). A common pathway runs from about 35 °S close to the ground to 55 °S (or further south) at 15 km altitude. Above, also these rays steepen and proceed to propagate more vertically once they enter the stratospheric jet.

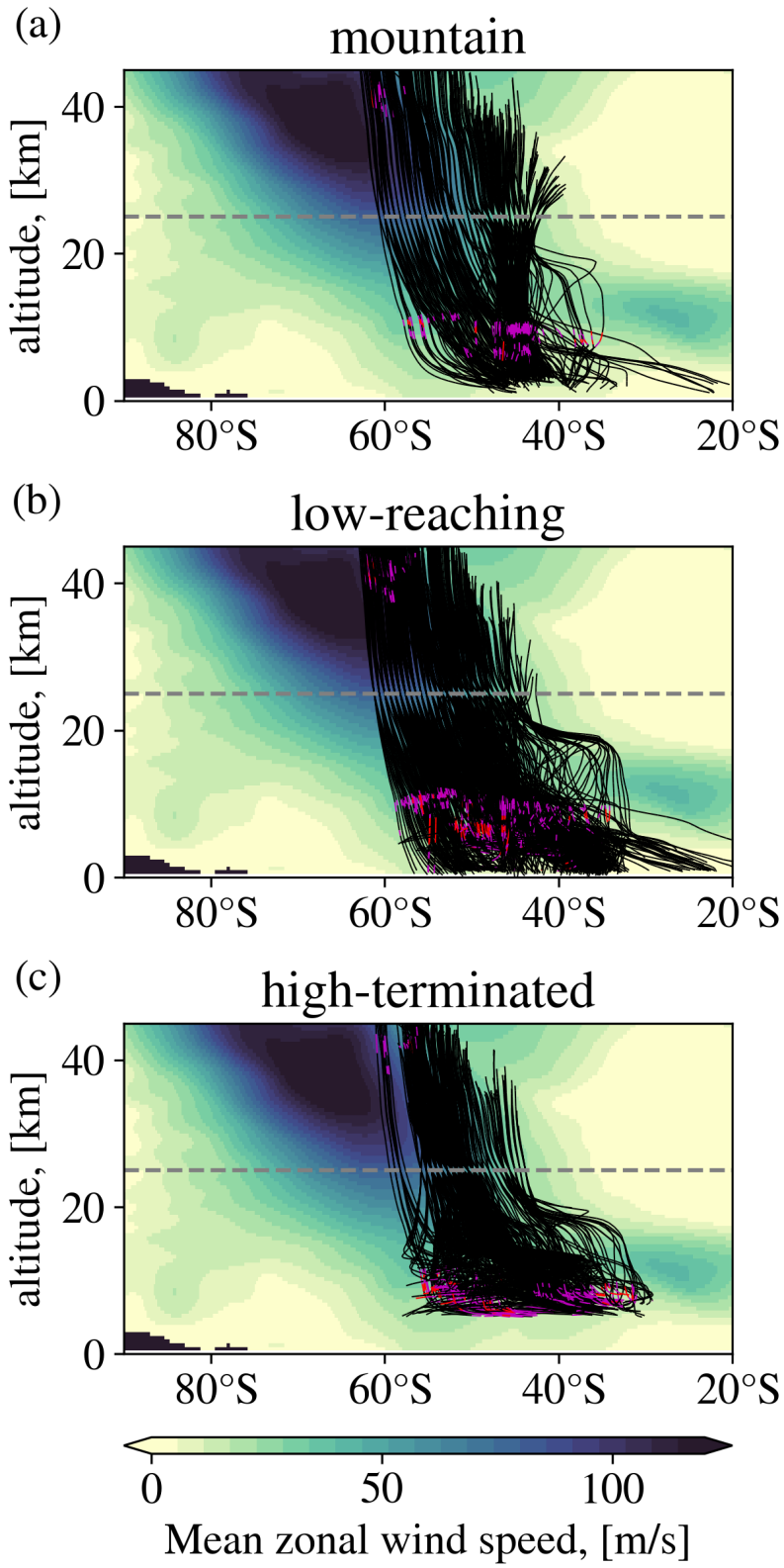

Figure 6.5: Latitude-altitude location of backward ray traces. The magenta and red colored sections of the rays show where the vertical WKB criterion is violated, i.e., where rays would be partly dissipated propagating upwards. The color code in the background shows the mean zonal background wind on 1 August 2014, 12:00 UTC.

Lastly, “high-terminated” rays tend to experience a very flat propagation at lower altitudes almost propagating only horizontally for a time. Then, these waves show very low vertical group velocities indicating a state very close to “vertical stalling”. This points to waves with small vertical wavelengths already in the lower stratosphere (around 15 km altitude), which is often associated with strong shears. This might also be an indication that the gravity wave source is actually located at the shear regions rather than the final ray termination point.

It should be noted that only those waves which enter the stratosphere are part of this study, because the ray tracing is performed from 25 km altitude backwards. In addition to these waves, there could be an abundance of gravity waves which propagate upward from mid-latitude sources, but reach a critical level in the tropospheric subtropical jet (20 °S to 40 °S) above 15 km altitude. These waves then would not contribute to the wave fields in the stratosphere. If waves were dominant at 15 km altitude that remain very close to their sources and have little relevance for the stratosphere, that would explain the apparent contradiction between the modelling study of Holt et al. (2017) and the superpressure balloon observations of Hertzog et al. (2008) and Jewtoukoff et al. (2015). However, testing this theory would require a modeling study upwards from relevant sources which is beyond the scope of this study.

6.2.3 The relation of ground-based phase speeds and gravity wave sources

The ground-based phase speed is closely related to the source process, but also highly relevant for the propagation path of a gravity wave. In theory, gravity waves induced by flow over orography, i.e. mountain waves, are expected to have zero ground-based frequency in a constant incident flow on the mountain ridge. Changing wind velocities as well as possible interactions with clouds or turbulence (Worthington, 1999) are expected to induce slow non-zero ground-based phase speeds.

Figure 6.6 shows the occurrence distributions of the ground-based phase speeds among the three ray categories at launch and termination altitudes. Indeed, the “mountain” ray category shows the most compact of all three distributions centered around zero

and mostly inside $\pm 10\,\mathrm{ms}^{-1}$.

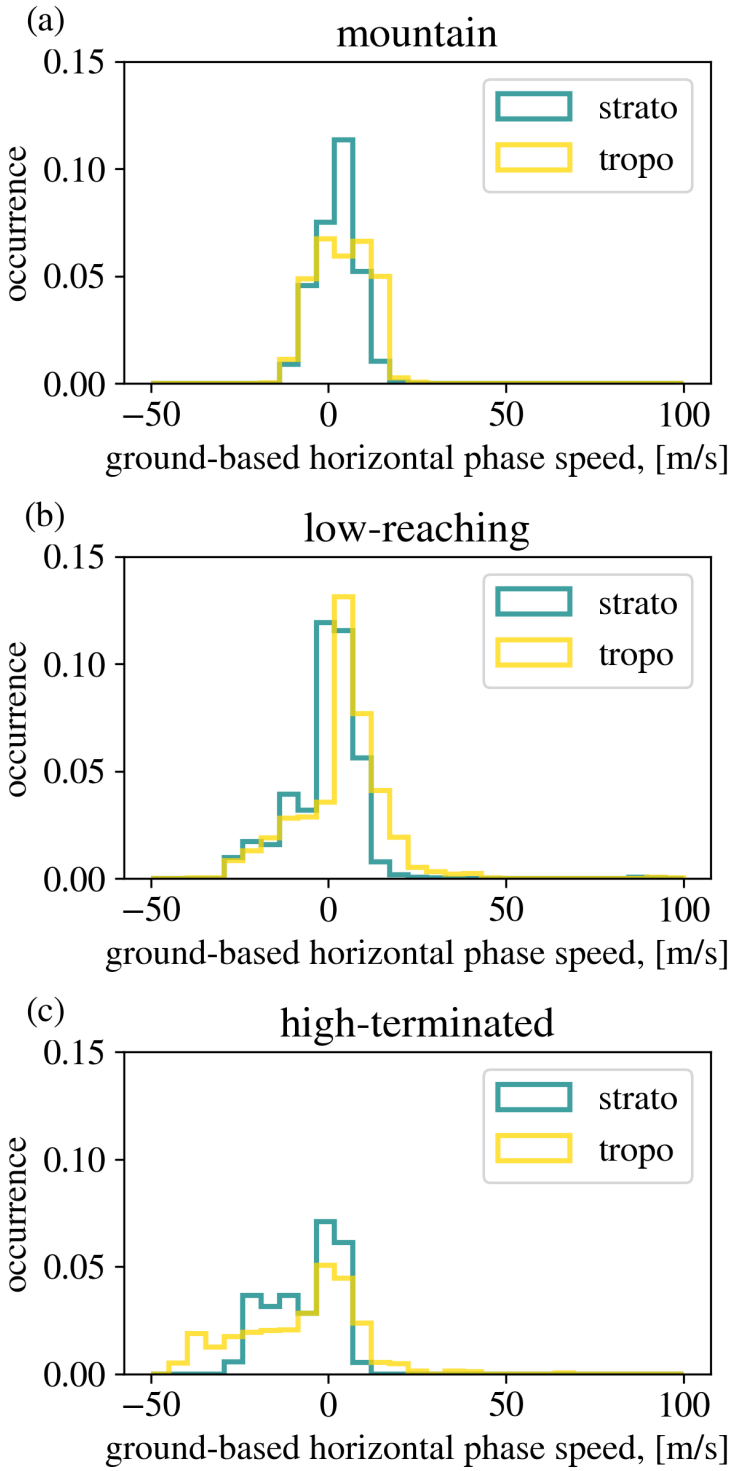

Figure 6.6: Phase speed of gravity waves relative to the ground (blue) at observation altitude (25 km) and (yellow) at ray-termination for the three ray-termination classes, respectively.

Waves with low ground-based phase speeds have intrinsic phase-speeds closely related to the wind velocity and the relative orientation between wind and wave vector. If they are strictly opposite, wind and intrinsic phase speed cancel each other and keep the wave above the source. At an angle, the component of the phase velocity compensating the wind is smaller: the wave drifts with the wind, and simultaneously, there is a component perpendicular to the wind (in this case southward), which lets the wave propagate meridionally. In the case of mountain waves, the ground-based propagation takes place along the horizontal phase fronts of the waves.

The ground-based phase speed of the "high-terminated" rays is mostly negative with respect to the wave vector, i.e. drift and active propagation are in the same direction. This makes the "high-terminated" rays propagate very far laterally (cf. Sect. 6.2.2). The ground-based phase speeds reach high negative values especially at termination altitudes, which further substantiates this point.

The distributions of ground-based phase speeds for the "low-reaching" rays shows an intermediate between "mountain" and "high-terminated" rays. The high number of rays with low ground-based phase speeds correspond well with the close locations of launch and termination points around the **I** and **S** amplitude maxima.

6.2.4 Angle of the waves relative to the ground and to the wind

The orientation of the wave vector determines how far a gravity wave can propagate laterally. This is true especially for waves with low phase speeds because the drift with the wind is particularly effective for waves with a low vertical group velocity that stay at the same altitude level for a longer period of time. In Figure 6.7 this is highlighted further by showing the propagation distance for the rays from termination to launch point on the vertical axis and the relative propagation direction[2] on the horizontal axis. Values are given for the altitude range between 6 and 18 km, which was chosen to investigate the altitudes where the rays seem to undergo the majority of the meridional shift (see the gradient in the ray paths in Fig. 6.5).

[2] Here, the relative propagation direction refers to the angle between wave direction and wind direction.

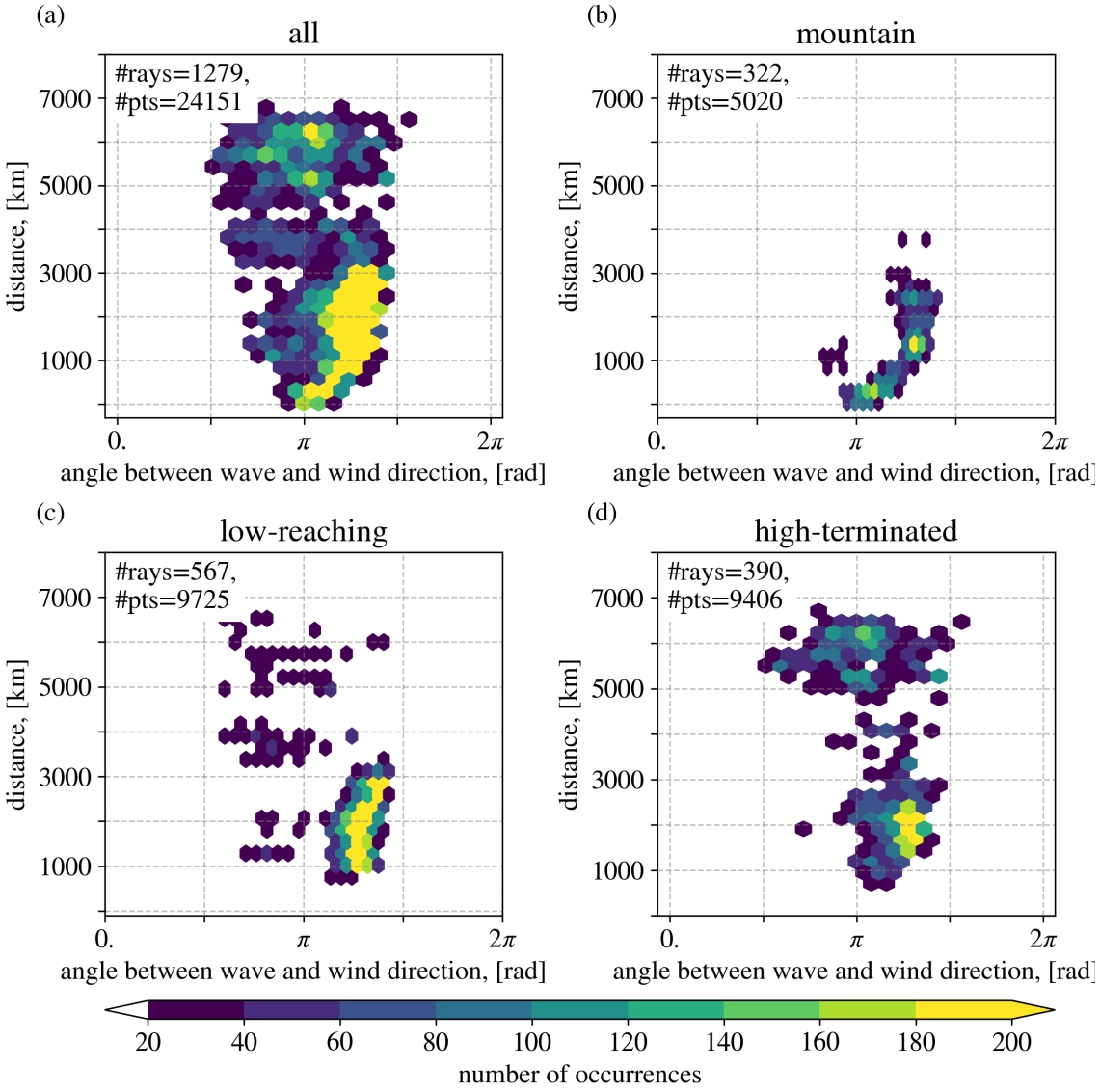

Figure 6.7: Relation of wave direction relative to the background wind direction versus propagation distance from lowest ray level to 25 km altitude in bins of ray instances. The colour map shows the number of instances in each bin.

In general, almost all directions between 90 °and 270 °seem to exist. However, the shorter the travelling distances, the closer is the wave to staying opposite to the wind. As expected, for “mountain” rays there is an almost linear dependency between propagation distance and angle: rays with 180 °relative propagation distance (i.e. wind and wave directed strictly opposite) are remaining over the source while the furthest propagation for “mountain” rays is reached for approximately 225 °(or 45 ° from opposite to the

wind). Waves at steeper angles, i.e. greater than 225 °are rather drifting downstream than propagating southward and are, in addition, easily dissipated.

For the “low-reaching” rays, which possess non-zero ground-based phase speed, the similar relation is visible, but less pronounced. The “high-terminated” rays that are propagating very far (≈6 000 km) are propagating at a variety of different angles. Angles between 90 °and 180 °are of little importance for waves propagating smaller distance and almost absent for “mountain” rays.

The results so far suggest a paramount importance of the relative wave direction for how far a particular wave propagates laterally. In previous studies, horizontal refraction was presented as a major factor for lateral propagation and focusing of gravity waves into the stratospheric jet stream (Sato et al., 2009; Preusse et al., 2009a). The question remains, to what extent refraction is relevant in this ray-tracing study.

In this context, Figure 6.8 shows in the left column the propagation direction relative to the ground, in the middle column the wind direction and in the right column the relative angle between waves and wind as direction in the angular axis. Here 0 ° represents a direction to the east, 90 ° southerly wind and northward propagation and so forth. The radial component represents altitude from 0 to 25 km. The figure furthermore separates the results for three ray categories: “mountain”, “low-reaching”, and “high-terminated” rays in the rows.

For the “mountain” rays (shown in the upper row, panels (a) to (c)), the majority of the waves point to approximately 225° (Figure 6.8a) for all altitudes. This corresponds well with trailing waves as one important process included in the “mountain” ray category discussed repeatedly in the previous sections. The wind turns with altitude (panel b). This turning translates to the relative propagation directions (panel c), since the wave directions are mostly constant with altitude. However, the relative direction always remains smaller than 270°, hence avoiding the directional critical level. There is a secondary, weaker branch of common directions around 150° in the wave directions (panel a) at low altitudes which turns with altitude to 180°. These waves are excited with wave vector orthogonal to the mountain ridge. This branch has relative propagation directions closer to

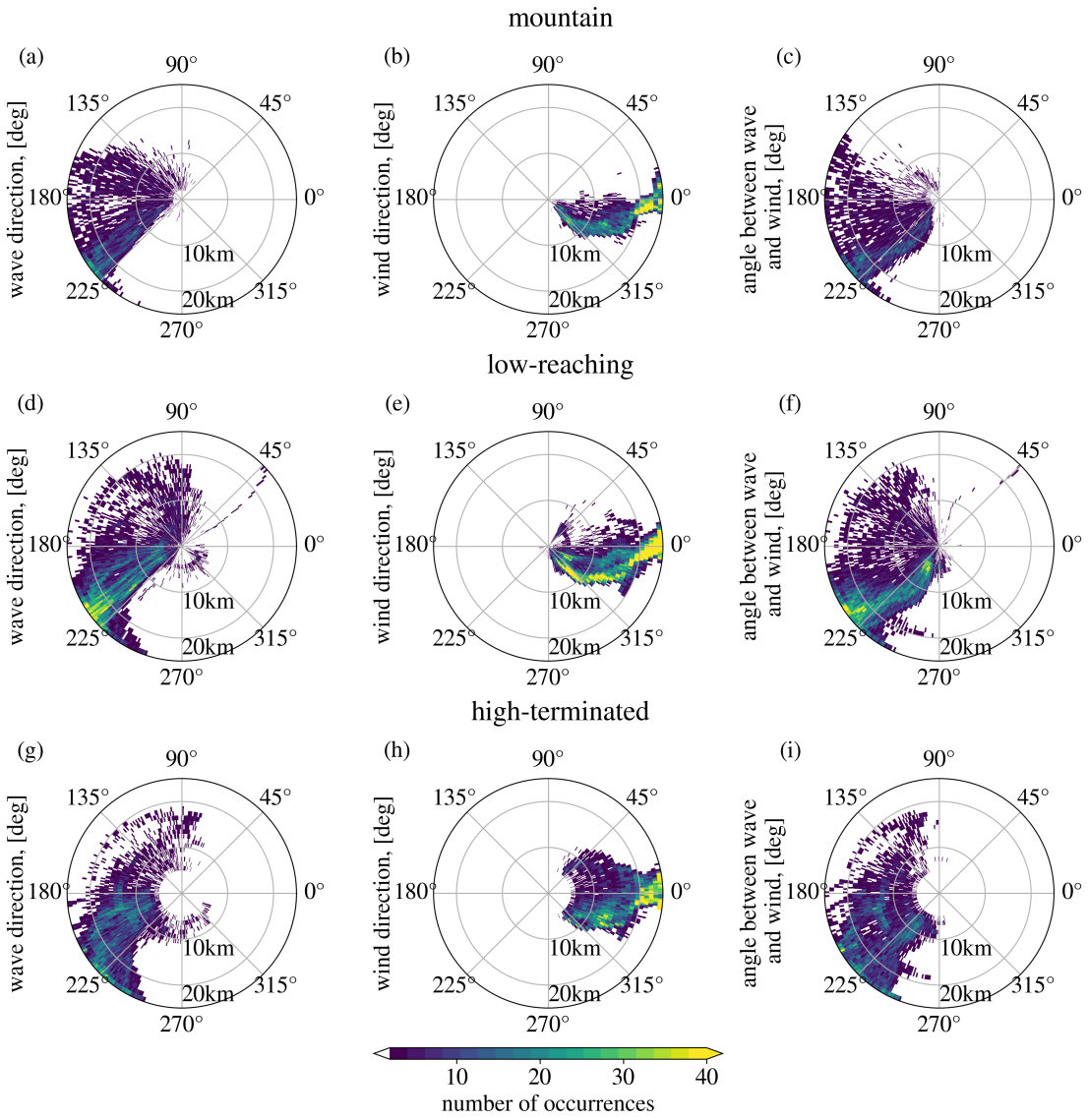

Figure 6.8: Polar maps of wind and wave directions along the GROGRAT rays binned into 0.5 km altitude (radial) and 1 ° boxes. The colour maps shows the number of ray instances in the corresponding box.

180° (panel c) throughout all altitudes, because of the wind direction turning. Therefore, the waves remain mostly stationary to the ground. This relates to the mountain waves discussed by Ehard et al. (2017) where waves are kept stationary over the mountain up to the middle stratosphere and may then shift laterally into the jet. However, as already mentioned, this process is expected to be represented less dominantly in this study because of the selection of waves from the large wave field mainly south of New Zealand.

"Low-reaching" rays (middle row of Figure 6.8) mostly exhibit directions of approximately 225 ° to the ground. Unlike for the "mountain" rays, the "low-reaching" rays do not show a secondary group of mostly stationary waves with 180 ° direction, especially not for high altitudes.

"High-terminated" rays are the only group with a notable fraction of eastward propagating waves (panel g) and for these waves all directions relative to the wind are present (panel i), though there is still a preference for a loosely-opposite orientation to the wind.

6.2.5 Origin areas of non-orographic rays

The position of "low-reaching" and "high-terminated" rays with respect to the jet is shown in Figure 6.9a and b, respectively. The jet is plotted in horizontal wind maps for 18:00 UTC on 31 July 2014, the synoptic time step closest to the time at which most rays, and in particular those closer to New Zealand, are terminated. "Low-reaching" rays are found often several 100 km upstream of New Zealand and closer to the jet core. A second maximum is located at the eastern-most part of the high wind velocities around 180°W, 50°S where the wind velocity strongly decreases. According to their position, they are likely associated with an unstable flow and have ground-based phase speeds of a few 10 ms^{-1}.

"High-terminated" rays originate from the northern border of the jet, a region of strong wind gradients. Their phase fronts are approximately parallel to the wind and seen also in tropospheric vertical winds (cf. Figure 6.10).

High-terminated rays: Indication for jet-exit region

Figure 6.10 shows the relation of local wave properties of selected "high-terminated" rays together with the background atmosphere for selected altitudes. The vertical wind maps show different types of perturbation all over the presented region, but especially between 150 °S and 170 °E. A streak of disturbances with small spatial scales aligns from the Australian east coast (around [150 °E, 35 °S] to [165 °E, 55 °S]). Comparing the location of these disturbances with the horizontal wind speed maxima in Fig. 6.9, it is evident that

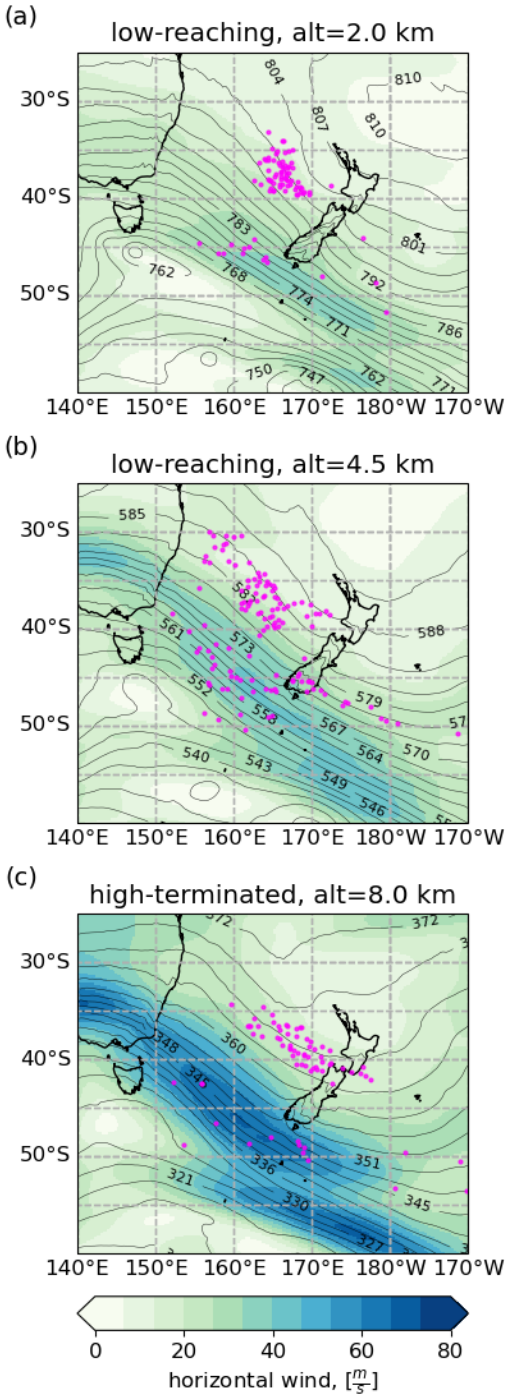

Figure 6.9: Current ray locations on horizontal background wind maps (i.e., large scale part from the scale separation) from ECMWF operational analyses of 31 July 2018, 18:00 UTC signified by the colour code. Contours show the pressure levels with values specified as numbers on the contour.

they are located right in the centre of the subtropical jet.

Vertical wind patterns that point to a jet-exit region can be found in the vertical wind map north of the jet stream (roughly between (155 °E, 35 °S) and (170 °E, 40 °S)) for all presented altitudes.

Most of the waves are found colocated with long horizontal wavelength wave structures of weak amplitudes. Again, for the stratosphere most relevant are not necessarily the strongest waves but these which are able to enter the stratosphere and hence are contained in our study. A detailed discussion of the source processes is however beyond the scope of this study.

6.3 Conclusion

In the present study, a gravity wave field south of New Zealand was analysed that was first presented by Ehard et al. (2017) in AIRS observations supporting their lidar study for the DEEPWAVE campaign. ECMWF operational analysis data of the structure show the same overall wave patterns as seen in the AIRS observations. The advantage of using the ECMWF operational analysis data for this investigation are the regular sampling without gaps and the good vertical resolution compared to AIRS observations. Furthermore, the model snapshots are not limited by observational filter effects (Hoffmann and Alexander, 2009; Krisch et al., 2020).

Table 6.1 collects the identified characteristics of different part for the wave field separated by the three defined regions of high temperature amplitudes and the categories the corresponding rays where sorted into. The overview shows that different wave packets build the complex wave structure under investigation. Furthermore, these characteristics are important for the different behaviours later observed for the rays that are traced backwards.

In the characterised area shown in Fig.6.2, horizontal wavelengths range between approximately 200 km and 1000 km. The high temperature amplitude regions generally show longer horizontal wavelengths starting from roughly 400 km. The wavelengths are shortest for **I** and longer for **S** and **E**. In the region of **I** there is a mixture of different

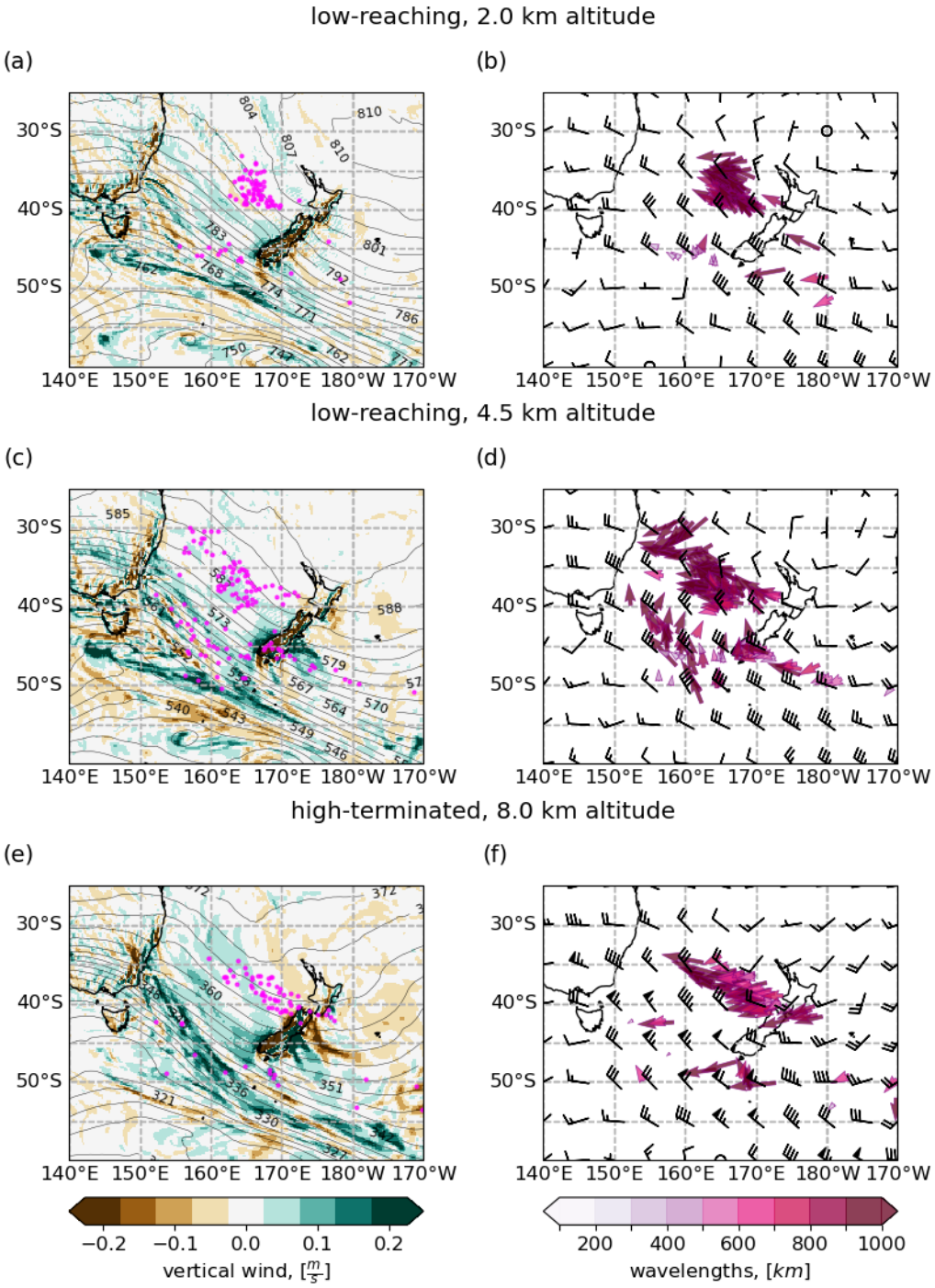

Figure 6.10: In the rows different altitudes with the corresponding ray categories as stated in the titles are shown. On the left: Position of ray-termination points overlayed on vertical wind velocities for 31 July 2014, 18:00 UTC, i.e. 18 h before the 25 km wave patterns analysed. Only ray locations that coincide with altitude and time are shown. On the right: Arrows show the direction where the wave vector is pointing at the ray location. The colour code highlights the different horizontal wavelengths of the shown rays.

	region **I**	region **S**	region **E**
"mountain" rays			
– hor. wavelengths	intermediate (400-600 km)	long (>500 km)	no rays
– gb. phase speeds	slow (0-10 m/s), mostly positive	very slow (0-5 m/s), positive	
– wave directions	west to southwest	west to southwest	
"low-reaching" rays			
– hor. wavelengths	intermediate (400-600 km)	long (>500 km)	intermediate (400-600 km)
– gb. phase speeds	two branches: 1) very slow (0-5 m/s), positive; 2) intermediate (5-15 m/s), negative	two branches: 1) very slow (0-5 m/s), positive; 2) slow (0-10 m/s), negative	fast (15-20 m/s), negative
– wave directions	west to southwest	west to southwest	southwest
"high-terminated" rays			
– hor. wavelengths	intermediate (400-600 km)	no rays	intermediate (400-600 km)
– gb. phase speeds	very slow (0-5 m/s), mostly positive		fast (10-25 m/s), negative
– wave directions	southwest		southwest

Table 6.1: Characteristion of waves in temperature amplitude maximum regions **I**, **S** and **E** with respect to their ray categoryof "mountain", "low-reaching" and "high-terminated" rays. Abbreviations: "hor." = horizontal, "gb." = ground-based.

propagation directions with a general tendency to westward and southwestward propagation, **S** and **E** are dominated by southwestward propagation. The vertical wavelengths are shorter in the north and longer in the south, as is expected from the higher background wind velocity in the stratospheric polar jet. Hence, vertical wavelengths only show differences because the high amplitude regions are located at different latitudes and are therefore not featured in the overview table. Inferred ground-based gravity wave periods are approximately 8 h for **E** and frequently 20 h and longer for **S** and **I**. These long periods indicate a contribution of mountain waves in particular to **I** and **S**.

Comparing the three categories to the three amplitude maxima the "mountain" category is responsible for the entire GWMF directly above New Zealand and for a larger

part of the trailing waves to the south of the South Island. The “low-reaching” category makes a second, large contribution to the tail to the south of New Zealand and forms the temperature amplitude maximum region **S**. Finally, the **E** amplitude maximum is dominated by “high-terminated” rays. The “mountain” category contributes about one-third of the total GWMF in the stratosphere, the “high-terminated” category about one quarter, and the largest part of more than 40 % is provided by the “low-reaching” rays, indicating that non-orographic sources generate an important part to the gravity wave activity in the southern hemispheric polar vortex region.

The slow ground-based horizontal phase speeds of rays from the **I** and **S** region suggest orographic wave sources. Other generation processes like convection, however, are also capable to generate very-low-phase-speed waves. Slow phase speeds still suggest a rather short lateral shift, which fits well to the travelled distances observed in the corresponding ray categories. Rays from the **E** region on the other hand are dominated by faster ground-based horizontal phase speeds, suggesting non-orographic generation. As the ground-based phase speed of the waves is comparably slow, the orientation of the waves is deciding of how far they can propagate to the south. Most efficient for lateral propagation is a southwestward propagation direction of $\sim$225° or $\sim$45° south relative to that direction opposing to the mean wind.

Most of the lateral propagation takes place below 15 km altitude, and almost all below 20 km. Considering the altitude distribution of the propagation direction there is indication for considerable horizontal refraction mainly in the part of “mountain” rays which remain over New Zealand and closely downstream. Otherwise waves have a southwestward propagation direction already at low altitudes.

Gravity waves which may have been excited but meet a critical level on top of the tropospheric jet, and thus do not enter the stratosphere, are not accounted for in this study. This may explain a strong dominance of southwestward wave orientation and it may also explain in part why Holt et al. (2017) see GWMF still close to the sources at 15 km, but Geller et al. (2013) find the GWMF maximum in the polar jet as low as 18 km altitude.

Chapter 7

Summary and outlook

This thesis provides a comprehensive analysis setup for resolved gravity waves in atmospheric fields from Integrated Forecast System of the the European Centre for Medium-Range Weather Forecasts (ECMWF-IFS). A constant increase in resolution during recent years advanced the operational analysis products of ECMWF-IFS up to a point where a large part of the relevant gravity wave scales are represented realistically. The analysis setup includes the extraction, characterisation and propagation behaviour of resolved gravity waves in the ECMWF-IFS operational analysis temperatures.

The challenges to extract gravity waves from different temperature data sets is often underestimated. Large-scale structures like inertial instability signals can be misinterpreted as gravity waves when insufficient background removal techniques are applied. Two spectral filters for removing the background atmosphere from temperature fields to reveal gravity waves are therefore compared thoroughly in application to an artificial inertial instability model, ECMWF reanalysis temperatures and satellite measurements from the SABER instrument. It was shown that horizontal filtering can adequately handle the presence of inertial instabilities.

Lateral propagation of gravity waves from midlatitude sources to 60 °S is a likely explanation for how gravity waves reach the stratospheric polar vortex which is not realistically approximated by current gravity wave drag parametrisation. In a case study, the a horizontal background removal and the gravity wave analysis setup is used to investigate the

propagation pathways that gravity waves take as well as the likely distribution of sources that contribute to a stratospheric wave field. Tracing waves back from the lower edge of the stratospheric polar vortex the distribution of likely sources and the propagation pathways taken show the importance of non-orographic sources and oblique propagation below 15 km altitude.

In particular, the introduction has posed the following research questions, which are addressed again here and answered briefly on the basis of the studies in the previous sections.

How well can gravity waves and background in different data sets be separated?

How does horizontal filtering perform as a gravity wave background removal in the presence of inertial instabilities signals compared to vertical filtering?

Spurious inertial instability structures are represented by “pancake” structures with large horizontal wavelength of usually several 1 000 km and short vertical wavelengths of less than 15 km. Vertical filtering has to remove vertical wavelengths down to 7 km to remove these structures from the artificial inertial instability data. The results after vertical filtering with commonly used cutoff wavelengths of 15 km for realistic model and satellite observations show therefore clear remnants of inertial instability structures in the inferred gravity wave perturbations. Beside remnants from inertial instability signals, the vertical filtering also struggles with anomalies at the tropical tropopause and the stratopause as well as with signals likely left by Kelvin waves in the tropical stratosphere. Horizontal filtering is able to remove spurious inertial instability structures from artificial signals, temperature fields of ECMWF’s reanalysis ERA5 as well as SABER observations. Effects at the tropopause and stratopause are handled easier by increasing the cutoff wavenumbers, which is addressed in more detail with the next question.

What is the optimal cutoff wavenumber for Numerical weather prediction (NWP) model product temperatures in the upper troposphere and lower stratosphere (UTLS) and the stratosphere respectively to avoid interference with other wavelike structures?

Applied on ERA5 temperature fields, horizontal filtering with cutoff wavenumbers larger than 6 gives generally satisfying results for the reduction of spurious inertial instability structures in the stratosphere. Also other global scale waves, such as Rossby waves are removed with wavenumber 6 in the stratosphere. To deal with remnants of Rossby waves in the subtropical UTLS region, a higher cutoff wavenumber was necessary. Removing wavenumbers up to 18 is generally sufficient in this case. A very high cutoff wavenumber, e.g. a removal up to wavenumber 42, reduces the magnitude of a gravity wave signal around the stratospheric jet stream and, hence, is unfavourable for gravity wave climatologies or gravity wave momentum flux balances. Infrared sounders on low-earth orbiting (LEO) satellites cover approximately 14 orbits per day and, therefore, resolve waves of wavenumber 7 in their data. The results of this study show that this resolution is sufficient to remove inertial instability remnants in the stratosphere and, thus, confirm work performed before in the remote sensing group at IEK-7. Overall a horizontal filtering approach with a cutoff wavenumber 6 gives the best results in areas where both inertial instabilities and gravity waves are present.

From which sources and through which pathways do gravity waves enter the southern polar vortex?

What source regions are important for a stratospheric wave field southeast of New Zealand?

Based on backward raytracing, major source regions of wave packets contributing to the stratospheric wave structure south of New Zealand were identified at New Zealand's topography, in a long streak along the tropospheric jet over the Tasman Sea as well as a jet exit region closer to the Australian east coast over the Tasman Sea. Other rays

terminate in smaller clusters in a streak extending from the south tip of the South Island of New Zealand to the southeast onto the ocean. These waves are likely trailing waves from orographic generation at the Southern Alps. Some rays trace back to Tasmania and mainland Australia, which are probably of orographic origin but advected eastwards by favourable wind conditions. Another smaller cluster is found far off to the west over the South Ocean at longitudes of the Australian west coast. These waves are probably generated somewhere along the tropospheric jet.

Most of these likely source regions lie north of 50 °S.

Which role do different source processes play in bringing momentum and energy to the lower stratosphere at 60 °S?

The “mountain” rays tracing back to significant orography are mostly generated by flow over the mountain ridge. This is supported by the close-to-zero phase speeds of many such rays. However, several rays show non-zero phase speeds suggesting that some waves are generated by other “orography-related” sources such as stagnation flow and associated convection. For the examined case, approximately a third of the traced wave packets are identified as orographic waves and these account for approximately 31% of the stratospheric GWMF calculated at 25 km altitude.

“Low-reaching” rays, i.e., rays that are terminated below 5 km altitude, are difficult to connect with certainty to a source process, because the source can in principle be located anywhere along the the ray path. Big clusters of ray termination locations over the Tasman Sea, however, indicate sources like frontal systems on the ocean. For the examined case, the largest group of the launched rays are identified as “low-reaching”. They account for approximately 42% of the calculated stratospheric GWMF in the wave field.

For the “high-terminated” rays terminating above 5 km altitude, only few wave sources, like instabilities at the tropospheric jet stream, are plausible compared to the low-reaching rays. The wind conditions at 8 km altitude 18 h before the ray launch in comparison with the local wave direction and structures in vertical wind fields from ECMWF operational

analyses indicate a jet exit region over the Tasman Sea that co-locates well with the location of a number of the “high-terminated” rays. Here, less than a third of the rays are identified as high-terminated rays and they contribute about 28% of the GWMF calculated for the stratospheric wave field.

Though the wave field south of New Zealand appears to be quite uniform, it is composed of waves from a variety of different source processes.

How do waves reach the region around 60 °S already in the lower stratosphere? What are likely propagation pathways?

By definition, this case study concentrated on gravity waves that reach higher latitudes already at rather low altitudes in the stratosphere, by launching the ray tracer from the wave field southeast of New Zealand at 25 km altitude backwards. The dominant propagation pathways of rays show lateral propagation already below 15 km altitude. The rays then reach regions of faster wind speeds, are refracted to longer vertical wavelengths, and quickly propagate upwards focusing into the stratospheric jet. This study supports the notion that far lateral propagation can already take place in the lowermost stratosphere. This propagation path could explain an apparent mismatch between high-resolution modelling results, placing gravity wave activity still at midlatitudes at 15 km, while superpressure balloon measurements find enhanced gravity wave activity already around 60 °S between 18 and 20 km altitude. A southwestward propagation direction of approximately 225 °, or 45 °south relative to the direction opposite to the mean wind are most efficient for lateral propagation.

Both, tools and the scientific results generated in this thesis will continue to be an essential part of IEK-7’s activities on gravity waves. The tools developed for this study will be employed on high-resolution atmospheric fields from the ICOsahedral Nonhydrostatic (ICON) model developed by Deutscher Wetterdienst (DWD) in the QUBICC project investigating the role of convective gravity waves for the quasi-bienniel oscillation (QBO). In particular, the findings from this case study have contributed to initiate the WASCLIM

project on the Role of the gravity waves in the Southern Hemispheric circulation and climate. Both projects are part of the joint research initiative “Role of the Middle atmosphere in Climate (ROMIC-II)”. A central part of WASCLIM will be a global investigation of ECMWF analysis products using a similar analysis setup to evaluate where the low-altitude, lateral gravity wave pathways are present and to identify dominant propagation paths statistically over a larger time frame. The climatology will then be used to facilitate a new parametrisation scheme that includes simplified horizontal propagation along these paths for integration in the ECHAM/MESSy Atmospheric Chemistry (EMAC) climate model.

List of Figures

List of Tables

List of acronyms

AIRS Atmospheric Infrared Sounder

CMAM Canadian Middle Atmosphere Model

CORAL Compact Rayleigh Autonomous Lidar

COSMIC Constellation Observing System for Meteorology Ionosphere and Climate

CRISTA Cryogenic Infrared Spectrometers and Telescopes forthe Atmosphere

DEEPWAVE Deep Propagating Gravity Wave Experiment (campaign)

DFT Discrete Fourier Transform

DWD Deutscher Wetterdienst (German Weather Service)

ECMWF European Centre for Medium-Range Weather Forecasts

ECMWF-IFS ECMWF's Integrated Forecast System

ERA5 ECMWF's current re-analysis product

FFT Fast Fourier Transform

GCM General circulation model

GLORIA Gimballed Limb Observer for Radiance Imaging of the Atmosphere

GPS Global Positioning System

GPS-RO Radio occultation from Global Positioning System data

GROGRAT Gravity-wave Regional Or Global Ray Tracer

GWMF Gravity wave momentum flux

HIRDLS High Resolution Dynamics Limb Sounder

ICON ICOsahedral Nonhydrostatic model

IDL Interactive Data Language

IEK-7 Institute for Energy and Climate research: Stratosphere (institute of Forschungszentrum Jülich

KIT Karlsruhe Institute of Technology

LEO Low earth orbiter (satellite)

MLS Microwave Limb Sounder (satellite experiment)

NWP Numerical Weather Prediction

PREMIER PRocess Exploitation through Measurements of Infrared and millimetre-wave Emitted Radiation (a proposed satellite experiment)

S3D three-dimensional sinusoidal fitting method for gravity wave characterisation

SABER Sounding of the Atmosphere using Broadband Emission Radiometry

UARS Upper AtmosphereResearch Satellite (satellite mission)

UTC Coordinated Universal Time

UTLS Upper Troposphere Lower Stratosphere

TIMED Thermosphere Ionosphere Mesosphere Energetics and Dynamics

QBO Quasi-biennial oscillation

WKB Wentzel-Kramers-Brillouin (approximation)

List of symbols

In this thesis, regular cursive symbols are used for real numbers and functions mapping into $\mathbb{R}$. Bold cursive font (e.g. $\boldsymbol{u}$) represents vectors and vector-valued functions. Symbols denoted with an apostrophe (e.g. u') describe the perturbation, with a tilde (e.g. $\tilde{u}$) the amplitude of the perturbation and with a bar (e.g. $\bar{u}$) the background state of the respective atmospheric quantity. A hat is used to refer to an intrinsic wave property (e.g. $\hat{\omega}$), i.e. the property as seen by an observer moving in the frame of reference with the background wind, while a subscript of *gb* (e.g. ω_{gb}) refers to the ground-based wave property, i.e. the property as seen by an immobile observer.

The following table contains the most important symbols used for mathematical notation and physical quantities:

$\boldsymbol{A}$	wave action
A, B	amplitudes in monochromatic wave model
c	phase speed; c_x, c_y along the directions of x and y respectively
c_h, c_z	horizontal respectively vertical phase speed
$\boldsymbol{c}_g$	group velocity; $\boldsymbol{c}_g = (c_{gx}, c_{gy}, c_{gz})$
$\boldsymbol{c}_{gh}$	horizontal group velocity; $c_{gh} = (c_{gx}, c_{gy})$
χ^2	sum of squares; cost function of the sinusoidal fit
$\boldsymbol{f}$	Coriolis frequency
$\boldsymbol{f}(\boldsymbol{x}, \boldsymbol{k})$	monochromatic wave model for sinusoidal fit
$\boldsymbol{F}_p$	vertical flux of horizontal momentum (gravity wave (pseudo)momentum flux); $\boldsymbol{F}_p = (F_{px}, F_{py})$
g	gravity acceleration

H	atmospheric scale height
$H_n(\lambda_z)$	filter function of Butterworth filter with order n
$\boldsymbol{k}$	wave vector; $\boldsymbol{k} = (k, l, m)$
k_c	cutoff wave number
$\boldsymbol{k}_h$	horizontal wave vector; $\boldsymbol{k}_h = (k, l)$
k_h	horizontal wave number; $k_h = \sqrt{k^2 + l^2}$
κ	scaling factor; $\kappa = k^2 + l^2 + m^2 + \frac{1}{4H^2}$
λ_c	cutoff wavelength
λ_h	horizontal wavelength; $\lambda_h = \frac{2\pi}{k_h}$
λ_z	vertical wavelength
N	buoyancy frequency
ω	wave frequency
p	pressure
ϕ	wave direction
$\mathfrak{Re}$	real part of a complex number
ρ	density
T	temperature
t	time
τ	wave period; $\tau = \frac{2\pi}{\omega}$
θ	potential temperature
u	zonal wind component
u_h	horizontal wind magnitude
v	meridional wind component
w	vertical wind component
$\boldsymbol{x}$	position in space; $\boldsymbol{x} = (x, y, z)$
ζ	vertical displacement
$\langle . \rangle$	zonal mean of a quantity
$var(.)$	variance of a quantity
$\boldsymbol{a} \cdot \boldsymbol{b}$	scalar product of vectors $\boldsymbol{a}$ and $\boldsymbol{b}$

Bibliography

M. J. Alexander. Global and seasonal variations in three-dimensional gravity wave momentum flux from satellite limb-sounding temperatures. *Geophys. Res. Lett.*, 42(16): 6860–6867, AUG 28 2015. ISSN 0094-8276. doi: $10.1002/2015\mathrm{GL}065234$.

M. J. Alexander and C. D. Barnet. Using satellite observations to constrain gravity wave parameterizations for global models. *J. Atmos. Sci.*, 64(5):1652–1665, 2007.

M. J. Alexander and A. W. Grimsdell. Seasonal cycle of orographic gravity wave occurrence above small islands in the Southern Hemisphere: Implications for effects on the general circulation. *J. Geophys. Res. Atmos.*, 118(20):11589–11599, OCT 27 2013. ISSN 2169-897X. doi: $10.1002/2013\mathrm{JD}020526$.

M. J. Alexander and K. H. Rosenlof. Gravity-wave forcing in the stratosphere: Observational constraints from the upper atmosphere research satellite and implications for parameterization in global models. *J. Geophys. Res.*, 108(D19):4597, 2003. doi: $10.1029/2003\mathrm{JD}003373$.

M. J. Alexander, J. R. Holton, and D. R. Durran. The gravity wave response above deep convection in a squall line simulation. *J. Atmos. Sci.*, 52:2212–2226, 1995.

M. J. Alexander, J. H. Beres, and L. Pfister. Tropical stratospheric gravity wave activity and relationships to clouds. *J. Geophys. Res.*, 105(D17):22299–22309, 2000. doi: $10.1029/2000\mathrm{JD}900326$.

M. J. Alexander, T. Tsuda, and R. A. Vincent. On the latitudinal variations observed in gravity waves with short vertical wavelengths. *J. Atmos. Sci.*, 59:1394–1404, 2002.

M. J. Alexander, J. Gille, C. Cavanaugh, M. Coffey, C. Craig, V. Dean, T. Eden, G. Francis, C. Halvorson, J. Hannigan, R. Khosravi, D. Kinnison, H. Lee, S. Massie, and B. Nardi. Global estimates of gravity wave momentum flux from High Resolution Dynamics Limb Sounder (HIRDLS) observations. *J. Geophys. Res.*, 113, 2008a. doi: $10.1029/2007\mathrm{JD}008807$.

M. J. Alexander, M. Geller, C. McLandress, S. Polavarapu, P. Preusse, F. Sassi, K. Sato, S. Eckermann, M. Ern, A. Hertzog, Y. Kawatani, M. Pulido, T. A. Shaw, M. Sigmond, R. Vincent, and S. Watanabe. Recent developments in gravity-wave effects in climate models and the global distribution of gravity-wave momentum flux from observations and models. *Quart. J. Roy. Meteorol. Soc.*, 136:1103–1124, 2010. ISSN 0035-9009. doi: $10.1002/\mathrm{qj}.637$.

S. P. Alexander, T. Tsuda, Y. Kawatani, and M. Takahashi. Global distribution of atmospheric waves in the equatorial upper troposphere and lower stratosphere: Cosmic observations of wave mean flow interactions. *J. Geophys. Res.*, 113, 2008b. doi: $10.1029/2008\mathrm{JD}010039$.

D. G. Andrews, J. R. Holton, and C. B. Leovy. *Middle Atmosphere Dynamics*, volume 40 of *International Geophysics Series*. Academic Press, 1987.

J. Artru, V. Ducic, H. Kanamori, P. Lognonne, and M. Murakami. Ionospheric detection of gravity waves induced by tsunamis. *Geophys. J. Int.*, 160(3):840–848, MAR 2005. ISSN 0956-540X. doi: $10.1111/\mathrm{j}.1365\text{-}246\mathrm{X}.2005.02552.\mathrm{x}$.

J. T. Bacmeister. Mountain-wave drag in the stratosphere and mesosphere inferred from observed winds and a simple mountain-wave parameterization scheme. *J. Atmos. Sci.*, 50:377–399, 1993.

T. J. Bacmeister, S. D. Eckermann, P. A. Newman, L. Lait, K. R. Chan, M. Loewenstein, M. H. Porffitt, and B. L. Gary. Stratospheric horizontal wavenumber spectra of winds, potential temperature and atmospheric tracers observed by high-altitude aircraft. *J. Geophys. Res.*, 101:9441–9470, 1996. doi: $10.1029/95\mathrm{JD}03835$.

M. P. Baldwin, L. J. Gray, T. J. Dunkerton, K. Hamilton, P. H. Haynes, W. J. Randel, J. R. Holton, M. J. Alexander, I. Hirota, T. Horinouchi, D. B. A. Jones, J. S. Kinnersley, C. Marquardt, K. Sato, and M. Takahashi. The quasi-biennial oscillation. *Rev. Geophys.*, 39: 179–229, 2001. doi: 10.1029/1999RG000073.

J. Barnett and K. Labitzke. Climatological distribution of planetary waves in the middle atmosphere. *Adv. Space Res.*, 10:1263–1291, 1990.

G. Boeloeni, B. Ribstein, J. Muraschko, C. Sgoff, J. Wei, and U. Achatz. The Interaction between Atmospheric Gravity Waves and Large-Scale Flows: An Efficient Description beyond the Nonacceleration Paradigm. *J. Atmos. Sci.*, 73(12):4833–4852, December 2016. ISSN 0022-4928. doi: 10.1175/JAS-D-16-0069.1.

M. Bramberger, A. Doernbrack, K. Bossert, B. Ehard, D. C. Fritts, B. Kaifler, C. Mallaun, A. Orr, P. D. Pautet, M. Rapp, M. J. Taylor, S. Vosper, B. P. Williams, and B. Witschas. Does strong tropospheric forcing cause large-amplitude mesospheric gravity waves? a deepwave case study. *J. Geophys. Res. Atmos.*, 122(21):11,422–11,443, NOV 16 2017. ISSN 2169-897X. doi: 10.1002/2017JD027371.

O. Bühler. On shear-generated gravity waves that reach the mesosphere. part i: Wave generation. *J. Atmos. Sci.*, 56:3749–3773, 1999.

N. Butchart, I. Cionni, V. Eyring, T. G. Shepherd, D. W. Waugh, H. Akiyoshi, J. Austin, C. Brühl, M. P. Chipperfield, E. Cordero, M. Dameris, R. Deckert, S. Dhomse, S. M. Frith, R. R. Garcia, A. Gettelman, M. A. Giorgetta, D. E. Kinnison, F. Li, E. Mancini, C. McLandress, S. Pawson, G. Pitari, D. A. Plummer, E. Rozanov, F. Sassi, J. F. Scinocca, K. Shibata, B. Steil, and W. Tian. Chemistry-climate model simulations of twenty-first century stratospheric climate and circulation changes. *J. Clim.*, 23:5349–5374, 2010.

O. Bühler, J. Callies, and R. Ferrari. Wave–vortex decomposition of one-dimensional ship-track data. *J. Fluid Mech.*, 756:1007–1026, 2014. doi: 10.1017/jfm.2014.488.

J. G. Charney and P. G. Drazin. Propagation of planetary-scale disturbances from the

lower into the upper atmosphere. *J. Geophys. Res.*, 66(1):83–109, 1961. doi: 10.1029/JZ066i001p00083.

D. Chen, C. Strube, M. Ern, P. Preusse, and M. Riese. Global analysis for periodic variations in gravity wave squared amplitudes and momentum fluxes in the middle atmosphere. *Ann. Geophys.*, 37(4):487–506, 2019. doi: 10.5194/angeo-37-487-2019. URL https://www.ann-geophys.net/37/487/2019/.

T. L. Clark, T. Hauf, and J. P. Kuettner. Convectively forced internal gravity waves: Results from two-dimensional numerical experiments. *Quart. J. Roy. Meteorol. Soc.*, 112(474): 899–925, 1986. doi: 10.1002/qj.49711247402.

S. De Angelis, S. R. McNutt, and P. W. Webley. Evidence of atmospheric gravity waves during the 2008 eruption of Okmok volcano from seismic and remote sensing observations. *Geophys. Res. Lett.*, 38, MAY 18 2011. ISSN 0094-8276. doi: 10.1029/2011GL047144.

A. de la Torre, T. Schmidt, and J. Wickert. A global analysis of wave potential energy in the lower and middle atmosphere from CHAMP and SAC-C GPS-RO long term data. *Geophys. Res. Lett.*, 33, 2006. doi: 10.1029/2006GL027696.

E. M. Dewan, R. H. Picard, R. R. O'Neil, H. A. Gardiner, J. Gibson, J. D. Mill, E. Richards, M. Kendra, and W. O. Gallery. MSX satellite observations of thunderstorm-generated gravity waves in mid-wave infrared images of the upper stratosphere. *Geophys. Res. Lett.*, 25(7):939–942, 1998.

D. I. V. Domeisen, O. Martius, and B. Jiménez-Esteve. Rossby wave propagation into the northern hemisphere stratosphere: The role of zonal phase speed. *Geophys. Res. Lett.*, 45(4):2064–2071, 2018. doi: 10.1002/2017GL076886.

T. J. Dunkerton. On the inertial stability of the equatorial middle atmosphere. *J. Atmos. Sci.*, 38(11):2354–2364, 1981. doi: 10.1175/1520-0469(1981)038<2354:OTISFT>2.0.CO;2.

T. J. Dunkerton. Shear instability of internal inertia-gravity waves. *J. Atmos. Sci.*, 54: 1628–1641, 1997.

S. D. Eckermann. Hodographic analysis of gravity waves: Relationships among stokes parameters, rotary spectra and cross-spectral methods. *J. Geophys. Res.*, 101:169–174, 1996.

S. D. Eckermann. Influence of wave propagation on the doppler spreading of atmospheric gravity waves. *J. Atmos. Sci.*, 54:2554–2573, 1997.

S. D. Eckermann and C. J. Marks. An idealized ray model of gravity wave-tidal interactions. *J. Geophys. Res.*, 101:195–212, 1996.

S. D. Eckermann and P. Preusse. Global measurements of stratospheric mountain waves from space. *Science*, 286(5444):1534–1537, 1999. doi: 10.1126/science.286.5444.1534.

ECMWF. *PART III: DYNAMICS ANDNUMERICAL PROCEDURES*. Number 3 in IFS Documentation. ECMWF, 2019. URL `https://www.ecmwf.int/node/19307`.

B. Ehard, B. Kaifler, N. Kaifler, and M. Rapp. Evaluation of methods for gravity wave extraction from middle-atmospheric lidar temperature measurements. *Atmos. Meas. Tech.*, 8(11):4645–4655, 2015. doi: 10.5194/amt-8-4645-2015.

B. Ehard, B. Kaifler, A. Dörnbrack, P. Preusse, S. Eckermann, M. Bramberger, S. Gisinger, N. Kaifler, B. Liley, J. Wagner, and M. Rapp. Horizontal propagation of large amplitude mountain waves in the vicinity of the polar night jet. *J. Geophys. Res. Atmos.*, pages 1423–1436, 2017. ISSN 2169-8996. doi: 10.1002/2016JD025621. URL `http://dx.doi.org/10.1002/2016JD025621`. 2016JD025621.

B. Ehard, S. Malardel, A. Doernbrack, B. Kaifler, N. Kaifler, and N. Wedi. Comparing ECMWF high-resolution analyses with lidar temperature measurements in the middle atmosphere. *Quart. J. Roy. Meteorol. Soc.*, 144(712, A):633–640, APR 2018. doi: 10.1002/qj.3206.

G. Eidmann, D. Offermann, and P. Preusse. Fluctuation power spectra in the mid stratosphere at increased horizontal resolution. *Adv. Space Res.*, 27(10):1647–1652, 2001. doi: 10.1016/S0273-1177(01)00230-7.

M. Ern, P. Preusse, M. J. Alexander, and C. D. Warner. Absolute values of gravity wave momentum flux derived from satellite data. *J. Geophys. Res. Atmos.*, 109(D20), 2004. ISSN 2156-2202. doi: 10.1029/2004JD004752.

M. Ern, P. Preusse, and C. D. Warner. Some experimental constraints for spectral parameters used in the Warner and McIntyre gravity wave parameterization scheme. *Atmos. Chem. Phys.*, 6(12):4361–4381, 2006. doi: 10.5194/acp-6-4361-2006.

M. Ern, C. Lehmann, M. Kaufmann, and M. Riese. Spectral wave analysis at the mesopause from SCIAMACHY airglow data compared to SABER temperature spectra. *Ann. Geophys.*, 27:407–416, 2009. doi: 10.5194/angeo-27-407-2009.

M. Ern, P. Preusse, J. C. Gille, C. L. Hepplewhite, M. G. Mlynczak, J. M. Russell III, and M. Riese. Implications for atmospheric dynamics derived from global observations of gravity wave momentum flux in stratosphere and mesosphere. *J. Geophys. Res.*, 116, 2011. doi: 10.1029/2011JD015821.

M. Ern, P. Preusse, S. Kalisch, M. Kaufmann, and M. Riese. Role of gravity waves in the forcing of quasi two-day waves in the mesosphere: An observational study. *J. Geophys. Res. Atmos.*, 118(9):3467–3485, 2013. ISSN 2169-8996. doi: 10.1029/2012JD018208.

M. Ern, F. Ploeger, P. Preusse, J. C. Gille, L. J. Gray, S. Kalisch, M. G. Mlynczak, J. M. Russell III, and M. Riese. Interaction of gravity waves with the QBO: A satellite perspective. *J. Geophys. Res. Atmos.*, 119:2329–2355, 2014. doi: 10.1002/2013JD020731.

M. Ern, Q. T. Trinh, P. Preusse, J. C. Gille, M. G. Mlynczak, J. M. Russell III, and M. Riese. GRACILE: A comprehensive climatology of atmospheric gravity wave parameters based on satellite limb soundings. *Earth Syst. Sci. Dat.*, 10:857–892, 2018. doi: 10.5194/essd-10-857-2018. URL `https://www.earth-syst-sci-data.net/10/857/2018/`.

M. Ern, P. Preusse, and M. Riese. Driving of the SAO by gravity waves as observed from satellite. *Ann. Geophys.*, 33(4):483–504, 2015. ISSN 0992-7689. doi: 10.5194/angeo-33-483-2015.

M. Ern, Q. T. Trinh, M. Kaufmann, I. Krisch, P. Preusse, J. Ungermann, Y. Zhu, J. C. Gille, M. G. Mlynczak, J. M. Russell, III, M. J. Schwartz, and M. Riese. Satellite observations of middle atmosphere gravity wave absolute momentum flux and of its vertical gradient during recent stratospheric warmings. *Atmos. Chem. Phys.*, 16(15):9983–10019, AUG 9 2016. ISSN 1680-7316. doi: 10.5194/acp-16-9983-2016.

M. Ern, L. Hoffmann, and P. Preusse. Directional gravity wave momentum fluxes in the stratosphere derived from high-resolution AIRS temperature data. *Geophys. Res. Lett.*, 44(1):475–485, JAN 2017. ISSN 0094-8276. doi: 10.1002/2016GL072007.

ESA. *Candidate Earth Explorer Core Missions - Report for Assessment: PREMIER - PRocess Exploitation through Measurements of Infrared and millimetre-wave Emitted Radiation*. Number SP-1313/5. ESA Publications Division, ESTEC, Keplerlaan 1, 2200 AG Noordwijk, The Netherlands, 2008.

E. J. Fetzer and J. C. Gille. Gravity wave variance in LIMS temperatures. part I: Variability and comparison with background winds. *J. Atmos. Sci.*, 51(17):2461–2483, 1994. doi: 10.1175/1520-0469(1994)051<2461:GWVILT>2.0.CO;2.

R. Fovell, D. Durran, and J. R. Holton. Numerical simulations of convectively generated stratospheric gravity waves. *J. Atmos. Sci.*, 49:1427–1442, 1992.

F. Friedl-Vallon, T. Gulde, F. Hase, A. Kleinert, T. Kulessa, G. Maucher, T. Neubert, F. Olschewski, C. Piesch, P. Preusse, H. Rongen, C. Sartorius, H. Schneider, A. Schönfeld, V. Tan, N. Bayer, J. Blank, R. Dapp, A. Ebersoldt, H. Fischer, F. Graf, T. Guggenmoser, M. Höpfner, M. Kaufmann, E. Kretschmer, T. Latzko, H. Nordmeyer, H. Oelhaf, J. Orphal, M. Riese, G. Schardt, J. Schillings, M. K. Sha, O. Sumińska-Ebersoldt, and J. Ungermann. Instrument concept of the imaging Fourier transform spectrometer GLORIA. *Atmos. Meas. Tech.*, 7(10):3565–3577, 2014. doi: 10.5194/amt-7-3565-2014.

D. Fritts and M. Alexander. Gravity wave dynamics and effects in the middle atmosphere. *Rev. Geophys.*, 41(1), APR 16 2003. ISSN 8755-1209. doi: 10.1029/2001RG000106.

D. C. Fritts and P. K. Rastogi. Convective and dynamical instabilities due to gravity wave motions in the lower and middle atmosphere: theory and observations. *Radio Sci.*, 20: 1247–1277, 1985.

J. Galewsky. Orographic clouds in terrain-blocked flows: an idealized modeling study. *J. Atmos. Sci.*, 65(11):3460–3478, NOV 2008. ISSN 0022-4928. doi: 10.1175/2008JAS2435.1.

R. Garcia and M. Salby. Transient-response to localized episodic heating in the tropics. 2. far-field behavior. *J. Atmos. Sci.*, 44(2):499–530, JAN 15 1987. ISSN 0022-4928. doi: {10.1175/1520-0469(1987)044<0499:TRTLEH>2.0.CO;2}.

R. R. Garcia, T. J. Dunkerton, R. S. Lieberman, and R. A. Vincent. Climatology of the semiannual oscillation of the tropical middle atmosphere. *J. Geophys. Res.*, 102: 26019–26032, 1997.

R. R. Garcia, A. K. Smith, D. E. Kinnison, A. de la Camara, and D. J. Murphy. Modification of the gravity wave parameterization in the whole atmosphere community climate model: Motivation and results. *J. Atmos. Sci.*, 74(1):275–291, 2017. doi: 10.1175/JAS-D-16-0104.1.

M. A. Geller, M. J. Alexander, P. T. Love, J. Bacmeister, M. Ern, A. Hertzog, E. Manzini, P. Preusse, K. Sato, A. A. Scaife, and T. Zhou. A comparison between gravity wave momentum fluxes in observations and climate models. *J. Clim.*, 26(17):6383–6405, SEP 2013. ISSN 0894-8755. doi: 10.1175/JCLI-D-12-00545.1.

A. J. Gerrard, T. J. Kane, S. D. Eckermann, and J. P. Thayer. Gravity waves and mesospheric clouds in the summer middle atmosphere: A comparison of lidar measurements and ray modeling of gravity waves over sonderstrom, greenland. *J. Geophys. Res.*, 109, 2004. doi: 10.1029/2002JD002783.

S. Gisinger, A. Doernbrack, V. Matthias, J. D. Doyle, S. D. Eckermann, B. Ehard, L. Hoffmann, B. Kaifler, C. G. Kruse, and M. Rapp. Atmospheric conditions during the Deep Propagating Gravity Wave Experiment (DEEPWAVE). *Mon. Weath. Rev.*, 145(10): 4249–4275, OCT 2017. ISSN 0027-0644. doi: 10.1175/MWR-D-16-0435.1.

E. E. Gossard and W. H. Hooke. Waves in the atmosphere, atmospheric infrasound and gravity waves - their generation and propagation. *Elsevier Scientific Publishing Company*, 1975.

F. Guest, M. Reeder, C. Marks, and D. Karoly. Inertia-gravity waves observed in the lower stratosphere over macquarie island. *J. Atmos. Sci.*, 57(5):737–752, 2000.

V. L. Harvey and J. A. Knox. Beware of inertial instability masquerading as gravity waves in stratospheric temperature perturbations. *Geophysical Research Letters*, 46 (3):1740–1745, 2019. doi: 10.1029/2018GL081142.

A. Hasha, O. Bühler, and J. Scinocca. Gravity wave refraction by three-dimensionally varying winds and the global transport of angular momentum. *J. Atmos. Sci.*, 65:2892–2906, 2008.

H. Hayashi, M. Shiotani, and J. C. Gille. Vertically stacked temperature disturbances near the equatorial stratopause as seen in cryogenic limb array etalon spectrometer data. *J. Geophys. Res.*, 103(D16):19469–19483, 1998. doi: 10.1029/98JD01730.

E. A. Hendricks, J. D. Doyle, S. D. Eckermann, Q. Jiang, and P. A. Reinecke. What is the source of the stratospheric gravity wave belt in austral winter? *J. Atmos. Sci.*, 71(5): 1583–1592, 2014. doi: 10.1175/JAS-D-13-0332.1.

A. Hertzog, G. Boccara, R. A. Vincent, F. Vial, and P. Cocquerez. Estimation of gravity wave momentum flux and phase speeds from quasi-Lagrangian stratospheric balloon flights. part ii: Results from the vorcore campaign in antarctica. *J. Atmos. Sci.*, 65(10): 3056–3070, 2008. doi: 10.1175/2008JAS2710.1.

N. P. Hindley, C. J. Wright, N. D. Smith, and N. J. Mitchell. The southern stratospheric gravity wave hot spot: individual waves and their momentum fluxes measured by COS-

MIC GPS-RO. *Atmos. Chem. Phys.*, 15(14):7797–7818, 2015. ISSN 1680-7316. doi: 10.5194/acp-15-7797-2015.

L. Hoffmann and M. J. Alexander. Retrieval of stratospheric temperatures from Atmospheric Infrared Sounder radiance measurements for gravity wave studies. *J. Geophys. Res.*, 114:D07105, 2009. doi: 10.1029/2008JD011241.

L. Hoffmann and M. J. Alexander. Occurrence frequency of convective gravity waves during the North American thunderstorm season. *J. Geophys. Res.*, 115, 2010. doi: 10.1029/2010JD014401.

L. A. Holt, M. J. Alexander, L. Coy, C. Liu, A. Molod, W. Putman, and S. Pawson. An evaluation of gravity waves and gravity wave sources in the Southern Hemisphere in a 7 km global climate simulation. *Quart. J. Roy. Meteorol. Soc.*, 143(707, B):2481–2495, JUL 2017. ISSN 0035-9009. doi: 10.1002/qj.3101.

J. R. Holton. The role of gravity wave induced drag and diffusion on the momentum budget of the mesosphere. *J. Atmos. Sci.*, 39(4):791–799, 1982.

J. R. Holton. *An Introduction to Dynamic Meteorology*. Academic Press Limited, 1992. 3rd edition.

R. A. Houze, Jr. Orographic effects on precipitating couds. *Rev. Geophys.*, 50:RG1001, JAN 6 2012. ISSN 8755-1209. doi: 10.1029/2011RG000365.

V. Jewtoukoff, A. Hertzog, R. Plougonven, A. de la Camara, and F. Lott. Comparison of Gravity Waves in the Southern Hemisphere Derived from Balloon Observations and the ECMWF Analyses. *J. Atmos. Sci.*, 72(9):3449–3468, SEP 2015. ISSN 0022-4928. doi: 10.1175/JAS-D-14-0324.1.

Q. Jiang, J. D. Doyle, S. D. Eckermann, and B. P. Williams. Stratospheric trailing gravity waves from New Zealand. *J. Atmos. Sci.*, 76(6):1565–1586, JUN 2019. ISSN 0022-4928. doi: 10.1175/JAS-D-18-0290.1.

R. M. Jones and A. J. Bedard. Atmospheric gravity wave ray tracing: Ordinary and extraordinary waves. *J. Atm. Sol.-Terr. Phys.*, 179:342–357, NOV 2018. ISSN 1364-6826. doi: 10.1016/j.jastp.2018.08.014.

S. Kalisch, P. Preusse, M. Ern, S. D. Eckermann, and M. Riese. Differences in gravity wave drag between realistic oblique and assumed vertical propagation. *J. Geophys. Res. Atmos.*, 119:10,081–10,099, 2014. ISSN 2169-8996. doi: 10.1002/2014JD021779.

S. Kalisch, H. Y. Chun, M. Ern, P. Preusse, Q. T. Trinh, S. D. Eckermann, and M. Riese. Comparison of simulated and observed convective gravity waves. *J. Geophys. Res. Atmos.*, 121(22):13474–13492, NOV 27 2016. ISSN 2169-897X. doi: 10.1002/2016JD025235.

Y.-H. Kim, G. N. Kiladis, J. R. Albers, J. Dias, M. Fujiwara, J. A. Anstey, I.-S. Song, C. J. Wright, Y. Kawatani, F. Lott, and C. Yoo. Comparison of equatorial wave activity in the tropical tropopause layer and stratosphere represented in reanalyses. *Atmos. Chem. Phys.*, 19(15):10027–10050, 2019. doi: 10.5194/acp-19-10027-2019.

Y.-J. Kim, S. D. Eckermann, and H.-Y. Chun. An overview of the past, present and future of gravity-wave drag parameterization for numerical climate and weather prediction models. *Atmosphere-Ocean*, 41:65–98, 2003.

J. A. Knox and V. L. Harvey. Global climatology of inertial instability and rossby wave breaking in the stratosphere. *J. Geophys. Res. Atmos.*, 110(D6), 2005. doi: 10.1029/2004JD005068.

S. E. Koch and L. M. Siedlarz. Mesoscale gravity waves and their environment in the central united states during storm-fest. *Mon. Weath. Rev.*, 127:2854–2879, 1999.

I. Krisch, P. Preusse, J. Ungermann, A. Dörnbrack, S. D. Eckermann, M. Ern, F. Friedl-Vallon, M. Kaufmann, H. Oelhaf, M. Rapp, C. Strube, and M. Riese. First tomographic observations of gravity waves by the infrared limb imager gloria. *Atmos. Chem. Phys.*, 17(24):14937–14953, 2017. doi: 10.5194/acp-17-14937-2017.

I. Krisch, M. Ern, L. Hoffmann, P. Preusse, C. Strube, J. Ungermann, W. Woiwode, and M. Riese. Superposition of gravity waves with different propagation characteristics observed by airborne and space-borne infrared sounders. *Atmos. Chem. Phys. Discuss.*, 2020:1–31, 2020. doi: $10.5194/\text{acp-}2020\text{-}327$. URL `https://www.atmos-chem-phys-discuss.net/acp-2020-327/`.

T. P. Lane, M. J. Reeder, and T. L. Clark. Numerical modeling of gravity wave generation by deep tropical convection. *J. Atmos. Sci.*, 58(10):1249–1274, 2001. doi: $10.1175/1520\text{-}0469(2001)058{<}1249{:}\text{NMOGWG}{>}2.0.\text{CO};2$.

C. I. Lehmann, Y.-H. Kim, P. Preusse, H.-Y. Chun, M. Ern, and S.-Y. Kim. Consistency between fourier transform and small-volume few-wave decomposition for spectral and spatial variability of gravity waves above a typhoon. *Atmos. Meas. Tech.*, 5(7):1637–1651, 2012. doi: $10.5194/\text{amt-}5\text{-}1637\text{-}2012$.

M. J. Lighthill. On sound generated aerodynamically i. general theory. *Proc. R. Soc. Lond*, page 564–587, 1952.

M. J. Lighthill. Waves in fluids. *Cambridge University Press*, page 504pp, 1978.

E. Lindborg. A helmholtz decomposition of structure functions and spectra calculated from aircraft data. *J. Fluid Mech.*, 762:R4, 2015. doi: $10.1017/\text{jfm}.2014.685$.

R. S. Lindzen. Turbulence and stress due to gravity wave and tidal breakdown. *J. Geophys. Res.*, 86:9707–9714, 1981.

R. S. Lindzen and J. R. Holton. A theory of the quasi-biennial oscillation. *J. Atmos. Sci.*, 25(6):1095–1107, 1968.

E. Manzini and N. A. McFarlane. The effect of varying the source spectrum of a gravity wave parameterization in a middle atmosphere general circulation model. *J. Geophys. Res.*, 103:31523–31539, 1998.

C. J. Marks and S. D. Eckermann. A three-dimensional nonhydrostatic ray-tracing model for gravity waves: Formulation and preliminary results for the middle atmosphere.

J. Atmos. Sci., 52(11):1959–1984, 1995. doi: 10.1175/1520-0469(1995)052<1959:ATDNRT>2.0.CO;2.

C. McLandress. On the importance of gravity waves in the middle atmosphere and their parameterization in general circulation models. *J. Atm. Sol.-Terr. Phys.*, 60:1357–1383, 1998. doi: 10.1016/S1364-6826(98)00061-3.

C. McLandress and T. G. Shepherd. Simulated anthropogenic changes in the Brewer-Dobson circulation, including its extension to high latitudes. *J. Clim.*, 22:1516–1540, 2009. doi: 10.1175/2008JCLI2679.1.

C. McLandress, M. J. Alexander, and D. L. Wu. Microwave Limb Sounder observations of gravity waves in the stratosphere: A climatology and interpretation. *J. Geophys. Res.*, 105(D9):11947–11967, 2000.

C. McLandress, T. G. Shepherd, S. Polavarapu, and S. R. Beagley. Is Missing Orographic Gravity Wave Drag near 60 degrees S the Cause of the Stratospheric Zonal Wind Biases in Chemistry Climate Models? *J. Atmos. Sci.*, 69(3):802–818, MAR 2012. ISSN 0022-4928. doi: 10.1175/JAS-D-11-0159.1.

C. J. Nappo. *An Introduction to Atmospheric Gravity Waves*. Academic Press, second edition, 2012. ISBN 978-0-12-385223-6.

NASA Visible Earth. Atmospheric gravity waves and internal waves off australia. URL `https://visibleearth.nasa.gov/images/69463/atmospheric-gravity-waves-and-internal-waves-off-australia`.

G. Nastrom, D. Fritts, and K. Gage. An investigation of terrain effects on the mesoscale spectrum of atmospheric motions. *J. Atmos. Sci.*, 44(20):3087–3096, OCT 15 1987. ISSN 0022-4928. doi: {10.1175/1520-0469(1987)044<3087:AIOTEO>2.0.CO;2}.

G. D. Nastrom and D. C. Fritts. Sources of mesoscale variability of gravity waves. part i: topographic excitation. *J. Atmos. Sci.*, 49:101–110, 1992.

A. Orr, P. Bechtold, J. Scinocca, M. Ern, and M. Janiskova. Improved middle atmosphere climate and forecasts in the ECMWF model through a nonorographic gravity wave drag parameterization. *J. Clim.*, 23:5905–5926, 2010.

S. Pawson and T. Kubitz. Climatology of planetary waves in the northern stratosphere. *J. Geophys. Res. Atmos.*, 101(D12):16987–16996, JUL 27 1996. ISSN 0148-0227. doi: 10.1029/96JD01226.

J. Perret, C. Wright, N. Hindley, L. Hoffmann, N. Mitchell, P. Preusse, C. Strube, and S. Eckermann. Determining gravity wave sources and propagation over the southern ocean by ray-tracing airs measurements. *Geophys. Res. Lett.*, page under review, 2020.

L. Pfister, S. Scott, M. Loewenstein, S. Bowen, and M. Legg. Mesoscale disturbances in the tropical stratosphere excited by convection: Observations and effects on the stratospheric momentum budget. *J. Atmos. Sci.*, 50(8):1058–1075, 1993.

C. Piani, D. Durran, M. J. Alexander, and J. R. Holton. A numerical study of three-dimensional gravity waves triggered by deep tropical convection and their role in the dynamics of the qbo. *J. Atmos. Sci.*, 57(22):3689–3702, 2000. doi: 10.1175/1520-0469(2000)057<3689:ANSOTD>2.0.CO;2.

Pint. Pint: makes units easy. https://pint.readthedocs.io/en/stable/, 2020.

R. Plougonven and C. Snyder. Gravity waves excited by jets: Propagation versus generation. *Geophys. Res. Lett.*, 32, 2005. doi: 10.1029/2005GL023730.

R. Plougonven and F. Zhang. Internal gravity waves from atmospheric jets and fronts. *Rev. Geophys.*, 52(1):33–76, MAR 2014. ISSN 8755-1209. doi: 10.1002/2012RG000419.

R. Plougonven, A. de la Camara, V. Jewtoukoff, A. Hertzog, and F. Lott. On the relation between gravity waves and wind speed in the lower stratosphere over the Southern Ocean. *J. Atmos. Sci.*, 74(4):1075–1093, APR 2017. ISSN 0022-4928. doi: 10.1175/JAS-D-16-0096.1.

T. C. Portele, A. Doernbrack, J. S. Wagner, S. Gisinger, B. Ehard, P.-D. Pautet, and M. Rapp. Mountain-wave propagation under transient tropospheric forcing: A DEEP-WAVE case study. *Mon. Weath. Rev.*, 146(6):1861–1888, JUN 2018. ISSN 0027-0644. doi: 10.1175/MWR-D-17-0080.1.

M. Pramitha, M. Venkat Ratnam, A. Taori, B. V. Krishna Murthy, D. Pallamraju, and S. Vijaya Bhaskar Rao. Evidence for tropospheric wind shear excitation of high-phase-speed gravity waves reaching the mesosphere using the ray-tracing technique. *Atmos. Chem. Phys.*, 15:2709–2721, 2015. doi: 10.5194/acp-15-2709-2015.

W. H. Press, S. A. Teukolsky, W. T. Vetterling, and B. P. Flannery. Numerical recipes in fortran 77, the art of scientific computing, second edition. *Cambridge University Press*, page 933, 1992.

P. Preusse. *Satellitenmessungen von Schwerewellen in der mittleren Atmosphäre mit CRISTA*. PhD thesis, Wuppertal University, 2001. PhD thesis.

P. Preusse, B. Schaeler, D. Offermann, and S. D. Eckermann. Mountain lee waves over south america - a case study on the sensitivity to spatial short scales. *Air pollution research report*, 69(EUR 18912 EN), 1999.

P. Preusse, G. Eidmann, S. D. Eckermann, B. Schaeler, R. Spang, and D. Offermann. Indications of convectively generated gravity waves in CRISTA temperatures. *Adv. Space Res.*, 27(10):1653–1658, 2001.

P. Preusse, A. Dörnbrack, S. D. Eckermann, M. Riese, B. Schaeler, J. T. Bacmeister, D. Broutman, and K. U. Grossmann. Space-based measurements of stratospheric mountain waves by CRISTA, 1. sensitivity, analysis method, and a case study. *J. Geophys. Res.*, 107(D23)(8178), 2002. doi: 10.1029/2001JD000699.

P. Preusse, S. D. Eckermann, M. Ern, F. J. Schmidlin, M. J. Alexander, and D. Offermann. Infrared limb sounding measurements of middle-atmosphere gravity waves by CRISTA. In *Proceedings of SPIE*, volume 4882, pages 134–148, 2003.

P. Preusse, M. Ern, S. D. Eckermann, C. D. Warner, R. H. Picard, P. Knieling, M. Krebsbach, J. M. Russell III, M. G. Mlynczak, C. J. Mertens, and M. Riese. Tropopause to mesopause gravity waves in August: measurement and modeling. *J. Atm. Sol.-Terr. Phys.*, 68:1730–1751, 2006.

P. Preusse, S. D. Eckermann, and M. Ern. Transparency of the atmosphere to short horizontal wavelength gravity waves. *J. Geophys. Res.*, 113(D24104), 2008. doi: 10.1029/2007JD009682.

P. Preusse, S. D. Eckermann, M. Ern, J. Oberheide, R. H. Picard, R. G. Roble, M. Riese, J. M. Russell III, and M. G. Mlynczak. Global ray tracing simulations of the SABER gravity wave climatology. *J. Geophys. Res. Atmos.*, 114, 2009a. doi: 10.1029/2008JD011214.

P. Preusse, S. Schroeder, L. Hoffmann, M. Ern, F. Friedl-Vallon, J. Ungermann, H. Oelhaf, H. Fischer, and M. Riese. New perspectives on gravity wave remote sensing by spaceborne infrared limb imaging. *Atmos. Meas. Tech.*, 2(1):299–311, 2009b. doi: 10.5194/amt-2-299-2009.

P. Preusse, L. Hoffmann, C. Lehmann, M. J. Alexander, D. Broutman, H.-Y. Chun, A. Dudhia, A. Hertzog, M. Höpfner, Y.-H. Kim, W. Lahoz, J. Ma, M. Pulido, M. Riese, H. Sembhi, S. Wüst, V. Alishahi, M. Bittner, M. Ern, P. G. Fogli, S.-Y. Kim, V. Kopp, M. Lucini, E. Manzini, J. C. McConnell, J. Ruiz, G. Scheffler, K. Semeniuk, V. Sofieva, and F. Vial. Observation of gravity waves from space. *Final report, ESA study*, CN/22561/09/NL/AF:pp 195, 2012.

P. Preusse, M. Ern, P. Bechtold, S. D. Eckermann, S. Kalisch, Q. T. Trinh, and M. Riese. Characteristics of gravity waves resolved by ECMWF. *Atmos. Chem. Phys.*, 14(19): 10483–10508, 2014. doi: 10.5194/acp-14-10483-2014.

P. Queney. The problem of airflow over mountains: A summary of theoretical studies. *Bull. Amer. Meteor. Soc.*, 29:16–27, 1948.

M. Rapp, A. Dörnbrack, and B. Kaifler. An intercomparison of stratospheric gravity wave

potential energy densities from metop gps radio occultation measurements and ecmwf model data. *Atmospheric Measurement Techniques*, 11(2):1031–1048, 2018a. doi: 10.5194/amt-11-1031-2018. URL https://www.atmos-meas-tech.net/11/1031/2018/.

M. Rapp, A. Dörnbrack, and P. Preusse. Large midlatitude stratospheric temperature variability caused by inertial instability: A potential source of bias for gravity wave climatologies. *Geophys. Res. Lett.*, 45(19):10682–10690, OCT 16 2018b. doi: 10.5194/amt-11-1031-2018. URL https://www.atmos-meas-tech.net/11/1031/2018/.

M. Rauthe, M. Gerding, and F.-J. Lübken. Seasonal changes in gravity wave activity measured by lidars at mid-latitudes. *Atmos. Chem. Phys.*, 8(22):6775–6787, 2008. doi: 10.5194/acp-8-6775-2008. URL http://www.atmos-chem-phys.net/8/6775/2008/.

E. E. Remsberg, B. T. Marshall, M. Garcia-Comas, D. Krueger, G. S. Lingenfelser, J. Martin-Torres, M. G. Mlynczak, J. M. Russell III, A. K. Smith, Y. Zhao, C. Brown, L. L. Gordley, M. J. Lopez-Gonzalez, M. Lopez-Puertas, C. Y. She, M. J. Taylor, and R. E. Thompson. Assessment of the quality of the version 1.07 temperature-versus-pressure profiles of the middle atmosphere from TIMED/SABER. *J. Geophys. Res.*, 113, 2008. doi: 10.1029/2008JD010013.

A. Richmond and R. Roble. Dynamic effects of aurora-generated gravity-waves on the mid-latitude ionosphere. *J. Atm. Sol.-Terr. Phys.*, 41(7-8):841–852, 1979. ISSN 0021-9169. doi: 10.1016/0021-9169(79)90127-2.

M. Riese, H. Oelhaf, P. Preusse, J. Blank, M. Ern, F. Friedl-Vallon, H. Fischer, T. Guggenmoser, M. Höpfner, P. Hoor, M. Kaufmann, J. Orphal, F. Plöger, R. Spang, O. Suminska-Ebersoldt, J. Ungermann, B. Vogel, and W. Woiwode. Gimballed limb observer for radiance imaging of the atmosphere (gloria) scientific objectives. *Atmos. Meas. Tech.*, 7 (7):1915–1928, 2014. ISSN 1867-1381. doi: 10.5194/amt-7-1915-2014.

M. Ripepe, G. Barfucci, S. De Angelis, D. Delle Donne, G. Lacanna, and E. Marchetti. Modeling volcanic eruption parameters by near-source internal gravity waves. *Scientfic Reports*, 6, NOV 10 2016. ISSN 2045-2322. doi: 10.1038/srep36727.

M. Salby. Survey of planetary-scale traveling waves - the state of theory and observations. *Rev. Geophys.*, 22(2):209–236, 1984. ISSN 8755-1209. doi: 10.1029/RG022i002p00209.

M. L. Salby. Sampling theory for asynoptic satellite observatioons. part i: Space-time spectra, resolution, and aliasing. *J. Atmos. Sci.*, 39:2577–2600, 1982.

M. L. Salby and R. R. Garcia. Transient response to localized episodic heating in the tropics. Part I: Excitation and short-time near-field behavior. *J. Atmos. Sci.*, 44(2):458–498, 1987.

K. Sato, H. Hashiguchi, and S. Fukao. Gravity waves and turbulence associated with cumulus convection observed with the UHF/VHF clear-air Doppler radars. *J. Geophys. Res.*, 100(D4):7111–7119, 1995.

K. Sato, M. Yamamori, S. Y. Ogino, N. Takahashi, Y. Tomikawa, and T. Yamanouchi. A meridional scan of the stratospheric gravity wave field over the ocean in 2001 (MeSSO2001). *J. Geophys. Res.*, 108(4491), 2003. doi: 10.1029/2002JD003219.

K. Sato, S. Watanabe, Y. Kawatani, Y. Tomikawa, K. Miyazaki, and M. Takahashi. On the origins of mesospheric gravity waves. *Geophys. Res. Lett.*, 36, OCT 7 2009. ISSN 0094-8276. doi: 10.1029/2009GL039908.

L. Schoon and C. Zuelicke. A novel method for the extraction of local gravity wave parameters from gridded three-dimensional data: description, validation, and application. *Atmos. Chem. Phys.*, 18(9):6971–6983, MAY 17 2018. ISSN 1680-7316. doi: {10.5194/acp-18-6971-2018}.

S. Schroeder, P. Preusse, M. Ern, and M. Riese. Gravity waves resolved in ECMWF and measured by SABER. *Geophys. Res. Lett.*, 36, 2009. doi: 10.1029/2008GL037054.

U. Schumann. The horizontal spectrum of vertical velocities near the tropopause from global to gravity wave scales. *J. Atmos. Sci.*, 76(12):3847–3862, DEC 2019. ISSN 0022-4928. doi: 10.1175/JAS-D-19-0160.1.

T. G. Shepherd. Atmospheric circulation as a source of uncertainty in climate change projections. *Nature Geosci.*, 7(10):703–708, OCT 2014. ISSN 1752-0894. doi: 10.1038/NGEO2253.

W. C. Skamarock. Evaluating mesoscale NWP models using kinetic energy spectra. *Mon. Weath. Rev.*, 132:3019–3032, 2004.

A. K. Smith and M. Riese. Cryogenic infrared spectrometers and telescopes for the atmosphere (CRISTA) observations of tracer transport by inertially unstable circulations. *J. Geophys. Res.*, 104:19171–19182, 1999.

A. K. Smith, P. Preusse, and J. Oberheide. Middle atmosphere Kelvin waves observed in CRISTA 1 and 2 temperature and trace species. *J. Geophys. Res.*, 107(D23)), 2002. doi: 10.1029/2001JD000577.

C. C. Stephan, C. Strube, D. Klocke, M. Ern, L. Hoffmann, P. Preusse, and H. Schmidt. Gravity waves in global high-resolution simulations with explicit and parameterized convection. *J. Geophys. Res. Atmos.*, 124(8):4446–4459, APR 27 2019a. ISSN 2169-897X. doi: 10.1029/2018JD030073.

C. C. Stephan, C. Strube, D. Klocke, M. Ern, L. Hoffmann, P. Preusse, and H. Schmidt. Intercomparison of gravity waves in global convection-permitting models. *J. Atmos. Sci.*, 76(9):2739–2759, SEP 2019b. ISSN 0022-4928. doi: 10.1175/JAS-D-19-0040.1.

C. Strube, M. Ern, P. Preusse, and M. Riese. Removing spurious inertial instability signals from gravity wave temperature perturbations using spectral filtering methods. *Atmos. Meas. Tech.*, 13:accepted, 2020. doi: 10.5194/amt-2020-29. URL https://amt.copernicus.org/preprints/amt-2020-29/.

C. Strube, M. Ern, P. Preusse, and M. Riese. Propagation paths and source distributions of resolved gravity waves in ecmwf-ifs analysis fields around the southern polar night jet. *Atmos. Chem. Phys.*, page in preparation, 2021.

F. Trey. Ein beitrag zum studium der luftwogen. *Meteorol. Zeitschrift*, 36:25–28, 1919.

Q. T. Trinh, S. Kalisch, P. Preusse, M. Ern, H.-Y. Chun, S. D. Eckermann, M.-J. Kang, and M. Riese. Tuning of a convective gravity wave source scheme based on hirdls observations. *Atmos. Chem. Phys.*, 16:7335–7356, 2016. doi: $10.5194/\text{acp-16-7335-2016}$.

T. Tsuda, M. Nishida, C. Rocken, and R. H. Ware. A global morphology of gravity wave activity in the stratosphere revealed by the GPS occultation data (GPS/MET). *J. Geophys. Res.*, 105(D6):7257–7274, 2000.

L. W. Uccellini and S. E. Koch. The synoptic setting and possible energy sources for mesoscale wave disturbances. *Mon. Weath. Rev.*, 115(3):721–729, 1987.

J. Vanneste and I. Yavneh. Exponentially Small Inertia–Gravity Waves and the Breakdown of Quasigeostrophic Balance. *Journal of the Atmospheric Sciences*, 61(2):211–223, 01 2004. ISSN 0022-4928. doi: $10.1175/1520\text{-}0469(2004)061{<}0211{:}\text{ESIWAT}{>}2.0.\text{CO};2$. URL `https://doi.org/10.1175/1520-0469(2004)061<0211:ESIWAT>2.0.CO;2`.

L. Wang and M. J. Alexander. Global estimates of gravity wave parameters from GPS radio occultation temperature data. *J. Geophys. Res. Atmos.*, 115, 2010. ISSN 0148-0227. doi: $10.1029/\text{2010JD013860}$.

A. Wegener. Studien über luftwogen. *Beitr. Physik Freien Atmos.*, 4:23–25, 1906.

R. M. Worthington. Alignment of mountain wave patterns above wales: A vhf radar study during 1990-1998. *J. Geophys. Res.*, 104:9199–9212, 1999.

C. J. Wright and N. P. Hindley. How well do stratospheric reanalyses reproduce high-resolution satellite temperature measurements? *Atmos. Chem. Phys.*, 18(18):13703–13731, 2018. doi: $10.5194/\text{acp-18-13703-2018}$. URL `https://www.atmos-chem-phys.net/18/13703/2018/`.

C. J. Wright, N. P. Hindley, L. Hoffmann, M. J. Alexander, and N. J. Mitchell. Exploring gravity wave characteristics in 3-d using a novel s-transform technique: Airs/aqua measurements over the southern andes and drake passage. *Atmos. Chem. Phys.*, 17(13):8553–8575, 2017. doi: $10.5194/\text{acp-17-8553-2017}$.

D. L. Wu and S. D. Eckermann. Global gravity wave variances from Aura MLS: Characteristics and interpretation. *J. Atmos. Sci.*, 65(12):3695–3718, DEC 2008. ISSN 0022-4928. doi: $10.1175/2008\mathrm{JAS}2489.1$.

D. L. Wu and J. W. Waters. Gravity-wave-scale temperature fluctuations seen by the UARS MLS. *Geophys. Res. Lett.*, 23(23):3289–3292, 1996a.

D. L. Wu and J. W. Waters. Satellite observations of atmospheric variances: A possible indication of gravity waves. *Geophys. Res. Lett.*, 23:3631–3634, 1996b.

X. Zhu. Radiative damping revisited - Parametrization of damping rate in the middle atmosphere. *J. Atmos. Sci.*, 50(17):3008–3021, SEP 1 1993. ISSN 0022-4928. doi: $10.1175/1520\text{-}0469(1993)050{<}3008{:}\mathrm{RDRPOD}{>}2.0.\mathrm{CO};2$.

F. Zink and R. A. Vincent. Wavelet analysis of stratospheric gravity wave packets over macquarie island, 1. wave parameters. *J. Geophys. Res.*, 106:275–288, 2001a.

F. Zink and R. A. Vincent. Wavelet analysis of stratospheric gravity wave packets over macquarie island, 2. intermittency and mean-flow accelerations. *J. Geophys. Res.*, 106:289–297, 2001b.

Danksagung

Zunächst möchte ich meinem Doktorvater Prof. Martin Riese danken, dass er mir das Thema zur vorgelegten Doktorarbeit anvertraut hat. Die Diskussionen über meine Forschungsergebnisse und anstehende Veröffentlichungen haben mich immer voran gebracht.

Genauso danke ich meinem Betreuer Peter Preuße, der mich mit seinem wissenschaftlichen KnowHow und beinahe endlosen Unterhaltungen über Schwerewellen immer auf Trab gehalten hat. Vielen, herzlichen Dank, dass ich bei dir mit interessanten Ergebnissen und auch mit Problemen immer auf ein offenes Ohr gestoßen bin.

Vielen Dank an das HITEC-Doktorandenprogramm. Mein Stipendium hat meine Doktorarbeit erst möglich gemacht. Außerdem haben mir die zusätzlichen Unterstützungen, für z.B. den Besuch meines externen Mentors Corwin Wright, mir einzigartige, wissenschaftliche Erfahrungen gewährt.

Ich danke der Deutschen Forschungsgemeinschaft und den Kollegen aus der MS-GWaves-Forschergruppe. Neben der unentbehrlichen Finanzierung aus dem Projekt, hat der wissenschaftliche Diskurs mit euch meine Ergebnisse stets verfeinert.

Darüber hinaus danke ich allen früheren und aktuellen Kollegen des IEK-7 für viereinhalb glorreiche Jahre. Danke für die Kaffeepausen, die Skiausflüge und die allgemeine Gemeinschaft zwischen Kollegen. Es war ein wahres Vergnügen mit euch zusammenzuarbeiten. Insbesondere Isabell Krisch und Jörn Ungermann haben mich tatkräftig durch die ein oder anderen verzweifelte Lage begleitet. Danke dafür!

Zu guter Letzt, ein dickes Dankeschön an meine Familie und Flo. Ihr wart immer für mich da und ohne euch wäre diese Arbeit nicht zustande gekommen.